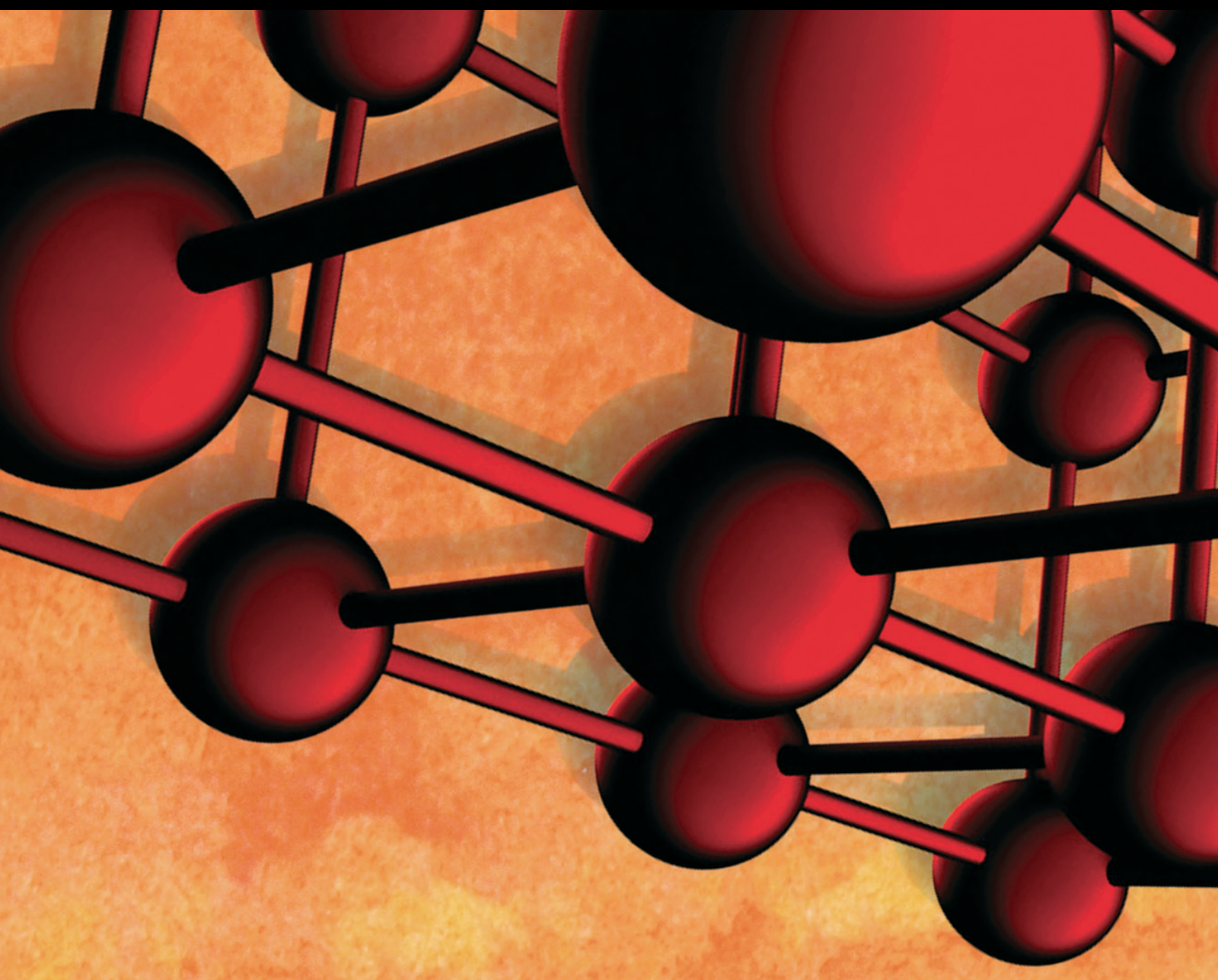


Materials for Nuclear and Fossil Energy Applications

Guest Editors: Kisor Kumar Sahu, Ajit Kumar Roy, Amritendu Roy, Kaushik Das, and Randhir Singh





Materials for Nuclear and Fossil Energy Applications

Advances in Materials Science and Engineering

Materials for Nuclear and Fossil Energy Applications

Guest Editors: Kisor Kumar Sahu, Ajit Kumar Roy,
Amritendu Roy, Kaushik Das, and Randhir Singh



Copyright © 2016 Hindawi Publishing Corporation. All rights reserved.

This is a special issue published in “Advances in Materials Science and Engineering.” All articles are open access articles distributed under the Creative Commons Attribution License, which permits unrestricted use, distribution, and reproduction in any medium, provided the original work is properly cited.

Editorial Board

Dimitrios G. Aggelis, Belgium
Michael Aizenshtein, Israel
Jarir Aktaa, Germany
K. G. Anthymidis, Greece
Amit Bandyopadhyay, USA
Arun Bansil, USA
Massimiliano Barletta, Italy
Mikhael Bechelany, France
Jozef Bednarcik, Germany
Avi Bendavid, Australia
Jamal Berakdar, Germany
Giovanni Berselli, Italy
Patrice Berthod, France
Didier Blanchard, Denmark
Susmita Bose, USA
Heinz-Günter Brokmeier, Germany
Steve Bull, UK
Peter Chang, Canada
Daolun Chen, Canada
Gianluca Cicala, Italy
Gabriel Cuello, France
Narendra B. Dahotre, USA
João P. Davim, Portugal
Angela De Bonis, Italy
Jeff Th. M. De Hosson, Netherlands
Francesco Delogu, Italy
Seshu B. Desu, USA
Guru P. Dinda, USA
Yong Ding, USA
Nadka Tz. Dintcheva, Italy
Kaveh Edalati, Japan
Philip Eisenlohr, USA
Gilbert Fantozzi, France
Paolo Ferro, Italy
Massimo Fresta, Italy
Eric Freysz, France
Sergi Gallego, Spain
Santiago Garcia-Granda, Spain
Filippo Giannazzo, Italy

Daniel Guay, Canada
Fawzy H. Samuel, Canada
Hiroki Habazaki, Japan
Joke Hadermann, Belgium
Satoshi Horikoshi, Japan
David Houivet, France
Rui Huang, USA
Michele Iafisco, Italy
Katsuyuki Kida, Japan
Jae-Ho Kim, Republic of Korea
Akihiko Kimura, Japan
Takayuki Kitamura, Japan
Hongchao Kou, China
Prashant Kumta, USA
Luciano Lamberti, Italy
Heinrich Lang, Germany
Pavel Lejcek, Czech Republic
Cristina Leonelli, Italy
Ying Li, USA
Jun Liu, China
Meilin Liu, Georgia
Wei Liu, France
Yunqi Liu, China
Fernando Lusquiños, Spain
Peter Majewski, Australia
Philippe Miele, France
Hossein Moayedi, Iran
Roberto Morandotti, Canada
Paul Munroe, Australia
Rufino M. Navarro, Spain
Luigi Nicolais, Italy
Hiroschi Noguchi, Japan
Chérif Nouar, France
José L. Ocaña, Spain
Tsutomu Ohzuku, Japan
Olanrewaju Ojo, Canada
Gianfranco Palumbo, Italy
Xiaoqing Pan, USA
Anna Paradowska, Australia

Matthew Peel, UK
Gianluca Percoco, Italy
Giorgio Pia, Italy
Jean-Francois Pierson, France
Simon C. Potter, Canada
Manijeh Razeghi, USA
Anna Richelli, Italy
Antonio Riveiro, Spain
Pascal Roussel, France
Timo Sajavaara, Finland
Antti Salminen, Finland
Carlo Santulli, Italy
Franz-Josef Schmitt, Germany
Jainagesh A. Sekhar, USA
Fridon Shubitidze, USA
Maria A. Signore, Italy
Donato Sorgente, Italy
Charles C. Sorrell, Australia
Costas M. Soukoulis, USA
Sam-Shajing Sun, USA
Kohji Tashiro, Japan
Somchai Thongtem, Thailand
Achim Trampert, Germany
Filip Tuomisto, Finland
Krystyn Van Vliet, USA
Qiang Wang, China
Rong Wang, USA
Rui Wang, China
Lu Wei, China
Jörg M. K. Wieszorek, USA
Wei Wu, USA
Hemmige S. Yathirajan, India
Wenbin Yi, China
Belal F. Yousif, Australia
Jinghuai Zhang, China
Li Zhang, China
Ming-Xing Zhang, Australia
Wei Zhou, China

Contents

Materials for Nuclear and Fossil Energy Applications

Kisor Kumar Sahu, Ajit Kumar Roy, Amritendu Roy, Kaushik Das, and Randhir Singh
Volume 2016, Article ID 5247563, 1 page

Molecular Dynamics Simulation to Investigate the Interaction of Asphaltene and Oxide in Aggregate

Rui Li, Hui Du, Zepeng Fan, and Jianzhong Pei
Volume 2016, Article ID 3817123, 10 pages

Effect of Suction Cycles and Suction Gradients on the Water Retention Properties of a Hard Clay

Liufeng Chen and Hua Peng
Volume 2015, Article ID 313682, 6 pages

Corrosion Inhibiting Mechanism of Nitrite Ion on the Passivation of Carbon Steel and Ductile Cast Iron for Nuclear Power Plants

K. T. Kim, H. W. Kim, H. Y. Chang, B. T. Lim, H. B. Park, and Y. S. Kim
Volume 2015, Article ID 408138, 16 pages

Gas-Cooled Thorium Reactor with Fuel Block of the Unified Design

Igor Shamanin, Sergey Bedenko, Yuriy Chertkov, and Ildar Gubaydulin
Volume 2015, Article ID 392721, 8 pages

Fabrication of UO₂ Porous Pellets on a Scale of 30 kg-U/Batch at the PRIDE Facility

Sang-Chae Jeon, Jae-Won Lee, Ju-Ho Lee, Sang-Jun Kang, Kwang-Yun Lee, Yung-Zun Cho, Do-Hee Ahn, and Kee-Chan Song
Volume 2015, Article ID 376173, 8 pages

Cyclic Stress Response and Fracture Behaviors of Alloy 617 Base Metal and Weld Joints under LCF Loading

Seon Jin Kim, Rando Tungga Dewa, Woo Gon Kim, and Min Hwan Kim
Volume 2015, Article ID 207497, 11 pages

Corrosion Control of Alloy 690 by Shot Peening and Electropolishing under Simulated Primary Water Condition of PWRs

Kyung Mo Kim, Hee-Sang Shim, Myung Ji Seo, and Do Haeng Hur
Volume 2015, Article ID 357624, 9 pages

Preparation of U-Zr-Mn, a Surrogate Alloy for Recycling Fast Reactor Fuel

Jong-Hwan Kim, Ki-Hwan Kim, and Chan-Bock Lee
Volume 2015, Article ID 131704, 8 pages

Editorial

Materials for Nuclear and Fossil Energy Applications

**Kisor Kumar Sahu,^{1,2} Ajit Kumar Roy,¹ Amritendu Roy,¹
Kaushik Das,¹ and Randhir Singh¹**

¹*School of Minerals, Metallurgical and Materials Engineering, Indian Institute of Technology Bhubaneswar, Bhubaneswar 751007, India*

²*Center of Excellence for Novel Energy Materials (CENEMA), Indian Institute of Technology Bhubaneswar, Bhubaneswar 751007, India*

Correspondence should be addressed to Kisor Kumar Sahu; kisorsahu@iitbbs.ac.in

Received 18 January 2016; Accepted 19 January 2016

Copyright © 2016 Kisor Kumar Sahu et al. This is an open access article distributed under the Creative Commons Attribution License, which permits unrestricted use, distribution, and reproduction in any medium, provided the original work is properly cited.

We are extremely happy to release this special issue. Energy is the prime driver for modern civilization. Strong inverse correlation between per capita energy consumption and poverty level suggests that, in order to alleviate poverty and enhancement of general living standards, the global energy consumption will grow manifold in the coming decades. With present-day technologies, this is simply not feasible particularly for the choice of present-day resource portfolio and the associated economic cost of scaling. For example, according to one estimate, for the global population to achieve western European living standard, characterized by moderate rate of per capita energy consumption (≈ 7 kW compared to ≈ 11 kW for USA), we will need \$2.2 trillion per year investment for next 20 years in a sustained rate at present-day prices. While one can debate about these numbers, what is clear is that, without technological advancements and breakthroughs, majority of the global population will have no choice but to settle for very poor living standards. Global climate change and deteriorating air quality in urban areas are also a direct consequence of how we source and utilize energy. Since the growth rate of cleaner energy sources is far lower than needed, serious technical research is necessary for better utilization of the traditional resources. Generally, materials are the bottleneck in developing new methods and technologies and hence, in this issue, we have tried to encompass a broad range of topics related to the materials aspects of nuclear energy-based and fossil fuel-based energy generation.

Articles presented in this issue are related to Sodium-cooled Fast Reactors (SFRs), Very High Temperature gas-cooled Reactors (VHTRs), Pressurized Water Reactors

(PWRs), and other reactors. Alloy development for nuclear fuel rods is an important topic in nuclear technology, and in this issue the article by J.-H. Kim and coworkers discusses the development of an injection casting process for preparing fuel slugs of U-10Zr-5Mn, a surrogate alloy for use in Sodium-cooled Fast Reactors (SFRs). Alloys to be used in energy generation plants have stringent requirements in terms of high temperature mechanical properties. In this issue, S. J. Kim and coworkers have presented a comparison of cyclic stress response and fracture behavior of Alloy 617 in the form of base metal and in the form of welded joints. Another critical issue in nuclear power generation is corrosion inhibition of the inner linings of the pipes and the tubes. These alloys get corroded due to exposure to primary water of nuclear power plants. Surface treatment of the alloys and/or inhibitor addition to the primary water are two approaches to inhibit corrosion, and these approaches are discussed in the articles by K. M. Kim et al. and by S. J. Kim et al., respectively.

Materials challenges in nuclear waste management and in recovery of nuclear fuel from spent fuel rods have also been considered in this issue. In addition, design of new generation of low power thorium-based nuclear technology also forms a part of this issue.

*Kisor Kumar Sahu
Ajit Kumar Roy
Amritendu Roy
Kaushik Das
Randhir Singh*

Research Article

Molecular Dynamics Simulation to Investigate the Interaction of Asphaltene and Oxide in Aggregate

Rui Li,¹ Hui Du,² Zepeng Fan,¹ and Jianzhong Pei¹

¹*School of Highway, Chang'an University, Xi'an 710064, China*

²*School of Transportation Engineering, Southeast University, Nanjing 210096, China*

Correspondence should be addressed to Jianzhong Pei; peijianzhong@126.com

Received 4 July 2015; Accepted 4 January 2016

Academic Editor: Amritendu Roy

Copyright © 2016 Rui Li et al. This is an open access article distributed under the Creative Commons Attribution License, which permits unrestricted use, distribution, and reproduction in any medium, provided the original work is properly cited.

The asphalt-aggregate interface interaction (AAI) plays a significant role in the overall performances of asphalt mixture, which is caused due to the complicated physicochemical processes and is influenced by various factors, including the acid-base property of aggregates. In order to analyze the effects of the chemical constitution of aggregate on the AAI, the average structure $C_{65}H_{74}N_2S_2$ is selected to represent the asphaltene in asphalt and magnesium oxide (MgO), calcium oxide (CaO), aluminium sesquioxide (Al_2O_3), and silicon dioxide (SiO_2) are selected to represent the major oxides in aggregate. The molecular models are established for asphaltene and the four oxides, respectively, and the molecular dynamics (MD) simulation was conducted for the four kinds of asphaltene-oxide system at different temperatures. The interfacial energy in MD simulation is calculated to evaluate the AAI, and higher value means better interaction. The results show that interfacial energy between asphaltene and oxide reaches the maximum value at 25°C and 80°C and the minimum value at 40°C. In addition, the interfacial energy between asphaltene and MgO was found to be the greatest, followed by CaO, Al_2O_3 , and SiO_2 , which demonstrates that the AAI between asphalt and alkaline aggregates is better than acidic aggregates.

1. Introduction

Studies have shown that asphalt pavement damage phenomenon has a strong dependency upon asphalt-aggregate interfacial nature. If the bond between asphalt and aggregate is weak, then the interface between asphalt and aggregate is prone to failure, which results in the early damage of pavement. Therefore, many methods were used to study the interface between asphalt and aggregate in different perspectives. Elphinstone [1] proposed that the surface free energy is an effective approach to predict the fatigue and moisture properties of mixture, and adhesion process of aggregate plays an important role. Tan et al. [2] tested the phase angle and complex shear modulus of matrix asphalt and asphalt mastic by dynamic shear rheometer, and the asphalt-aggregate interaction capabilities were evaluated by K.Ziegel-B parameter. Cheng et al. [3] measured the surface free energy of different asphalt and aggregates and calculated the adhesion work of asphalt and reactive aggregates with and without water.

Bhasin et al. [4] proposed quantifying the free energy of the surface of asphalt-aggregate adhesion energy, and the results have shown that the same type of aggregate and bitumen adhesion between the energies has significant difference. To sum up, on the asphalt-aggregate interface studies have been largely analyzed from the experimental point of view. However, the experimental results were affected by many factors, in the dynamic shear rheological experiments; powder-binder ratio had greater impact on the test results, and how to determine the best powder-binder ratio is a problem. While aggregate composition is complex, powder, and mixed into the asphalt, mastic asphalt does not characterize asphalt-aggregate interface behavior. In the surface energy calculation, measurement results on the final great influence, different methods may result in different surface energy, resulting in a larger difference in the results.

In recent years, with the improvement of computer hardware and the perfection of related theory, molecular dynamics (MD) have become the effective means to study a complex

system from the molecular level [5], the effective methods for the deep understanding of asphaltene adsorption characteristics, and the interaction mechanism of the interface from the microscopic view. At present, the domestic and foreign scholars mostly from the angle of test studied asphalt with aggregate interface area properties, and the computer simulation research is less. As a result, the MD method asphalt-aggregate interface behavior of asphalt mixture's research has the vital significance.

Based on the molecular dynamics calculation, we can simulate the asphalt-aggregate interfacial behavior. In four components of asphalt, asphaltene molecular mass is bigger and has stronger polarity and the asphaltenes content has a great impact on the properties of asphalt [6]. Asphaltene is fused aromatic ring system as the core, with a number of different alkyl chains linked structure, with N, S, and O heteroatoms, not soluble in nonpolar molecules of the corresponding normal alkanes soluble in benzene and toluene matter [7]. The composition, structure, and morphology of the asphaltene are very complex. In the study, the average molecular model is often used to replace the chemical structure [8]. Rogel [9] proposed a representative average asphaltene molecular structure model for the study of this paper. According to the composition of aggregate analysis, aggregates content of more oxides was analyzed, the remaining content of less neglected ones. The asphalt-oxide interface model based on dynamics simulation of the interfacial energy and adsorption configuration, which can quantitatively point out the ability of the main oxides in asphalt and aggregate interface interaction, for further understanding the mechanism of adhesion between asphalt and aggregate, is of great significance.

2. Computer Simulation Theory

2.1. Basic Theory. Calculations were conducted with Accelrys Materials Studio software package in this study and this method relies mainly on Newtonian mechanics to simulate the movement of molecular systems, the samples are taken in different states of the molecular system, and the configuration of the system is integrated. The thermodynamic quantities and other macroscopic properties are further calculated based on the results of the integration configuration.

COMPASS is selected for force field simulation, and the potential energy function form is shown as follows:

$$E_{\text{total}} = \sum_{\text{bond}} E_b(b) + \sum_{\text{angle}} E_\theta(\theta) + \sum_{\text{dihedral}} E_\phi(\phi) + \sum_{\text{out-of-plane}} E_\chi(\chi) + \sum_{\text{cross}} E(b, \theta, \phi) + E_{\text{coulomb}} + E_{\text{vdw}} \quad (1)$$

In (1), the preceding five letters are bonding interaction of which the potential energy function contains bond lengths, bond angles, dihedral angles, plane, and cross-term; b , θ , ϕ , and χ are expressed as bond lengths, bond angles, dihedral angles, and off-plane vibration; the next two letters are non-bonding interactions which are electrostatic interaction

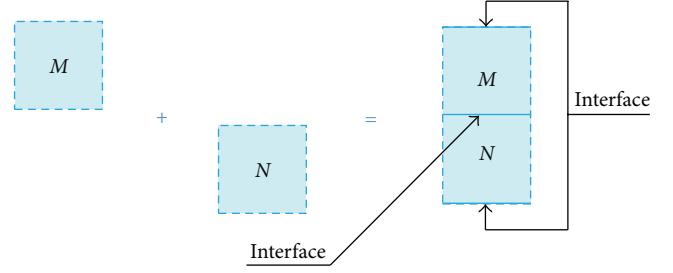


FIGURE 1: Schematic diagram of the interfacial energy.

E_{coulomb} and van der Waals interaction E_{vdw} , respectively. E_{coulomb} and E_{vdw} are calculated by the following:

$$E_{\text{coulomb}} = \sum_{i>j} \frac{q_i q_j}{r_{ij}}, \quad (2)$$

$$E_{\text{vdw}} = \sum \varepsilon_{ij} \left[2 \left(\frac{r_{ij}^0}{r_{ij}} \right)^9 - 3 \left(\frac{r_{ij}^0}{r_{ij}} \right)^6 \right]. \quad (3)$$

In (2) and (3), i and j represent different atoms; q is atomic charge; r is the distance of different atomic; ε is potential well depth.

The interface model is composed of three layers. The first layer is oxide, the second layer is asphaltene, and the third layer is vacuum, eliminating the impact of the cyclical interaction between the particles resulting from double counting.

The molecular dynamics simulation of the canonical ensemble (NVT) is completed by Discover module. According to the set temperature, the temperature is controlled by Andersen thermostat, the initial rate of each molecule is randomly generated by the Maxwell-Boltzmann distribution, Newton's equation of motion is calculated by Velocity Verlet algorithm, and the van der Waals interaction and Coulomb interaction are calculated by Charge Group method.

2.2. Interfacial Energy Calculation. Interfacial energy is also known as the interaction energy, the calculation method is similar to the surface energy, and the difference is that the interfacial energy reflects the bonding strength between the two materials. The interface may be between the same materials or different materials; the interfacial energy of the same material can be theoretically equal to the surface energy. The interfacial energy can be calculated as shown in Figure 1.

In Figure 1, to calculate the interfacial energy between materials M and N , the interface model is constructed as shown in the right of Figure 1. The model is calculated in temperature T and system NVT by molecular dynamics until the system reaches a steady state; the energy of the model is E_{total} . The interface models M and N are constructed as shown in the left of Figure 1 and calculated by molecular dynamics; the energy of the two models is E_M and E_N , respectively. If the area of the combination surface is A , the interfacial energy is calculated as follows:

$$\gamma_{\text{int}} = \frac{(E_M + E_N - E_{\text{total}})}{2A}. \quad (4)$$

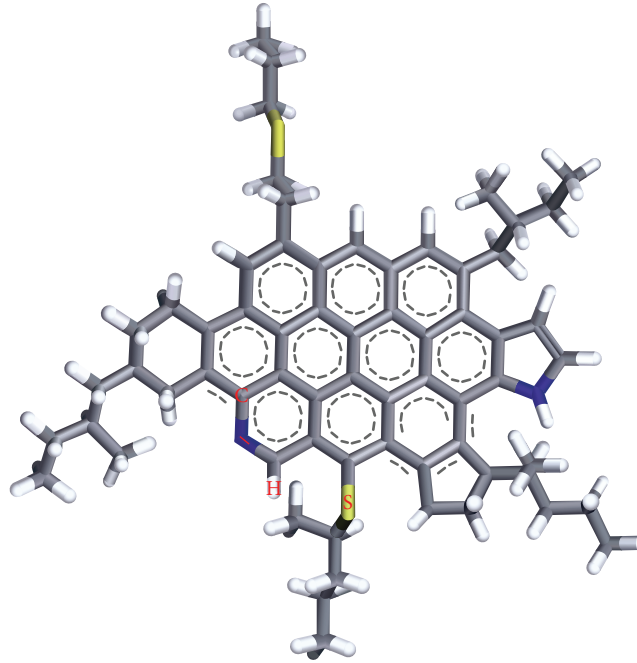


FIGURE 2: Average molecular structure of asphaltene.

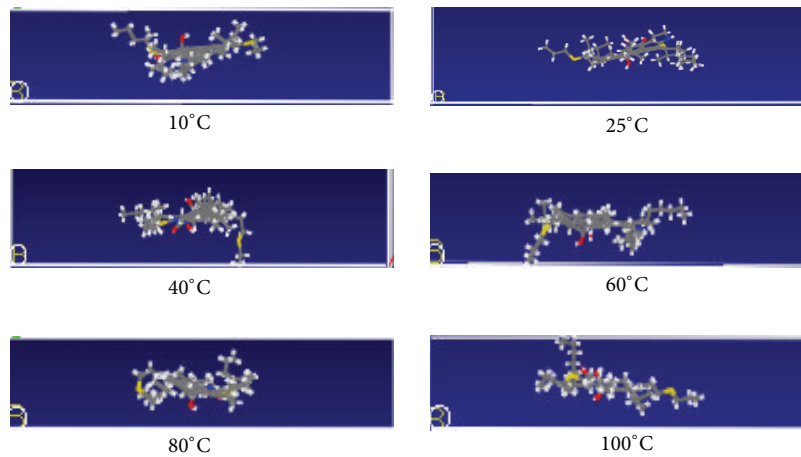


FIGURE 3: The configuration of asphaltene molecules in different temperature.

3. Results and Discussion

3.1. Asphaltene Molecular Structure Model. Since the composition and structure of the asphaltene are very complex, Rogel et al. built average molecular structure, which was standardized samples studied in the Strategic Highway Research Program (SHRP). The average structure is shown in Figure 2.

Because asphaltenes are highly polydisperse molecules, the construction is highly complex. So in the research, we used one of the average molecules. For the simulation, we chose the COMPASS force field. For the asphaltene, the target density was set to 1 g/cm^3 , constructing the configuration of asphaltene system. In order to analyze the temperature dependence of the asphaltene system, six different temperatures were

chosen: 10°C (283.15 K), 25°C (298.15 K), 40°C (313.15 K), 60°C (333.15 K), 80°C (353.15 K), and 100°C (373.15 K), and the results are shown in Figure 3.

3.2. Oxide Molecular Structure Model

3.2.1. Selection of Representative Oxides. To simulate aggregate, we used 10 chemical compositions of aggregate ($M1$, $M2, \dots, M10$) suggested by Ozkahraman and Işık [10] (as seen in Figure 4). The chemical composition of aggregate is $\text{SiO}_2 > \text{CaO} > \text{Al}_2\text{O}_3 > \text{MgO} > \text{Fe}_2\text{O}_3 > \text{NaO} > \text{K}_2\text{O}$.

Therefore, the simulation is mainly focused on the four oxides which are SiO_2 , CaO , Al_2O_3 , and MgO .

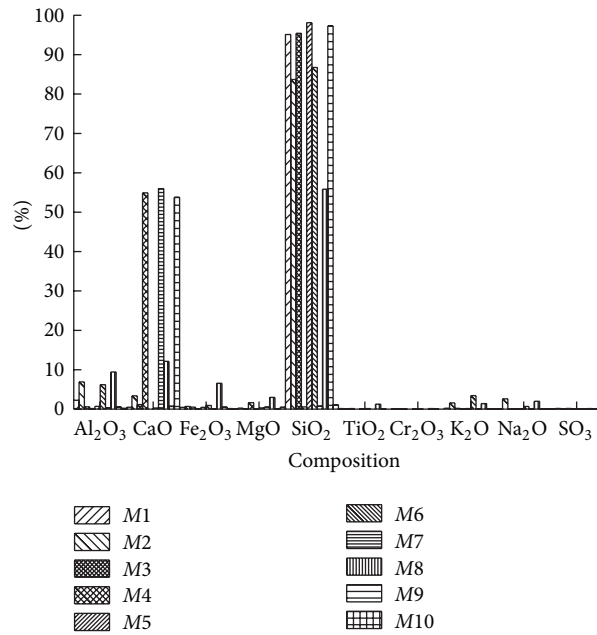


FIGURE 4: The chemical composition of aggregates.

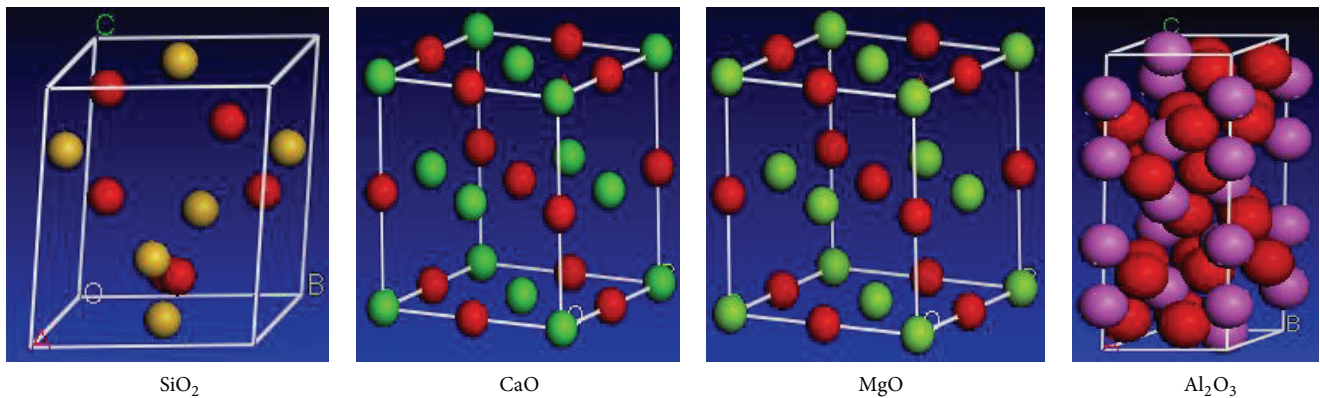


FIGURE 5: Four kinds of oxide molecular cell structure.

3.2.2. Building Oxide Molecular Cell. By the molecular dynamics software that comes with the unit cell model of oxide molecules, molecular cell structure of oxide is formed after importing the unit cell model, as shown in Figure 5.

3.2.3. Building Oxide Supercell. Based on the molecular cell above, the cell is intercepted by section 0 0 1. Secondly, the force field is assigned to each atom of cell. In the paper, the force field is COMPASS. The energy of cell is minimized by the Minimize module of Discover. Finally, the oxide supercell structure is built by the supercell module of Build which is composed of 5×5 matrix. For example, the process of building supercell structure of SiO_2 is shown in Figure 6.

3.3. The Interaction of Asphaltene and Oxide

3.3.1. Creating of Asphaltene/Oxide Interface. Interface model is composed of three layers. Layer 1 is oxide, layer 2 is asphaltene, and the last layer is 30 Å thick vacuum layer. According

to the depiction earlier, the three-layer interface structure was formed. For example, the asphaltene/ SiO_2 interface model of 25°C is shown in Figure 7.

3.3.2. Dynamic Simulation Interface of Asphaltene/Oxide. As shown in the interface model in Figure 7, molecular dynamic simulation was then conducted in order to equilibrate systems further. The temperature is set and maintained constant by Andersen thermostat; the initial rate of molecular cell structure is randomly generated by the Maxwell-Boltzmann distribution. The Velocity Verlet algorithm is used to solve Newton's equation of motion. The van der Waals interaction and the Coulomb interaction are calculated by Charge Group method. The intermolecular interaction is corrected by an average density approximation. The system was simulated under NVT conditions with velocity rescaling, which was used for 2000 ps with a time step of 1.0 fs to dissipate high energy interactions between molecules.

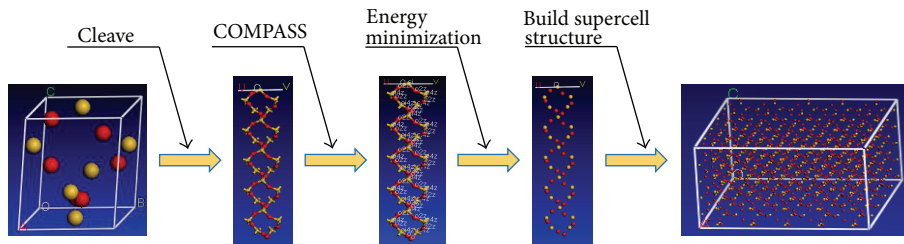
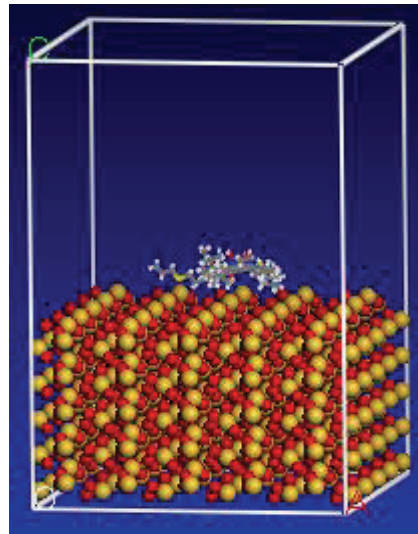
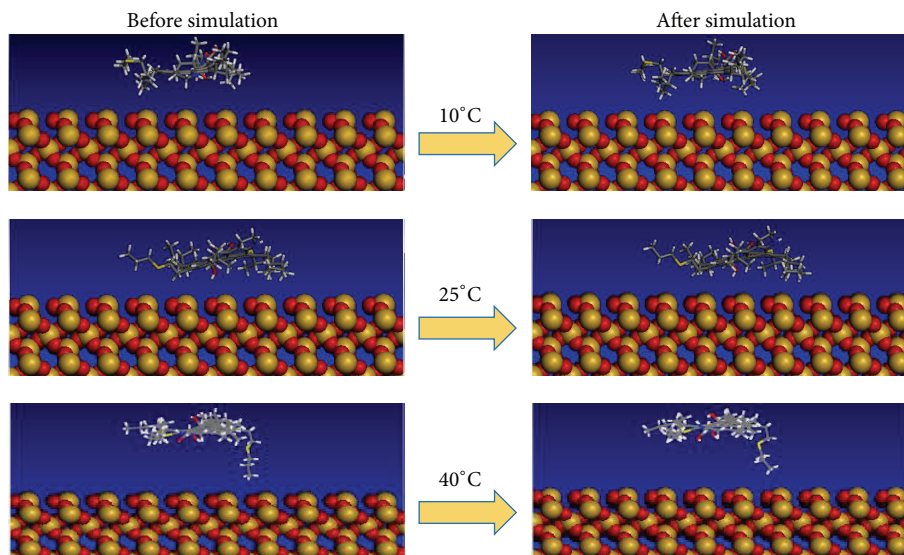


FIGURE 6: The process of building supercell structure.

FIGURE 7: Asphaltene/SiO₂ interface model.FIGURE 8: The interface configuration of asphaltene/SiO₂ (10–40°C).

MD simulation of four-group interface model was performed for temperatures of 10°C (283.15 K), 25°C (298.15 K), 40°C (313.15 K), 60°C (333.15 K), 80°C (353.15 K), and 100°C (373.15 K). The results are shown in Figures 8–15.

As shown in the four interface configurations, the asphaltene molecular structures change in varying degree after the simulation. The asphaltene molecular structure moves closer to the oxide surface. Comparing the four kinds of interface

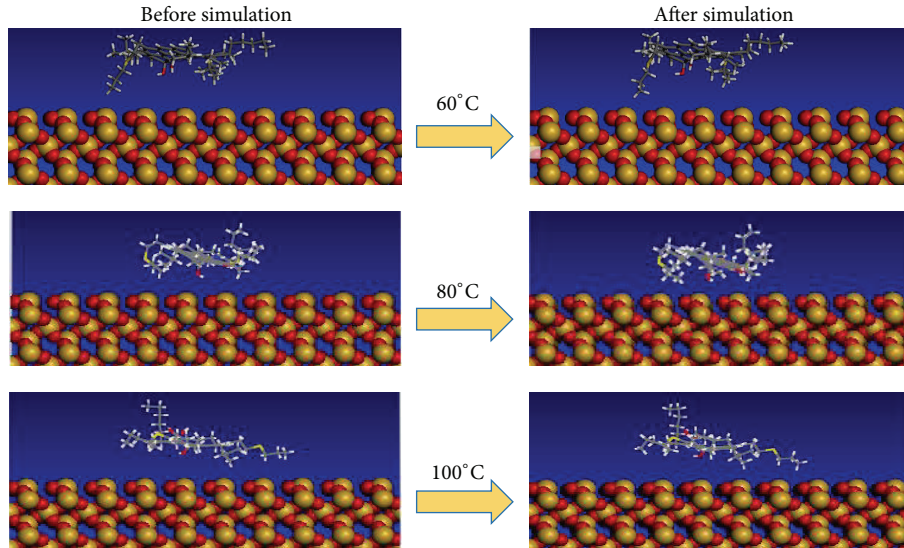


FIGURE 9: The interface configuration of asphaltene/SiO₂ (60–100°C).

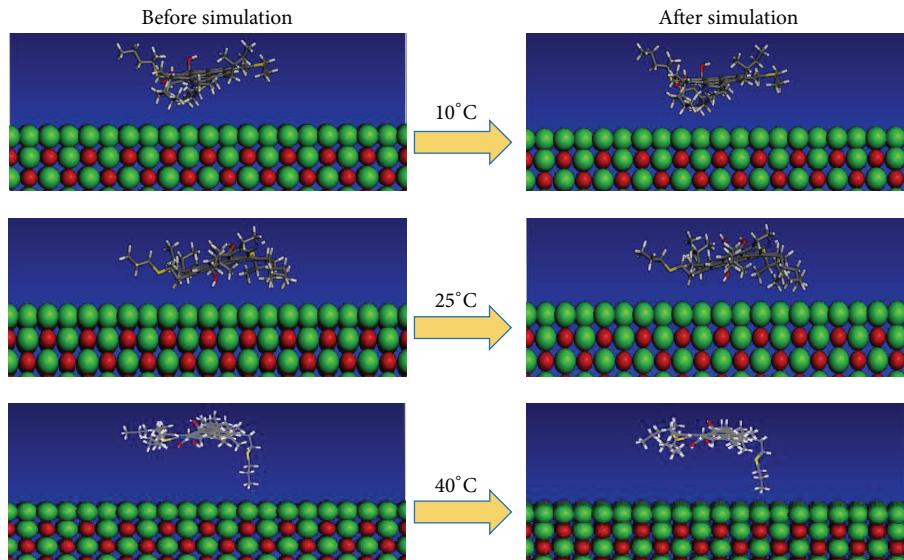


FIGURE 10: The interface configuration of asphaltene/CaO (10–40°C).

configuration, it is difficult to evaluate the interaction between asphaltene and oxides accurately. For the fixed interface configuration, it is almost impossible to distinguish whether the interaction changes with temperature. Therefore, the interfacial energy is introduced to evaluate the interaction more precisely.

3.3.3. *The Calculation of Interfacial Energy.* The interfacial energy can be calculated according to the following:

$$\gamma_{\text{int}} = \frac{(E_{\text{polymer}} + E_{\text{surface}} - E_{\text{total}})}{2A}. \quad (5)$$

The four-interface model size is $49.000 \times 49.000 \times 26.38067 \text{ \AA}$. So the interfacial energy equation can be simplified as follows:

$$\gamma'_{\text{int}} = (E_{\text{polymer}} + E_{\text{surface}} - E_{\text{total}}). \quad (6)$$

After the molecular dynamics simulation, the four kinds of interfacial energy are shown in Tables 1 and 2.

The interfacial energy of asphaltene/SiO₂ varies from $2.22E + 01$ to $2.09E + 02$ kJ/mol within the temperature range of 10°C to 100°C; the calculated variation ranges of asphaltene/CaO, asphaltene/MgO, and asphaltene/Al₂O₃ within the same temperature range are $7.44E + 02$ to $1.00E + 03$ kJ/mol,

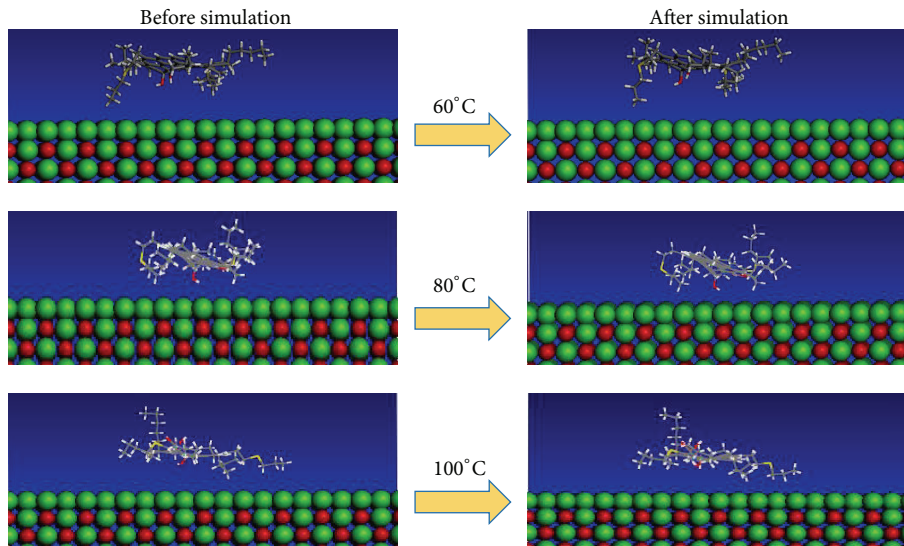


FIGURE 11: The interface configuration of asphaltene/CaO (60–100°C).

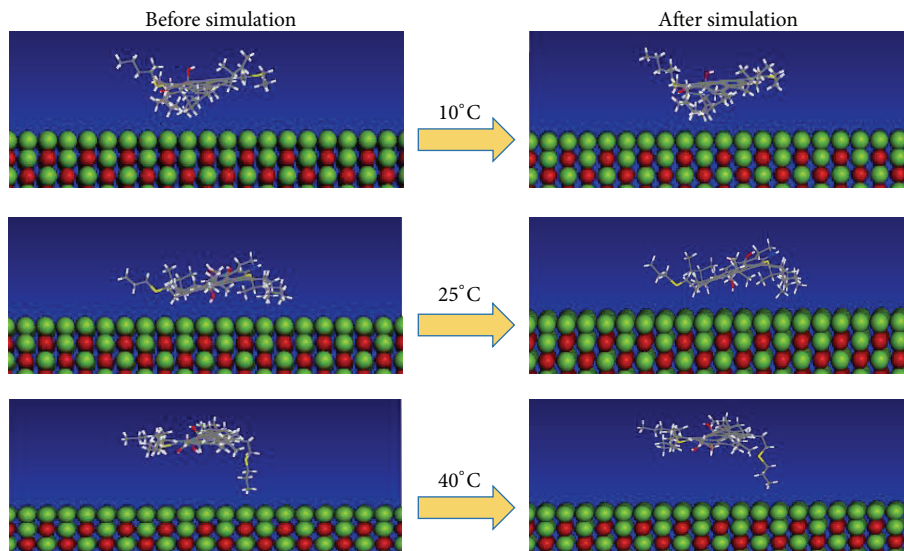


FIGURE 12: The interface configuration of asphaltene/MgO (10–40°C).

TABLE 1: Asphaltene/SiO₂ and asphaltene/CaO.

	Temp. (°C)	E_{total} (kJ/mol)	E_{polymer} (kJ/mol)	E_{surface} (kJ/mol)	$E_{\text{interface}}$ (kJ/mol)
Asphaltene/SiO ₂	10	$9.03E + 06$	$3.63E + 02$	$9.03E + 06$	$2.22E + 01$
	25	$9.03E + 06$	$3.83E + 02$	$9.03E + 06$	$2.09E + 02$
	40	$9.03E + 06$	$3.73E + 02$	$9.03E + 06$	$3.25E + 01$
	60	$9.03E + 06$	$3.72E + 02$	$9.03E + 06$	$3.88E + 01$
	80	$9.03E + 06$	$3.83E + 02$	$9.03E + 06$	$1.36E + 02$
	100	$9.03E + 06$	$3.85E + 02$	$9.03E + 06$	$1.31E + 02$
Asphaltene/CaO	10	$-1.57E + 06$	$3.71E + 03$	$-1.57E + 06$	$8.99E + 02$
	25	$-1.57E + 06$	$3.69E + 03$	$-1.57E + 06$	$9.63E + 02$
	40	$-1.57E + 06$	$3.68E + 03$	$-1.57E + 06$	$7.44E + 02$
	60	$-1.57E + 06$	$3.87E + 03$	$-1.57E + 06$	$8.51E + 02$
	80	$-1.57E + 06$	$3.83E + 03$	$-1.57E + 06$	$1.00E + 03$
	100	$-1.57E + 06$	$3.81E + 03$	$-1.57E + 06$	$8.13E + 02$

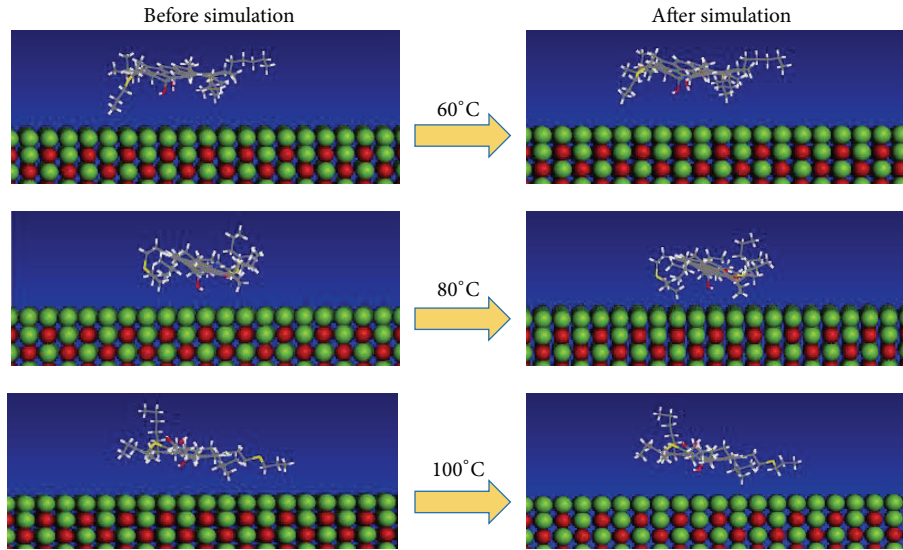
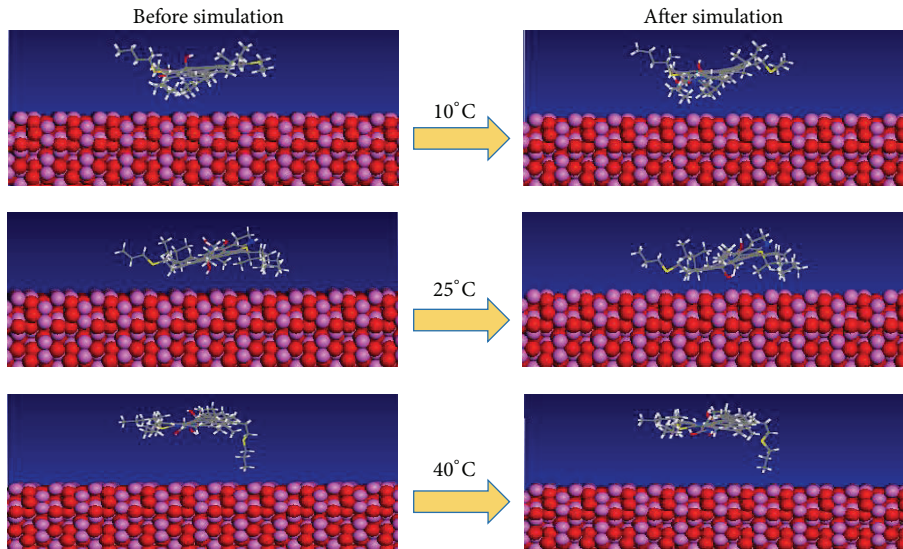


FIGURE 13: The interface configuration of asphaltene/MgO (60–100°C).

FIGURE 14: The interface configuration of asphaltene/Al₂O₃ (10–40°C).TABLE 2: Asphaltene/MgO and asphaltene/Al₂O₃.

	Temp. (°C)	E_{total} (kJ/mol)	E_{polymer} (kJ/mol)	E_{surface} (kJ/mol)	$E_{\text{interface}}$ (kJ/mol)
Asphaltene/MgO	10	$-2.61E + 06$	$3.71E + 03$	$-2.61E + 06$	$1.67E + 03$
	25	$-2.61E + 06$	$3.79E + 03$	$-2.61E + 06$	$1.79E + 03$
	40	$-2.61E + 06$	$3.73E + 03$	$-2.61E + 06$	$1.61E + 03$
	60	$-2.61E + 06$	$3.76E + 03$	$-2.61E + 06$	$1.61E + 03$
	80	$-2.61E + 06$	$3.76E + 03$	$-2.61E + 06$	$1.68E + 03$
	100	$-2.61E + 06$	$3.81E + 03$	$-2.61E + 06$	$1.63E + 03$
Asphaltene/Al ₂ O ₃	10	$-2.01E + 07$	$3.75E + 03$	$-2.01E + 07$	$4.61E + 02$
	25	$-2.01E + 07$	$3.72E + 03$	$-2.01E + 07$	$4.32E + 02$
	40	$-2.01E + 07$	$3.92E + 03$	$-2.01E + 07$	$1.19E + 02$
	60	$-2.01E + 07$	$3.98E + 03$	$-2.01E + 07$	$3.10E + 02$
	80	$-2.01E + 07$	$3.97E + 03$	$-2.01E + 07$	$6.43E + 02$
	100	$-2.01E + 07$	$3.87E + 03$	$-2.01E + 07$	$2.71E + 02$

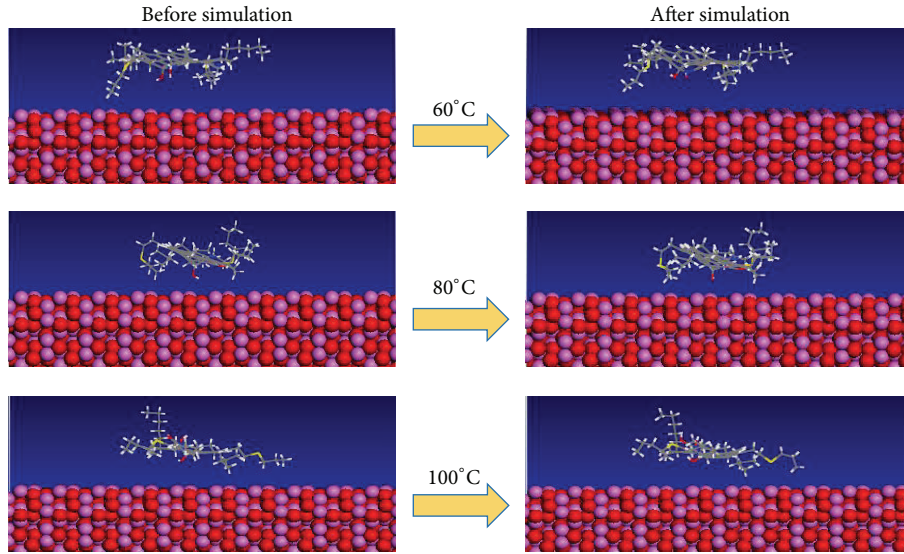


FIGURE 15: The interface configuration of asphaltene/ Al_2O_3 (60–100°C).

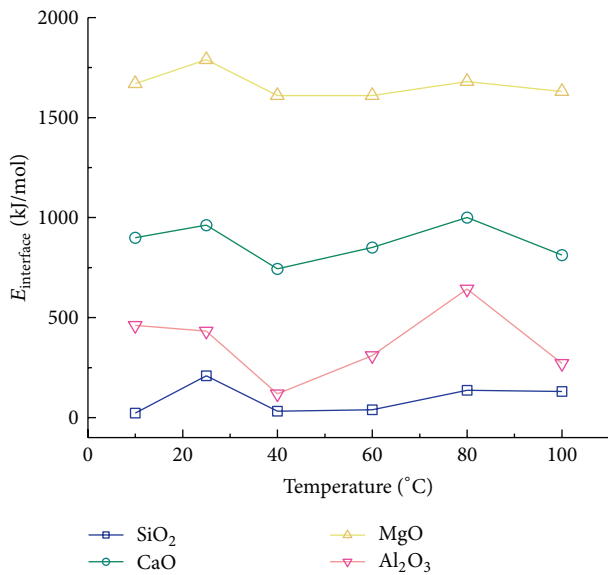


FIGURE 16: The interfacial energy with different temperature.

$1.61E + 03$ to $1.79E + 03$ kJ/mol, and $1.19E + 02$ to $6.43E + 02$ kJ/mol, respectively. Further, the interfacial energy was plotted in Figure 16.

As shown in Figure 16, the four kinds of interfacial energy reach the extreme twice at 25°C and 80°C which indicates stronger interaction between asphaltene and oxides. Within the temperature range of 10°C to 100°C, the interaction capability ranking of the four oxides to asphaltene is as follows: $\text{MgO} > \text{CaO} > \text{Al}_2\text{O}_3 > \text{SiO}_2$.

4. Conclusion

The interaction and the interfacial energy between asphaltene and four kinds of oxides (MgO , CaO , Al_2O_3 , and SiO_2) under

temperature range from 10°C to 100°C were analyzed by virtue of molecular dynamic simulations and the following conclusions can be made: the interaction between asphaltene and oxides reaches strongest level at the temperature of 25°C and 80°C and reaches weakest level at the temperature of 40°C. It could be concluded according to the calculation results of the interfacial energy that the interfacial energy between asphaltene and four kinds of oxides ranges from $2.22E + 01$ kJ/mol to $1.79E + 03$ kJ/mol within the temperature range of 10°C to 100°C. In this temperature range, the interaction capability ranking of the four oxides to asphaltene is as follows: $\text{MgO} > \text{CaO} > \text{Al}_2\text{O}_3 > \text{SiO}_2$.

Conflict of Interests

The authors declare that there is no conflict of interests regarding the publication of this paper.

Acknowledgments

This work is supported by the National Natural Science Foundation of China (Grant nos. 51408048 and 51378037), the Key Program for International Science and Technology Cooperation Projects of Shaanxi province (Grant nos. 2012KW-09 and 2014KW10-03), the China Postdoctoral Science Foundation (Grant nos. 2015M570805 and 2015M582592), the Fundamental Research Funds for the Central Universities of Chang'an University (Grant nos. 310821153502 and 310821152005), and the Research Fund for the Doctoral Program of Higher Education of China (Grant no. 20120205120010).

References

- [1] G. M. Elphinstone, *Adhesion and cohesion in asphalt-aggregate systems [Ph.D. thesis]*, Texas A&M University, College Station, Tex, USA, 1997.

- [2] Y.-Q. Tan, J.-T. Wu, X.-M. Li, and L. Ji, "Evaluation indexes for interaction capability of asphalt and aggregate," *Journal of Harbin Institute of Technology*, vol. 41, no. 7, pp. 81–84, 2009.
- [3] D. Cheng, D. N. Little, R. L. Lytton, and J. C. Holste, "Use of surface free energy properties of the asphalt-aggregate system to predict moisture damage potential," *Journal of the Association of Asphalt Paving Technologists*, vol. 71, pp. 59–88, 2002.
- [4] A. Bhasin, E. Masad, D. Little, and R. Lytton, "Limits on adhesive bond energy for improved resistance of hot-mix asphalt to moisture damage," *Transportation Research Record*, vol. 1970, pp. 3–13, 2006.
- [5] R. Notman and T. R. Walsh, "Molecular dynamics studies of the interactions of water and amino acid analogues with quartz surfaces," *Langmuir*, vol. 25, no. 3, pp. 1638–1644, 2009.
- [6] K. J. Leontaritis, J. O. Amaefule, and R. E. Charles, "Systematic approach for the prevention and treatment of formation damage caused by asphaltene deposition," in *Proceedings of the International Symposium on Formation Damage Control*, pp. 383–395, Lafayette, La, USA, February 1992.
- [7] Y.-F. Li, G.-W. Lu, W. Sun et al., "Study on the molecular dynamics of petroleum-derived asphaltene aggregate," *Acta Petrolei Sinica (Petroleum Processing Section)*, vol. 23, no. 4, pp. 25–31, 2007.
- [8] P. Srivastava, W. G. Chapman, and P. E. Laibinis, "Molecular dynamics simulation of oxygen transport through *n*-alkanethiolate self-assembled monolayers on gold and copper," *The Journal of Physical Chemistry B*, vol. 113, no. 2, pp. 456–464, 2009.
- [9] E. Rogel, "Studies on asphaltene aggregation via computational chemistry," *Colloids and Surfaces A: Physicochemical and Engineering Aspects*, vol. 104, no. 1, pp. 85–93, 1995.
- [10] H. T. Ozkahraman and E. C. Işik, "The effect of chemical and mineralogical composition of aggregates on tensile adhesion strength of tiles," *Construction and Building Materials*, vol. 19, no. 4, pp. 251–255, 2005.

Research Article

Effect of Suction Cycles and Suction Gradients on the Water Retention Properties of a Hard Clay

Liufeng Chen^{1,2} and Hua Peng¹

¹School of Civil and Architectural Engineering, Wuhan University, Wuhan 430072, China

²College of Civil Engineering, Suzhou University of Science and Technology, Suzhou 215011, China

Correspondence should be addressed to Hua Peng; huapeng904@163.com

Received 14 May 2015; Accepted 22 November 2015

Academic Editor: Kisor K. Sahu

Copyright © 2015 L. Chen and H. Peng. This is an open access article distributed under the Creative Commons Attribution License, which permits unrestricted use, distribution, and reproduction in any medium, provided the original work is properly cited.

The effect of suction cycles and suction gradients on a hard clay is investigated. The cylindrical samples of the hard clay are prepared to carry out the hydration and dehydration tests with different suction gradient and suction cycles. The results show that the suction gradient has little effect on the suction-water content relation, while the suction cycle has great effect on it, particularly the first cycle of hydration and dehydration. The apparent moisture diffusion coefficient of the hard clay has been identified by the use of a two-dimensional diffusion model. The moisture diffusion coefficient varies between 4.10^{-11} m²/s and 2.10^{-10} m²/s and it decreases during dehydration while the relative humidity is less than 85%. The results also show that the suction cycles play little effect on the moisture diffusion coefficient.

1. Introduction

In Belgium, a hard clay has been considered as an ideal geological formation for high-level radioactive nuclear waste disposal in Belgium [1, 2], because it has several favourable factors such as low permeability, plasticity, and high retention capacity for radionuclide. The hydromechanical behaviour of the host rock is one of the most important issues in the feasibility studies of the deep geological repository and many studies concerning coupled hydromechanical behaviour and unsaturated behaviour have been carried out [3–5]. Earlier studies show that the mechanical behaviour of clay strongly depends on water content [6, 7] and dehydration and hydration can induce a chemical-physical reaction and change the microstructure of clay and degrade the properties of clay [8–10]. The excavation stage and the open-drift stage of a nuclear waste repository could last a few decades during which the ventilation and temperature conditions will change [11]. The hydromechanical properties of clay could be changed due to cyclic moisture variation. The studies of Wang et al. in 2013 [10] show that different suction gradients play a notable effect on the microstructure of the COx argillaceous rock and larger suction gradients create more microcracks in the clayey matrix than smaller suction gradient during the same suction

range. The microstructure change could affect the water retention properties of the material. The purpose of this study was to investigate the effect of suction cycles and suction gradients on the water retention properties of Boom clay.

2. Material and Methods

2.1. Material and Sample Preparation. In this study, the hydration and dehydration tests have been performed on Boom clay that is a plastic clay. Boom clay contains an average of 55% clay minerals including illite and smectite, 20%–25% quartz, 5%–10% feldspar, and the small content of pyrite (<5%) and calcite (<5%) [12]. The dry density of the material varies between 1.6 and 1.7 g/cm³ [3]. The total porosity of Boom clay is between 36% and 40% [1, 12] and the hydraulic conductivity is around 10^{-12} m/s. Young's modulus of the Boom clay is around 300 MPa and the uniaxial compression strength is about 2 MPa.

The cylindrical sample with a diameter of 36 mm and a length of 10 mm approximately was machined from the cores extracted from the Praclay gallery in the Mol underground research laboratory at a depth of 223 m in Belgium. Special care was taken to assure that the sample was in saturated

TABLE 1: Four different dehydration and hydration paths.

Type	Dehydration and hydration path
A	Saturated state → 98% → 90% → 85% → 81% → 75% → 59% → 43% → 32.5% → 11% → 32.5% → 43% → 59% → 75% → 81% → 85% → 90% → 98%
B	Saturated state → 98% → 75% → 32.5% → 75% → 98% → 75% → 32.5% → 75% → 98% → 75% → 32.5% → 75% → 98%
C	Saturated state → 98% → 81% → 59% → 11% → 98% → 81% → 59% → 11% → 59% → 81% → 98% → 81% → 59% → 11%.
D	Saturated state → 98% → 75% → 32.5% → 75% → 98% → 75% → 32.5% → 75% → 98% → 75% → 32.5% → 75% → 98%.

state. The measurements show that the tested samples had an average water content of 25% at the initial state and dry density of 1.63 g/cm^3 .

2.2. Experimental Method. In order to determine the water retention properties of Boom clay, the suction was imposed by controlling the relative humidity in an airtight container. The relative humidity can be imposed by the use of supersaturated saline solution, which creates a fixed vapour pressure in a sealed container. As shown by Delage et al. in 1998 [13], different values of relative humidity corresponding to the saline solution are listed and they firmly depend on the temperature. The tested samples were placed into the desiccators containing saturated saline solutions at their bottom. Different supersaturated saline solutions (LiCl , $\text{CaCl}_2 \cdot 6\text{H}_2\text{O}$, $\text{K}_2\text{CO}_3 \cdot 2\text{H}_2\text{O}$, NaBr , NaCl , $(\text{NH}_4)_2\text{SO}_4$, KCl , $\text{ZnSO}_4 \cdot 7\text{H}_2\text{O}$, and $\text{CuSO}_4 \cdot 5\text{H}_2\text{O}$) were chosen to cover a large range of relative humidity from 98% to 11%. The corresponding suction at 25°C varies from 2.76 to 301.51 MPa, following the Kelvin law [13]:

$$P_c = -\frac{RT}{M_w V_w} \ln\left(\frac{P}{P_0}\right) = -\frac{RT}{M_w V_w} \ln\left(\frac{HR}{100}\right). \quad (1)$$

P_c is the suction, equal to the absolute difference between the air and water pressures; R is the constant of perfect gases ($R = 8.3143 \text{ J} \cdot \text{mol}^{-1} \cdot \text{K}^{-1}$); T is the absolute temperature ($T = 298 \text{ K}$ at 25°C); M_w is the molar masse of water ($M_w = 18.016 \text{ g} \cdot \text{mol}^{-1}$); V_w is specific volume of water ($V_w = 0.99565 \text{ g} \cdot \text{cm}^{-3}$); P is the partial water vapour pressure; and P_0 is the fact that, at state saturated, their ration is the relative humidity. Note that all the tests are carried out at a constant environment temperature.

The saturated saline solutions used and the corresponding suctions/relative humidity at 20°C have been presented by Delage et al. in [13]. Note that all the tests are carried out at a constant environment temperature (25°C).

2.3. Test Program. To study the effects of suction gradients and suction cycles on water retention properties of Boom clay, four different dehydration and hydration paths were programmed as shown in Table 1. In order to obtain the representative results, a series of samples are submitted to a same hydration or dehydration path. Path A was performed on the six samples (A1–A6) with different heights and it consisted of one cycle of dehydration and hydration with

small suction gradient. Path B was performed on five samples (B1–B5) and it consists of two drying/wetting cycles with small suction gradient. Path C was performed on eight samples (C1–C8) and it is composed of two and a half cycles of hydration and dehydration with large suction gradient. Path D was performed on eight samples (D1–D8) and it consists of three drying/wetting cycles with larger suction gradient. Because of the low permeability of Boom clay, each moisture stage lasted more than one week to reach a stable state. Note that more than five samples were simultaneously tested following the same hydration and dehydration paths to get better confidence in the results.

When the samples reached mass stabilization, the sample was weighted rapidly and then placed in the desiccator to subject to the next hydric loading. Once the whole hydration and dehydration cycles finished, the tested samples were dried in the oven at 105°C to determine the dry weight. The volume of the sample was measured by immersing the waxed samples into water.

3. Experimental Results

3.1. Water Retention Curves. The successive samples weights (M) at the moisture equilibrium were measured and the corresponding water contents (w) were thus determined by comparing the measured weight (M) with the dried weight (M_d) obtained at the end of the test: $w = (M - M_d)/M_d$. All the results concerning the water content show that the samples submitted to the same hydration and dehydration path have close water content change during each moisture phase as shown in Figure 1 which illustrates the water content evolution of the three samples (A1, A2, and A3) following path A. Therefore, the water content evolution observed of the Boom clay in centimetre should be representative to study the water retention curves of the material. We will present only the results of the samples A1, B1, C1, and D1 in order to focus on the effect of suction cycles and suction gradients on the water content properties.

The gravitational water content versus suction of the samples A1, B1, C1, and D1 is plotted in Figures 2(a), 2(b), 2(c), and 2(d), respectively. Similar to the results of Bernier et al. in 1997 [3] and Li et al. in 2006 [1], the water retention curves show that the water content decreases nonlinearly with the increase of suction. The water content variation is relatively larger than that obtained by CIEMAT [3] and close to the results obtained by the researchers of Universitat Politècnica

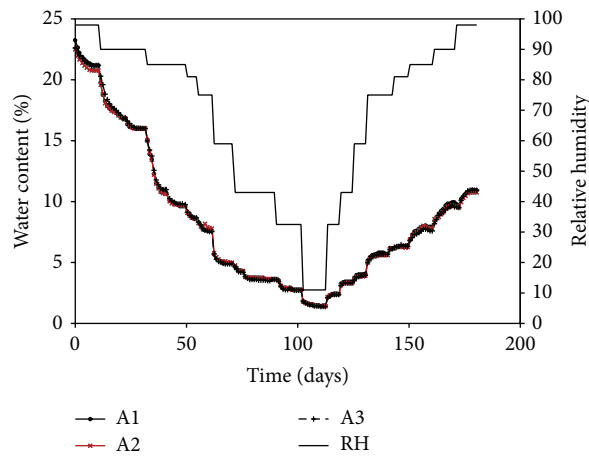


FIGURE 1: Hydration and dehydration path and the corresponding water content evolution of the samples A1, A2, and A3.

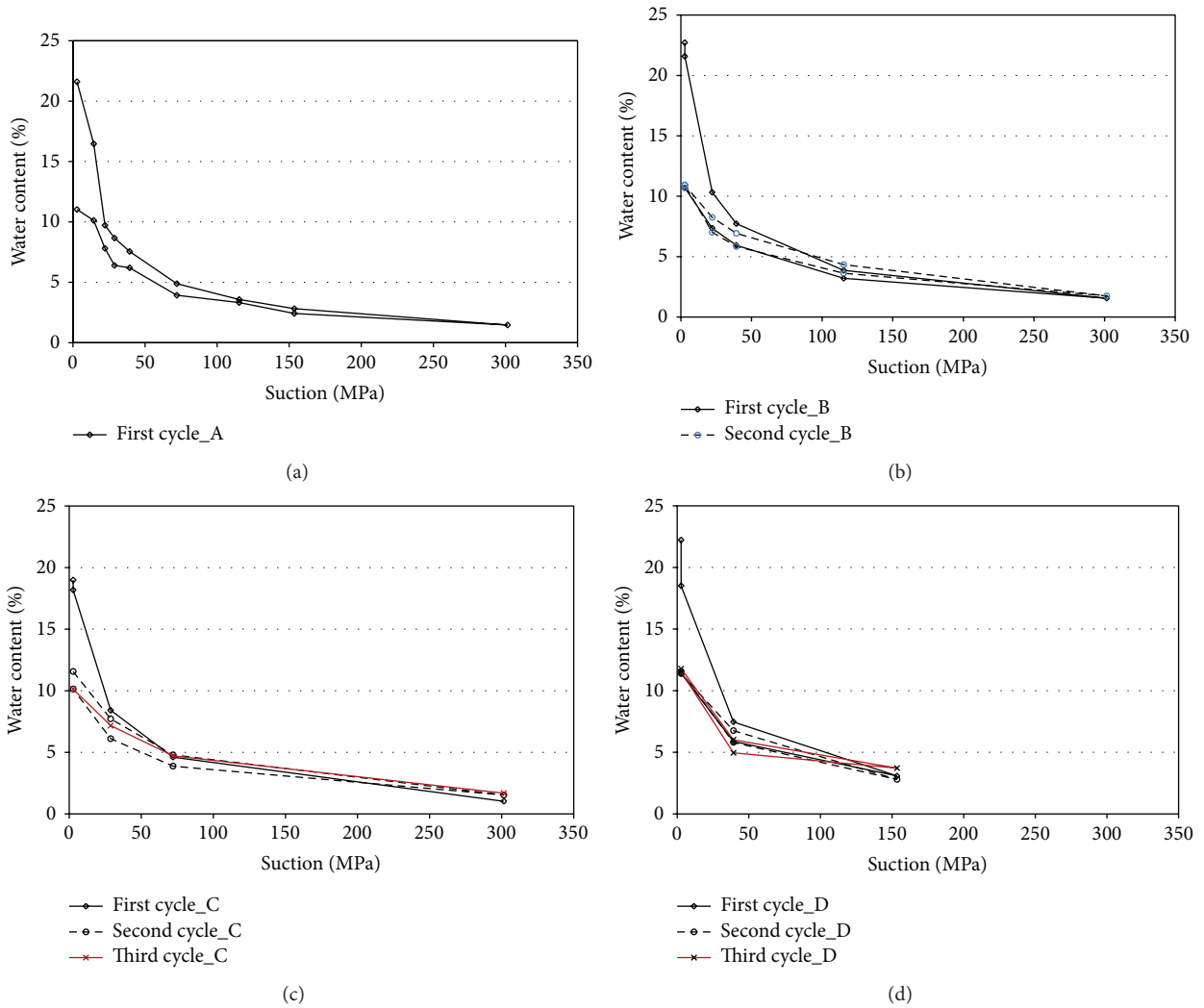


FIGURE 2: The water retention curves of the samples A1, B1, C1, and D1.

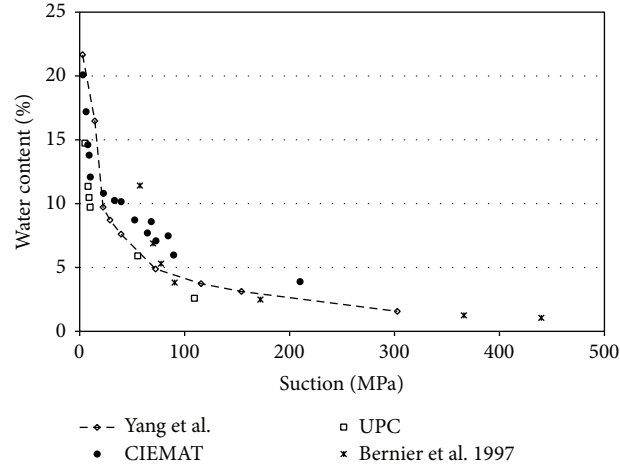


FIGURE 3: The comparison of the water retention curves of different studies.

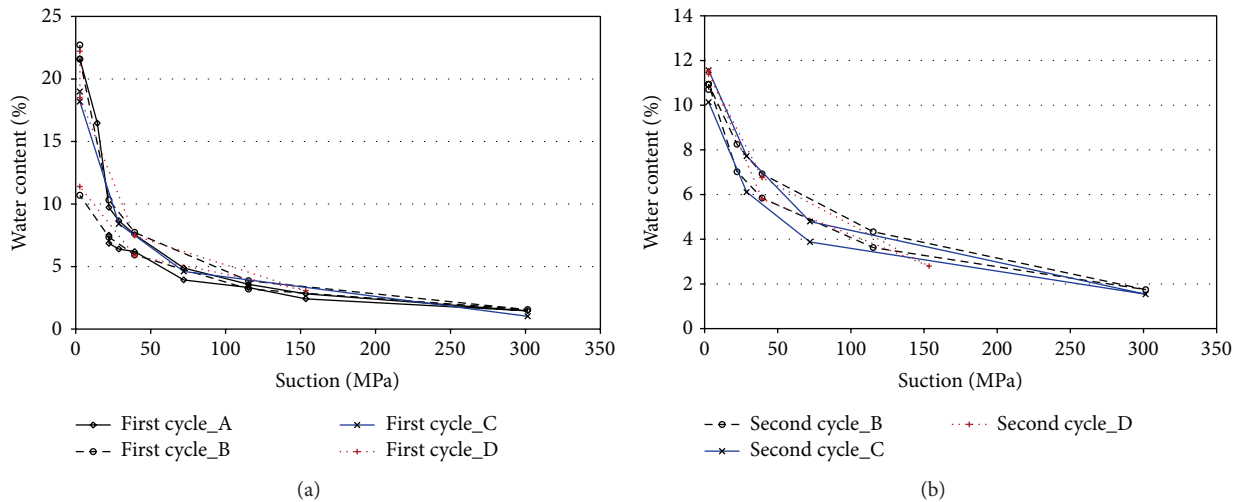


FIGURE 4: (a) Effect of suction gradient on the water retention curves during the first hydric cycle and (b) the second hydric cycle.

de Catalunya (UPC) (Figure 3). The water content decreases greatly during the first desaturation and it losses more than 10% when the suction increases to 29 MPa corresponding to a relative humidity of 81%. The large variation of the water content should be related to both the initial state and the pore size distribution of Boom clay. During the first dehydration, the initial state of the sample is fully saturated and the continuous water will be vapoured and it will induce the shrinkage of Boom clay and lead to a large variation of water content. The first cycle and the second cycle of dehydration and hydration of the four samples (A1, B1, C1, and D1) are, respectively, regrouped in Figures 4(a) and 4(b), which show that the water content of the samples at the same suction level is very close and there is little effect of the suction gradient on the water retention curves. Figures 2(b), 2(c), and 2(d) show also that there is large difference between the first hydric cycle and the second one. However, there is small difference between the second hydric cycle and the third hydric cycle. Moreover, the water content is nearly reversible after the second and third hydric cycle

(Figure 2(d)). Therefore, suction cycles play an important role on the water retention curves, mainly the first dehydration and hydration cycle. The little effect of suction gradient on the water retention properties should be related to small microstructure change during hydration and dehydration which is different from the COx argillaceous rock. The effect of suction cycle on the water retention properties should be mainly related to the pore size distribution as Bernier et al. in 1997 [3] and Coussy in 2010 [15] indicated.

3.2. Moisture Diffusion Coefficient. The dehydration and hydration tests with different paths lasted more than six months. The long test duration should be firmly related to the transfer moisture properties. In fact, the moisture transfer process is complex and it depends on the relative humidity level. At high relative humidity, the capillary phase remains continuous and the moisture transfer is governed by the capillary forces; when relative humidity decreases, the liquid water and the gas (vapour and air) coexist and the moisture transfer is controlled by the exchange between

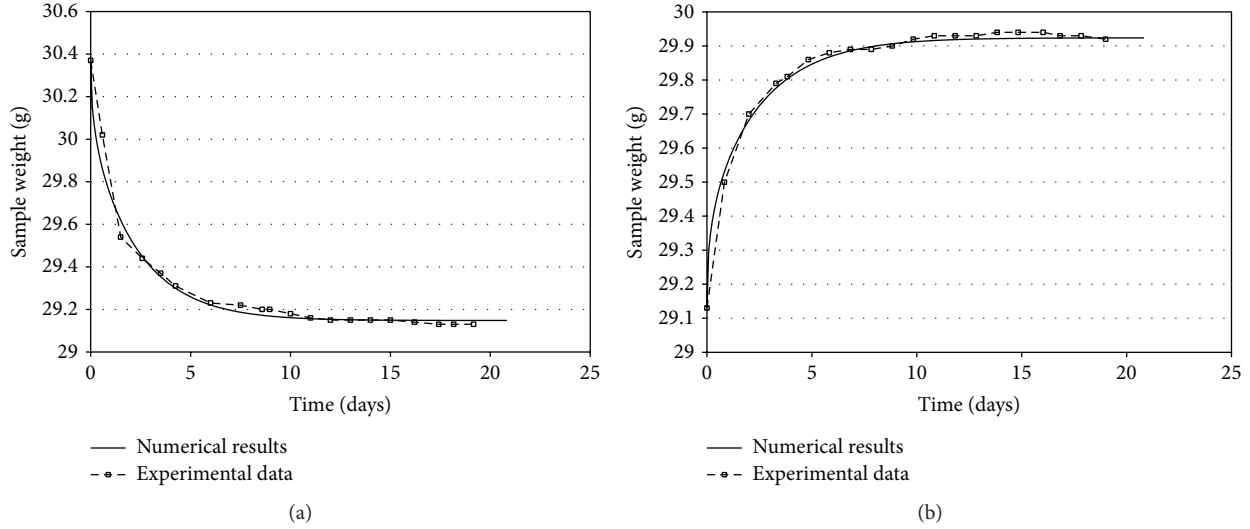


FIGURE 5: (a) Experimental results and the numerical prediction of the weight evolution of the sample D1 during dehydration while the relative humidity (RH) decreases from 75% to 32% (b) and during hydration with the increase of RH from 32% to 75%.

evaporation and condensation; at low relative humidity, the pores are mainly occupied by gas and the moisture transfer is controlled by vapour diffusion [14]. In this study, the apparent moisture diffusion coefficient is used to characterize the transfer properties of Boom clay. Assuming the validity of the mass conservation law and Fick's law [15], the moisture transfer of the cylindrical sample of Boom clay can be expressed using a macroscopic model in two dimensions to simulate the moisture diffusion in the radial direction and the vertical direction:

$$\frac{\partial m_e}{\partial t} = D_e \left(\frac{\partial^2 m_e}{\partial r^2} + \frac{1}{r} \frac{\partial m_e}{\partial r} + \frac{\partial^2 m_e}{\partial z^2} \right). \quad (2)$$

With $0 \leq r < a$, $0 < z < l$ for $t > 0$, where m_e is the volumetric mass water content ($\text{kg}\cdot\text{m}^{-3}$) defined as $m_e = \rho_e \phi S_r$ ($\text{kg}\cdot\text{m}^{-3}$); ρ_e is the water density; ϕ is porosity; S_r is the saturation degree; a is the radius of sample (m) and l is the length (m); and D_e is the apparent moisture diffusion coefficient ($\text{m}^2\cdot\text{s}^{-1}$).

While the initial conditions (porosity, geometric parameters) and boundary conditions (initial and final saturation) are given, the numerical solution of (2) can be obtained by means of the finite difference time domain method. The moisture equilibrium time only depends on D_e . The apparent moisture diffusion coefficient is determined by searching an optimal parameter D_e to minimize the difference between the experimental mass evolution and the numerical solution of (2). Figure 5(a) illustrates the experimental weight evolution of the sample D1 when the relative humidity decreased from 75% to 32% to compare with its numerical solution with a coefficient of diffusion of $1.4 \cdot 10^{-10} \text{ m}^2\cdot\text{s}^{-1}$. Figure 5(b) illustrates the case of hydration. The numerical prediction data fits well with the experimental results. Most of the hydric phases are analysed and the moisture diffusion coefficient of the sample D1 varies from $4 \cdot 10^{-11} \text{ m}^2\cdot\text{s}^{-1}$ to $2 \cdot 10^{-10} \text{ m}^2\cdot\text{s}^{-1}$. It is much smaller at the high relative humidity of 98% than

at the lower humidity level as shown in Figures 6(a) and 6(b) which gives evidence also of the little effect of hydration and dehydration cycle on moisture diffusion coefficient. In fact, the moisture diffusion coefficient is firmly related to the water permeability, which decreases with the diminution of the relative humidity. The results of this study confirm it as shown in Figure 6, even if the apparent diffusion coefficient varies very little during hydration and dehydration when the relative humidity is less than 85%.

4. Conclusions

In order to study the effect of suction cycles and suction gradients on the water retention properties of the hard clay, a series of samples are prepared to carry out dehydration and hydration tests by means of suction controlled technique. Four hydric paths with different suction cycles and suction gradients are programmed and each hydric test has lasted more than six months. The results concerning water content show that the samples following the same hydric path have a very close water content variation during the same suction change and suction gradient has little effect on the suction water content relation, while the suction cycle has great effect on it, particularly the first cycle of hydration and dehydration will change much the suction-water content relation.

Because of the very low permeability, each hydric phase during dehydration and hydration lasted more than one week. The moisture transfer properties of Boom clay were quantified by the use of a two-dimensional diffusion model. The apparent moisture diffusion coefficient of Boom clay varies between $4 \cdot 10^{-11} \text{ m}^2/\text{s}$ and $2 \cdot 10^{-10} \text{ m}^2/\text{s}$. It decreases during dehydration while the relative humidity is less than 85%. The moisture diffusion coefficient is relatively small when the relative humidity is close to 98% and it is about $4 \cdot 10^{-11} \text{ m}^2/\text{s}$. The results show also that the suction cycles play little effect on the moisture diffusion coefficient.

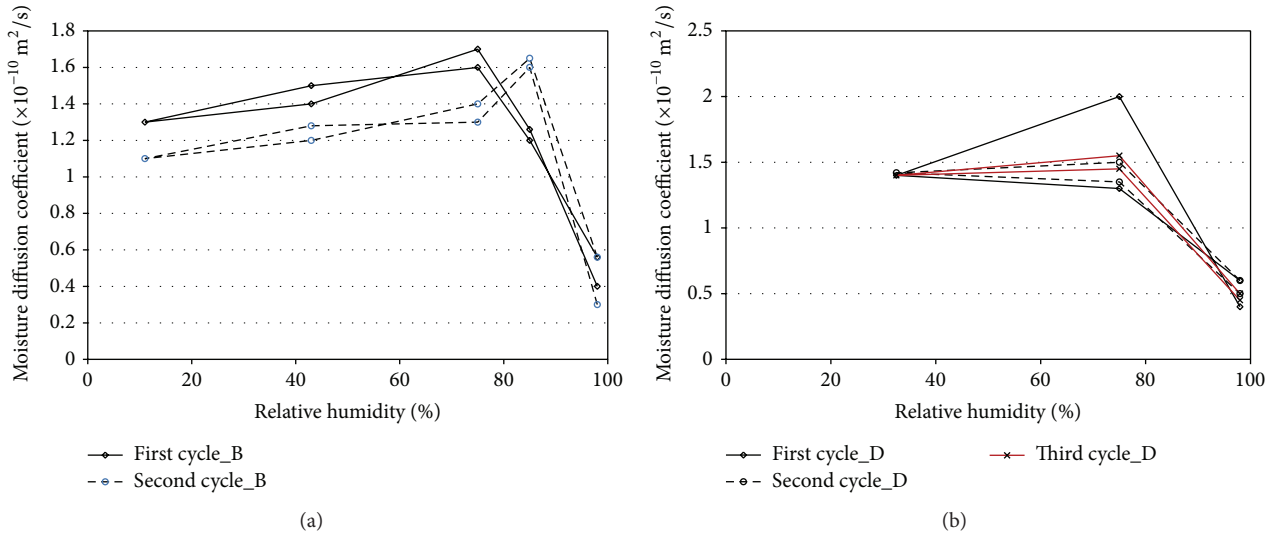


FIGURE 6: (a) The apparent moisture diffusion coefficient of the sample B1 (b) and the sample D1.

Conflict of Interests

The authors declare that they have no conflict of interests.

Acknowledgments

The authors gratefully acknowledge the support of the National Natural Science Foundation of China (Grant nos. 51379200, 51225902). The authors gratefully thank Dr. Diansen Yang for the paper preparation and Professor Weizhong Chen for the helpful discussion.

References

- [1] X. L. Li, W. Bastiaens, and F. Bernier, "The hydromechanical behaviour of the Boom Clay observed during excavation of the connecting gallery at Mol site," in *Proceedings of EUROCK2006-Multiphysics Coupling and Long Term Behaviour in Rock Mechanics, Liege, Belgium*, pp. 467–472, Balkema, Rotterdam, The Netherlands, 2006.
- [2] H.-D. Yu, W.-Z. Chen, S.-P. Jia, J.-J. Cao, and X.-L. Li, "Experimental study on the hydro-mechanical behavior of Boom clay," *International Journal of Rock Mechanics and Mining Sciences*, vol. 53, pp. 159–165, 2012.
- [3] F. Bernier, G. Volckaert, E. Alonso, and M. Villar, "Suction-controlled experiments on Boom clay," *Engineering Geology*, vol. 47, no. 4, pp. 325–338, 1997.
- [4] F. Collin, X. L. Li, J. P. Radu, and R. Charlier, "Thermo-hydro-mechanical coupling in clay barriers," *Engineering Geology*, vol. 64, no. 2-3, pp. 179–193, 2002.
- [5] M. Wan, P. Delage, A. M. Tang, and J. Talandier, "Water retention properties of the Callovo-Oxfordian claystone," *International Journal of Rock Mechanics and Mining Sciences*, vol. 64, pp. 96–104, 2013.
- [6] Q. T. Pham, F. Valès, L. Malinsky, D. N. Minh, and H. Gharbi, "Effects of desaturation-resaturation on mudstone," *Physics and Chemistry of the Earth*, vol. 32, no. 8–14, pp. 646–655, 2007.
- [7] D. S. Yang, M. Bornert, S. Chanchole, H. Gharbi, and P. Valli, "Dependence on moisture content of elastic properties of argillaceous rocks investigated with optical full-field strain measurement techniques," *International Journal of Rock Mechanics and Mining Sciences*, vol. 54, pp. 53–62, 2012.
- [8] E. E. Alonso, J. Vaunat, and A. Gens, "Modelling the mechanical behaviour of expansive clays," *Engineering Geology*, vol. 54, no. 1-2, pp. 173–183, 1999.
- [9] J. Vaunat and A. Gens, "Analysis of the hydration of a bentonite seal in a deep radioactive waste repository," *Engineering Geology*, vol. 81, no. 3, pp. 317–328, 2005.
- [10] L. L. Wang, M. Bornert, S. Chanchole et al., "Micro-scale experimental investigation of the swelling anisotropy of the Callovo-Oxfordian argillaceous rock," *Clay Minerals*, vol. 48, no. 2, pp. 391–402, 2013.
- [11] C.-F. Tsang, F. Bernier, and C. Davies, "Geohydromechanical processes in the Excavation Damaged Zone in crystalline rock, rock salt, and indurated and plastic clays—in the context of radioactive waste disposal," *International Journal of Rock Mechanics & Mining Sciences*, vol. 42, no. 1, pp. 109–125, 2005.
- [12] C. Coll, *Endommagement des roches argileuses et perméabilité induite au voisinage d'ouvrage souterrains [Ph.D. thesis]*, Université Joseph Fourier-Grenoble 1, Grenoble, France, 2005.
- [13] P. Delage, M. D. Howat, and Y. J. Cui, "The relationship between suction and swelling properties in a heavily compacted unsaturated clay," *Engineering Geology*, vol. 50, no. 1-2, pp. 31–48, 1998.
- [14] V. Baroghel-Bouny, "Water vapour sorption experiments on hardened cementitious materials. Part II: essential tool for assessment of transport properties and for durability prediction," *Cement and Concrete Research*, vol. 37, no. 3, pp. 438–454, 2007.
- [15] O. Coussy, *Mechanics and Physics of Porous Solids*, John Wiley & Sons, 2010.

Research Article

Corrosion Inhibiting Mechanism of Nitrite Ion on the Passivation of Carbon Steel and Ductile Cast Iron for Nuclear Power Plants

K. T. Kim,¹ H. W. Kim,¹ H. Y. Chang,² B. T. Lim,² H. B. Park,² and Y. S. Kim¹

¹Materials Research Centre for Energy and Clean Technology, School of Materials Science and Engineering, Andong National University, 1375 Gyeongsongro, Andong 760-749, Republic of Korea

²Power Engineering Research Institute, KEPCO Engineering & Construction Company, 8 Gumiro, Bundang, Seongnam, Gyeonggi 463-870, Republic of Korea

Correspondence should be addressed to Y. S. Kim; yikim@anu.ac.kr

Received 1 July 2015; Accepted 27 September 2015

Academic Editor: Randhir Singh

Copyright © 2015 K. T. Kim et al. This is an open access article distributed under the Creative Commons Attribution License, which permits unrestricted use, distribution, and reproduction in any medium, provided the original work is properly cited.

While NaNO_2 addition can greatly inhibit the corrosion of carbon steel and ductile cast iron, in order to improve the similar corrosion resistance, *ca.* 100 times more NaNO_2 addition is needed for ductile cast iron compared to carbon steel. A corrosion and inhibition mechanism is proposed whereby NO_2^- ion is added to oxidize. The NO_2^- ion can be reduced to nitrogen compounds and these compounds may be absorbed on the surface of graphite. Therefore, since nitrite ion needs to oxidize the surface of matrix and needs to passivate the galvanic corroded area and since it is absorbed on the surface of graphite, a greater amount of corrosion inhibitor needs to be added to ductile cast iron compared to carbon steel. The passive film of carbon steel and ductile cast iron, formed by NaNO_2 addition showed N-type semiconductive properties and its resistance, is increased; the passive current density is thus decreased and the corrosion rate is then lowered. In addition, the film is mainly composed of iron oxide due to the oxidation by NO_2^- ion; however, regardless of the alloys, nitrogen compounds (not nitrite) were detected at the outermost surface but were not incorporated in the inner oxide.

1. Introduction

Since the operation period of nuclear power plants around the world increases each year, the degradations in buried pipes have become an important issue in the nuclear power industry. Many reports have been carried out on the degradation of buried pipes, such as the lining damage of buried pipe for a component cooling seawater system at Hanul #1 unit (Korea), 1998 [1], the leakage of buried pipe for a fire protection system at Hanbit #4 unit (Korea), 2006 [2], and the cooling water leakage (*ca.* 2.27 m^3) at Indian Point #2 unit (USA), 2009 [3]. In the case of buried pipe, its corrosion environment differs from that of air-exposure pipe. While the interior of the pipe becomes corroded by fluids, the outside undergoes mechanical and chemical damage from the soil. Also, even though leakage occurs in the buried

pipe, it is very difficult to determine the reason for the leakage and to fix it timely because of a lack of accessibility. Various pipes of *ca.* 30~40 km per unit of nuclear power plant have been buried and operated, and depending on the application system and water chemistry, they are separately maintained as the large diameter pipes and the other pipes. Large diameter pipes are installed to convey the primary cooling seawater system, the secondary cooling seawater system, and the circulating system, the cooling water of which is seawater [4, 5]. About 70% of pipes are Prestressed Concrete steel Cylinder Pipe (PCCP) and Prestressed Concrete Pipe (PCP). Another pipework has been installed for conveying water for the fire-fighting system, which was made of carbon steel or cast iron [6]. The types of damage that can occur in buried pipe include leakage, fracture, blockage, and deformation by mechanical impact. Secondary damage

TABLE 1: Chemical compositions of experimental alloys.

Alloys	Chemical compositions, wt%										
	C	Mn	P	S	Si	Cr	Cu	Mo	Ni	V	Fe
CS	0.26	0.86	0.014	0.005	0.23	0.04	0.057	0.033	0.029	0.008	bal.
DCI	4.01	0.17	0.022	0.026	1.53	—	0.023	0.028	0.059	0.016	bal.

CS: carbon steel, ASME SA106 Gr.B; DCI: ductile cast iron, KS D4311.

then occurs, including general corrosion, pitting, microbial induced corrosion, scale buildup, multiplication of microbial, and fatigue. Therefore, several corrosion control methods such as painting and coating, electrical protection, and the use of corrosion inhibitors have been applied [7–9]. Carbon steel and cast iron used in a closed cooling system may be corroded. In order to control this type of corrosion problem, corrosion inhibitors such as nitrite, silicate, molybdate, and hydrazine have been used among them; nitrite is widely used because of its excellent performance.

Many reports have been presented on corrosion inhibition by nitrite, including Fe_2O_3 formation on steel by nitrite addition [10], adherent protective oxide on steel [11], correlation of oxygen and nitrite on steel corrosion [12], comparative study of nitrite including various inhibitors on steel [13–15], and inhibition effect of nitrite on steel with time [16, 17]. Nitrite as an anodic inhibitor has a tendency to increase anodic polarization and thus increase corrosion potential to a noble direction and decrease the corrosion current. Since nitrite contains a strong oxidizing power, it oxidizes the surface and forms Fe_2O_3 [18]. Formation rate of protective film due to nitrite is very fast and thus among the several corrosion inhibitors, nitrite shows good performance [19].

On the other hand, ductile cast iron has a very different microstructure to that of carbon steel. Spheroidized graphite forms in the matrix and galvanic corrosion occurs between the matrix and graphite. Also, cast iron does not have high corrosion resistance to various corrosion environments and it should be protected by a coating. As described above, many reports have been presented on the corrosion inhibition of carbon steel but there are few reports on cast iron. Therefore, in this work, corrosion inhibition effects of nitrite on carbon steel and ductile cast iron for nuclear power plant pipework using chemical and electrochemical methods were evaluated. This work attempts to clarify the corrosion inhibition mechanism between steel and iron by NaNO_2 addition.

2. Experimental Procedure

2.1. Materials and Corrosion Environments. Commercial carbon steel (ASME SA106 Gr.B) [20] and ductile cast iron (KS D4311) [21] were used in this work, and Table 1 shows the chemical composition of the experimental alloys.

The test solution was simulated primary cooling water used in the nuclear power plant. The standard solution was 1.6 ppm NaCl and its pH was modified with 1N NaOH solution and the range of $\text{pH } 9 \pm 0.2$ was controlled. NaNO_2 as a corrosion inhibitor was added as a ppm order.

2.2. Corrosion Tests

2.2.1. Immersion Corrosion Test. A specimen was cut to a size of $20 \times 20 \times 5$ mm and each surface was ground using #120 SiC paper. Immersion tests were carried out in a stagnant solution condition (500 mL glass flask) and in a circulating solution, in which test chamber has a dimension of $50 \times 100 \times 50$ cm and the flow rate was 5 L/min. After the immersion tests, each specimen was cleaned with acetone and alcohol and was then dried; the corrosion rate was then determined.

2.2.2. Electrochemical Tests. Specimens were cut to a size of 20×20 mm and, after electrical connection, they were epoxy-mounted and the surface was ground using #600 SiC paper and coated with epoxy resin, except an area of 1 cm^2 . A polarization test was performed using a potentiostat (Gamry DC105) and the reference electrode was a saturated calomel electrode and the counter electrode was Pt wire. The test solution was deaerated using nitrogen gas at the rate of 100 mL/min for 30 minutes and the scanning rate was 0.33 mV/sec. In order to measure the AC impedance, the specimens were ground using #2,000 SiC paper and then polished using a diamond paste ($3 \mu\text{m}$). The test solution was the same as that of the polarization test. AC impedance measurement was performed using an electrochemical analyzer (Gamry EIS 300). Before measuring, passivation was treated at +400 mV(SCE) for carbon steel and 0 mV(SCE) for ductile cast iron for 30 minutes. AC impedance was measured at a passivation potential from 10 kHz to 0.01 Hz and the AC voltage amplitude was 10 mV. Also, a Mott-Schottky plot was prepared to determine the semiconductive properties of the passive film. The specimen preparation was the same as that for AC impedance measurement and the DC amplitude was 10 mV (peak-to-peak) at 1,580 Hz of the AC frequency [22]. The capacitance was measured at the scan rate of 50 mV/sec from +1 V(SCE) to -1.5 V(SCE).

2.2.3. Surface Analysis. X-ray photoelectron spectroscopy (XPS, K-alpha (Thermo VG, UK), Al- K_α (1486.6 eV, 12 kV, 3 mA)) was analyzed to determine the chemical state of several species of the passive film. The specimen was cut to a size of $20 \times 20 \times 5$ mm and then ground with #2000 SiC paper and polished with a $3 \mu\text{m}$ diamond paste; the specimen was finally cleaned with alcohol using an ultrasonic cleaner. Carbon steel and ductile cast iron were passivated by immersion for 24 hours in 1,000 ppm and 100,000 ppm NaNO_2 , respectively. The depth profile was obtained every 5 seconds by Ar-sputtering. Also, an Electron Probe Micro Analyzer (EPMA, EPMA-1600, 15 KV) was used to identify the elemental distribution of the passivated surface. Optical

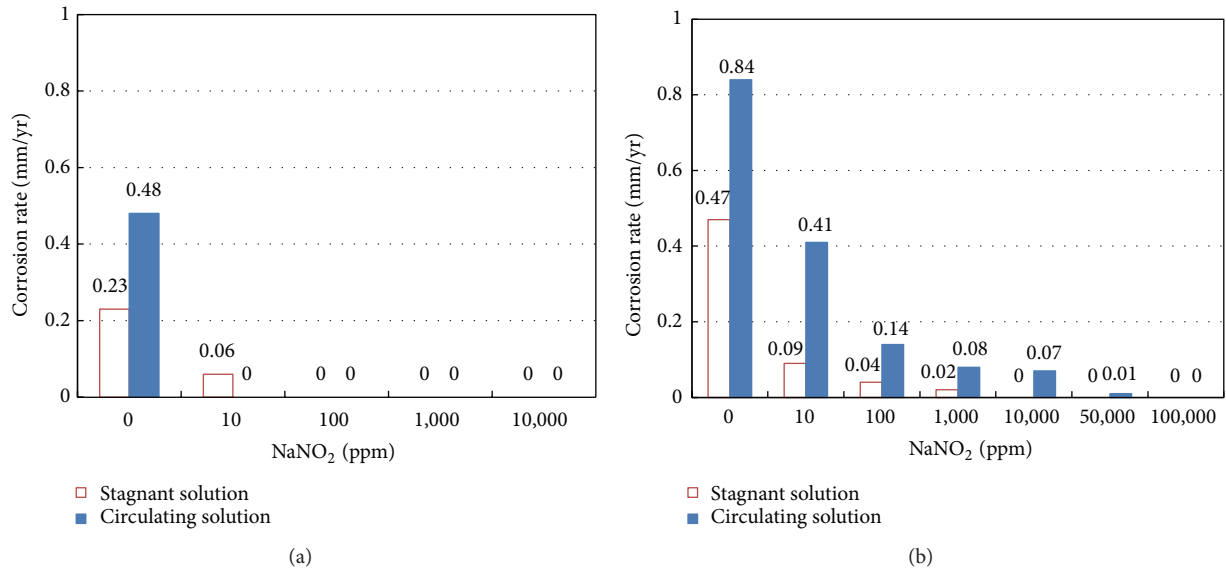


FIGURE 1: Effect of NaNO₂ addition on corrosion rate in circulating and stagnant simulated cooling water at 25°C; (a) carbon steel and (b) ductile cast iron.

Microscope (OM, Zeiss AxioTech 100HD) and SEM-EDS (Tescan Vega II LMU) and a 3D microscope (Zeiss KH-7700) were used.

2.2.4. Corrosion Simulation. In order to determine the difference in galvanic corrosion between the matrix and spheroidized graphite of the ductile cast iron, computer simulation was performed using COMSOL Multiphysics software. Tafel slopes of anodic and cathodic reactions were used and the rate controlling equation applied in this modeling was the secondary corrosion condition.

3. Results and Discussion

3.1. Effect of Nitrite Concentration. Figure 1 shows the effect of NaNO₂ addition on corrosion rate in circulating and stagnant simulated cooling water in the air at 25°C. In the case of carbon steel, increasing NaNO₂ concentration reduced significantly the corrosion rate of carbon steel. When the inhibitor was absent, the rates of stagnant and circulating solutions were 0.23 and 0.48 mm/year, respectively. Also, the effect of nitrite ion was stronger in the circulating solution than in the stagnant solution. However, in the case of ductile cast iron, the effect of nitrite addition was similar to that of carbon steel, but the similar corrosion inhibition of ductile cast iron needs a significant addition of NaNO₂. When the inhibitor was absent, the rates of stagnant and circulating solutions were 0.47 and 0.84 mm/year, respectively. Even though the NaNO₂ addition was increased, the corrosion rate of ductile cast iron showed relatively higher values than those of carbon steel. The corrosion of carbon steel can be inhibited at near 100 ppm NaNO₂ addition, but the corrosion of ductile cast iron can be inhibited by an addition of more than 10,000 ppm NaNO₂. Moreover, while the corrosion of carbon steel can be inhibited more readily by the circulation

of the solution, the circulation facilitated the corrosion of ductile cast iron.

The open circuit potential with immersion time by NaNO₂ addition in circulating (solid symbol) and stagnant (open symbol) simulated cooling water in the air at 25°C was shown in Figure 2. Regardless of the alloys used and the circulation of solution, the open circuit potential of the specimen without NaNO₂ addition decreased with immersion time. However, the open circuit potential of the specimen with NaNO₂ addition increased and its tendency depends on the alloys. In the case of carbon steel, an addition of 100 ppm NaNO₂ increased the open circuit potential and the circulation stimulated its rate. Also, in the case of ductile cast iron, a greater concentration (about 100 times) of NaNO₂ is needed for a similar effect of NaNO₂ addition.

The effect of NaNO₂ addition on the polarization behavior in deaerated simulated cooling water at 25°C was revealed in Figure 3; the scanning rate was 0.33 mV/s. When NaNO₂ is not added, carbon steel and ductile cast iron dissolved readily without the passivation by anodic polarization. With 10 and 100 ppm NaNO₂ additions, carbon steel revealed active-passive transition, but the passive current density was high and transpassive behavior occurred. Ductile cast iron did not show an active-passive transition until a 10,000 ppm NaNO₂ addition. From a 1,000 ppm NaNO₂ addition, carbon steel showed excellent passivation behavior, but the ductile cast iron revealed the best passivation curve from 100,000 ppm NaNO₂ addition. This tendency is coincident with the result of the immersion test shown in Figure 1.

Figure 4 shows the corrosion rate due to the NaNO₂ addition obtained from the immersion test (circulation condition) shown in Figure 1 and the current density was obtained at +400 mV(SCE) as shown in Figure 3. Regardless of the chemical or electrochemical tests, the corrosion of carbon steel can be inhibited by a small NaNO₂ addition

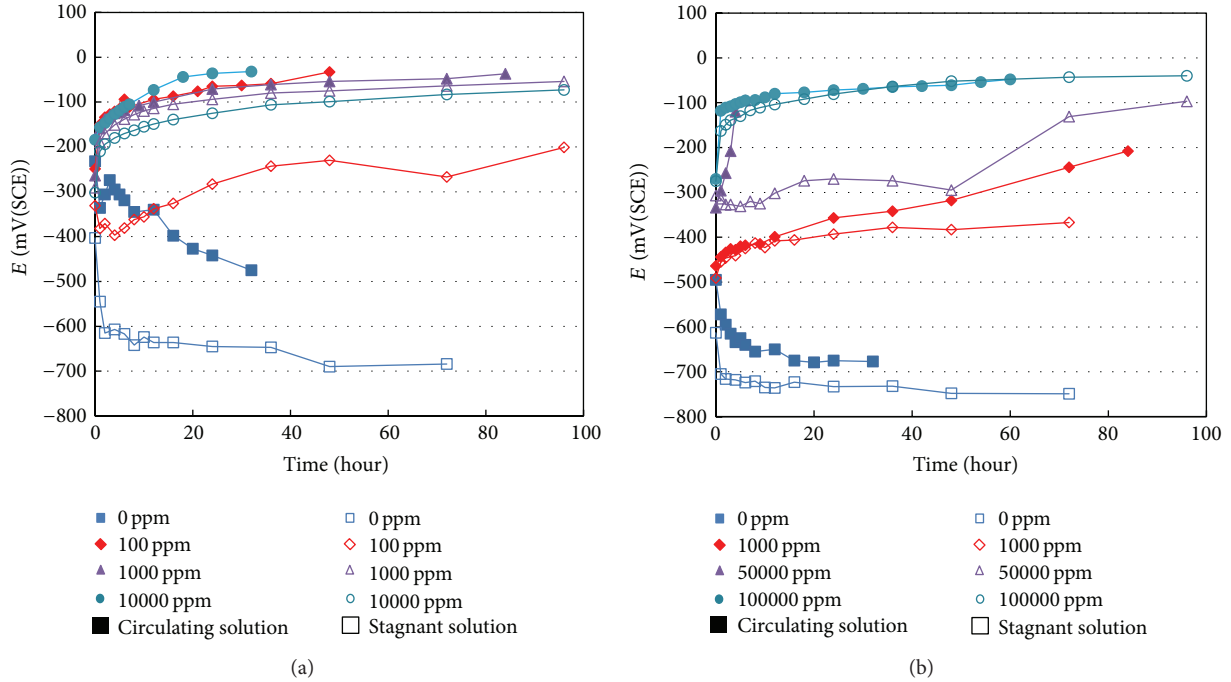


FIGURE 2: Open circuit potential with immersion time by nitrite addition in circulating (solid symbol) and stagnant (open symbol) simulated cooling water at 25°C; (a) carbon steel and (b) ductile cast iron.

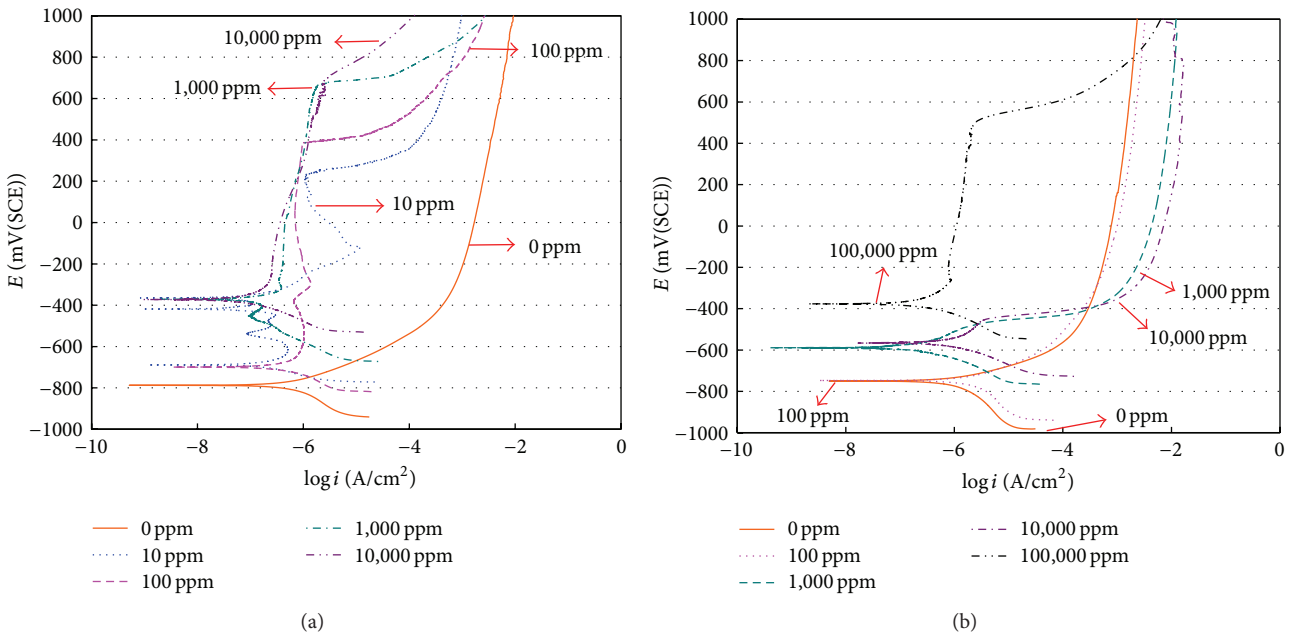


FIGURE 3: Effect of NaNO₂ addition on polarization behavior in deaerated simulated cooling water at 25°C (scanning rate; 0.33 mV/s); (a) carbon steel and (b) ductile cast iron.

(ca. 1,000 ppm), but the corrosion of ductile cast iron could be only inhibited by a significant NaNO₂ addition (ca. 100,000 ppm). That is, it was demonstrated that the difference in the NaNO₂ addition needed between carbon steel and ductile cast iron was about 100 times.

In order to determine the resistance of the passive film formed on the surface of carbon steel and ductile cast iron by NaNO₂ addition, the AC impedance was measured. Figure 5 shows the effect of NaNO₂ addition in Nyquist plot obtained from AC impedance measurement at +400 mV(SCE) for

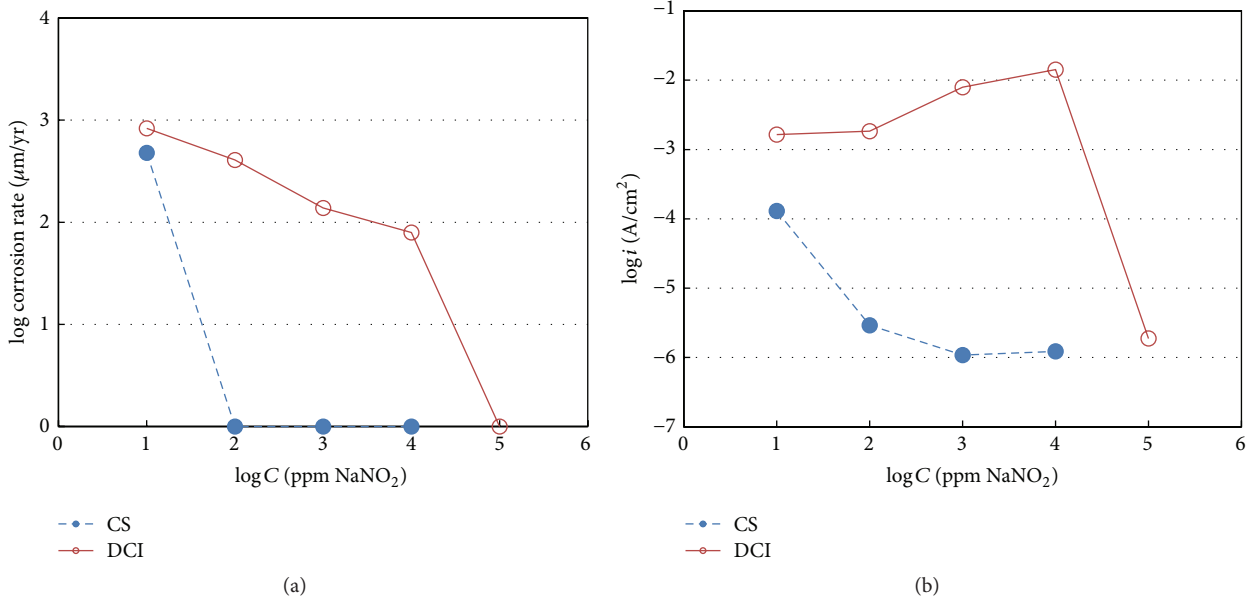


FIGURE 4: Comparison of (a) corrosion rate (circulation condition) from Figure 1 and (b) current density obtained at +400 mV (SCE) of Figure 3 by NaNO₂ addition to simulated cooling water.

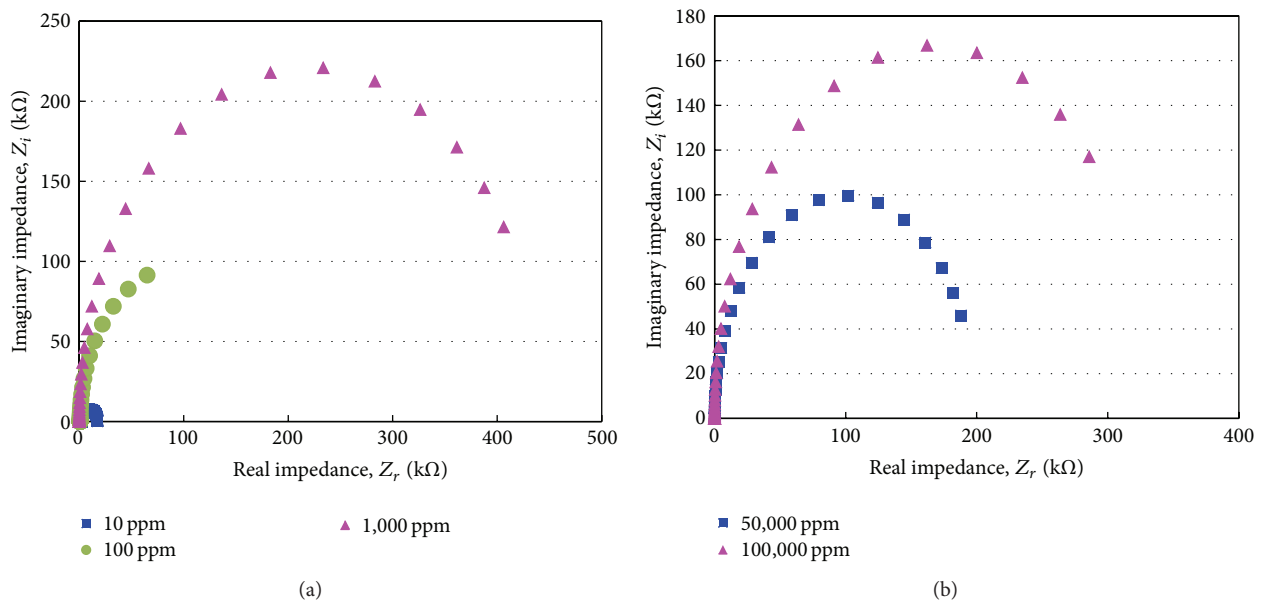


FIGURE 5: Effect of NaNO₂ addition on Nyquist plot obtained from AC impedance measurement in deaerated simulated cooling water at 25°C; (a) carbon steel at +400 mV (SCE) and (b) ductile cast iron at 0 V (SCE).

carbon steel and 0 V(SCE) for ductile cast iron in deaerated simulated cooling water at 25°C. In the case of carbon steel, a stable passive film could not be formed with a 10 ppm NaNO₂ addition and very small impedance (15.6 kohm) was thus shown. A 100 ppm NaNO₂ addition formed a passive film, but its polarization resistance was small (194.6 kohm). However, a stable passive film (442.5 kohm) was formed with a 1,000 ppm NaNO₂ addition. In the case of ductile cast iron, a stable passive film (333.7 kohm) was formed with a 100,000 ppm NaNO₂ addition. As shown in Figures 1 and 4, the difference

of corrosion inhibition between carbon steel and ductile cast iron due to the NaNO₂ addition was closely related to the formation of a stable passive film on the surface.

3.2. Corrosion Inhibition Mechanism of Carbon Steel and Ductile Cast Iron by Nitrite Ion. It was revealed that the difference in the effect of corrosion inhibition due to NaNO₂ addition between carbon steel and ductile cast iron was about 100 times through the immersion test and electrochemical tests as described above. As shown in Table 1, the significant

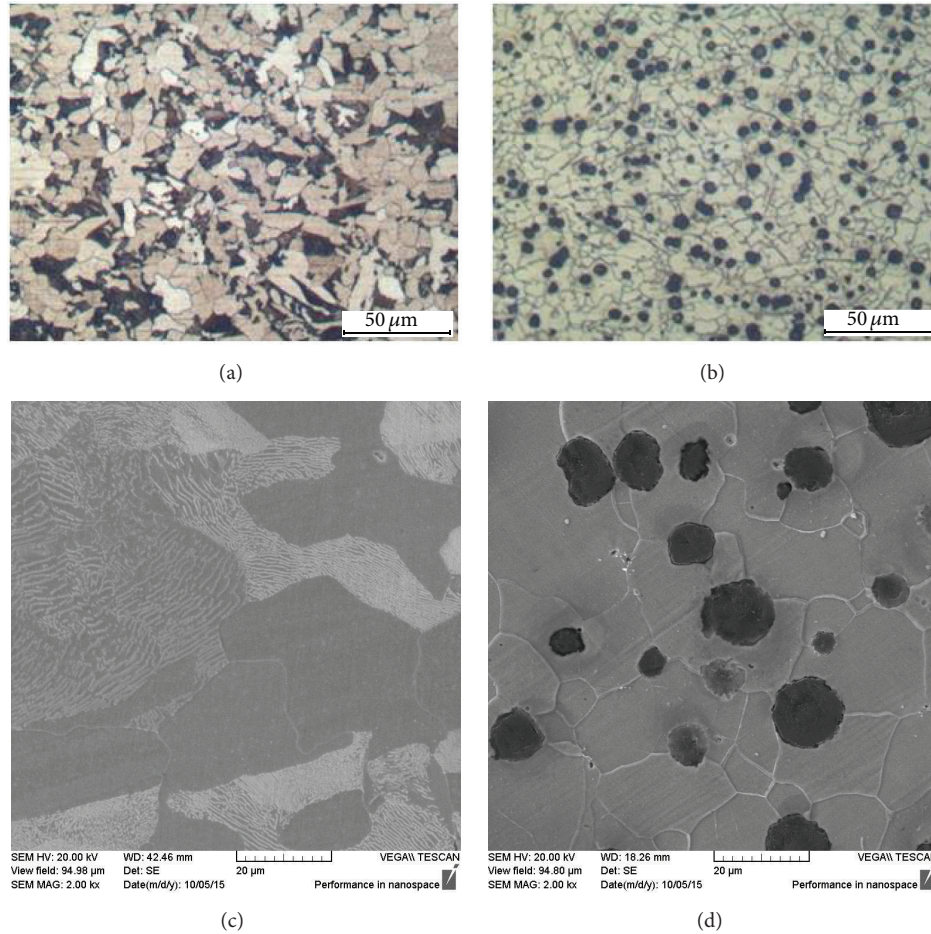


FIGURE 6: Optical microstructures (a, b) and SEM images (c, d); (a, c) carbon steel and (b, d) ductile cast iron.

difference in the composition between the two alloys is carbon content. Figure 6 shows optical microstructures and SEM images for carbon steel and ductile cast iron. In the case of carbon steel, ferrite and pearlite phases can be observed. However, in the case of ductile cast iron, spheroidized phases were formed in the ferrite matrix and the spheroidized phase was shown to be graphite by SEM-EDS analysis. These pictures show the typical microstructures of carbon steel and ductile cast iron.

In order to determine the effect of NaNO_2 addition on the corrosion morphologies of ductile cast iron after immersion, the corroded surface was observed. The effect of NaNO_2 addition on the surface appearance of ductile cast iron after the immersion test in simulated cooling water for 3 hours at 25°C was presented in Figure 7; Figure 7(a) shows the addition of 0 ppm NaNO_2 and Figure 7(b) shows the addition of 10,000 ppm NaNO_2 . When no NaNO_2 was added, the ductile cast iron was generally corroded on the entire surface. However, when 10,000 ppm NaNO_2 was added (this addition of which is not sufficient to inhibit corrosion of ductile cast iron as shown in Figures 1 and 3), the iron was corroded locally near the spheroidized graphite and the corroded areas were agglomerated. Figure 8 shows the corrosion morphologies of ductile cast iron in which ductile cast iron

was corroded for 3 hours in stagnant simulated cooling water (10,000 ppm NaNO_2) at 25°C . Figure 8(a) shows the surface contour using a 3D microscope and local corrosion near the spheroidized graphite was confirmed. Figure 8(b) shows an SEM image of the corroded area, showing that it was corroded spherically near the graphite, and then finally the graphite had chipped off. Also, corrosion products and even cracks were observed near the chipped-off graphite. These figures show that galvanic corrosion took place in the ductile cast iron. It is well known that graphite is nobler than matrix iron [23].

The galvanic corrosion between graphite and matrix iron was simulated using a COMSOL Multiphysics program. Anodic and cathodic Tafel slopes (+108 mV and -206 mV, resp.) were applied to calculate the corrosion behavior of the corroding and noncorroding areas. Figure 9 shows computer 3D simulation results of the corrosion propagation of ductile cast iron occurring in stagnant simulated cooling water (10,000 ppm NaNO_2) at 25°C . At the initial stage (0 hour), the potential difference between graphite (the center) and matrix (left and right) is shown by the blue and red colors, respectively. By increasing the immersion time, the matrix near the graphite corroded and the corrosion depth was increased; its depth was greater near the graphite. (This is the distance effect observed in galvanic corrosion.) This

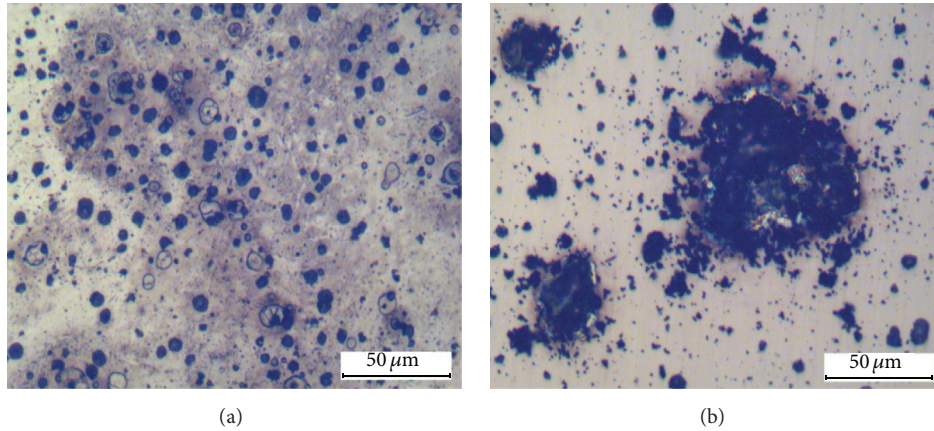


FIGURE 7: Effect of NaNO_2 addition on surface appearance of ductile cast iron after the immersion test in simulated cooling water for 3 hours at 25°C ; (a) 0 ppm NaNO_2 and (b) 10,000 ppm NaNO_2 .

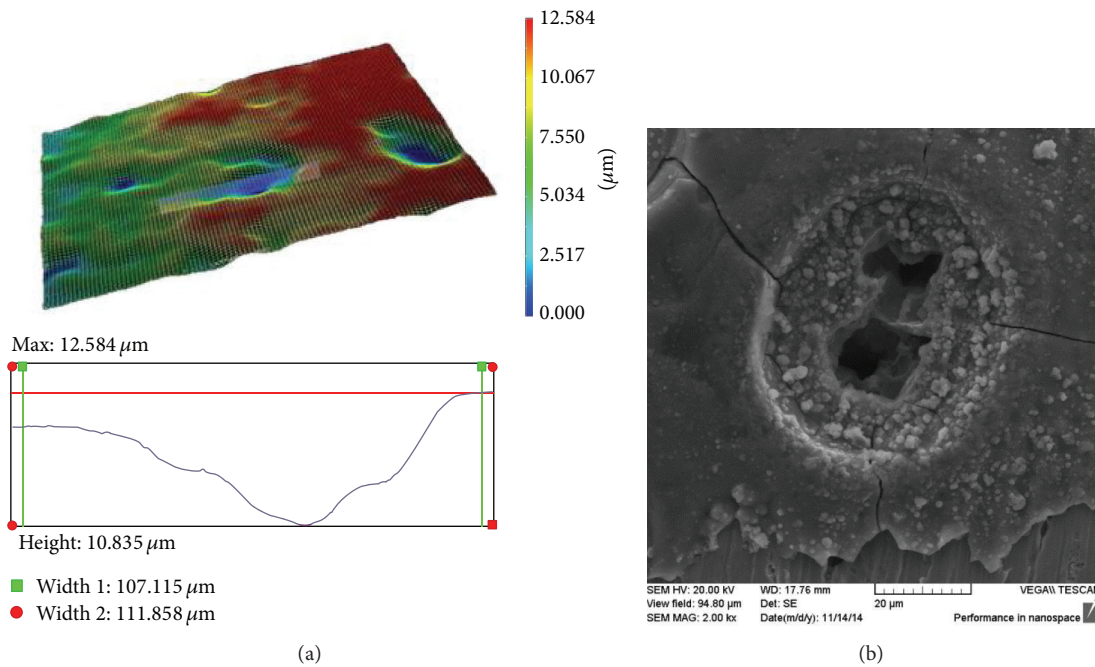


FIGURE 8: Corrosion morphologies of ductile cast iron corroded in stagnant simulated cooling water (10,000 ppm NaNO_2) for 3 hours at 25°C ; (a) 3D microscope and (b) SEM image.

simulation result differs from that shown in Figure 8(b). This difference could be due to the characteristics of the graphite. (However, it should be noted that the COMSOL Multiphysics program does not simulate the mechanical damage in galvanic corrosion.) The crystal structure of graphite is covalent bonded with neighboring atoms in the same layer, although layers are van der Waals bonded together [24, 25] and thus the bonding force of graphite is very weak. Therefore, it is considered that the matrix is corroded galvanically and that the graphite is protruded and then graphite is peeled off layer by layer because of the weak bonding force of graphite.

Figure 10 shows the elemental distribution analyzed using EPMA on the surface of ductile cast iron passivated in

simulated cooling water (100,000 ppm NaNO_2) at 25°C for 72 hours. The SEM image clearly shows the microstructure of ductile cast iron. Fe was depleted in the graphite area and carbon was concentrated as spheroidized shapes. Also, while oxygen was detected on the entire surface, it was particularly concentrated on the graphite area and dim spots of nitrogen were detected. Figure 11 shows the elemental distribution analyzed using EPMA on the surface of ductile cast iron corroded in simulated cooling water (10,000 ppm NaNO_2) at 25°C for 72 hours. The SEM image shows the locally corroded morphology as seen in Figure 7(b). Fe was not uniform and this is related to local corrosion. However, the carbon distribution was very different to the fully passivated

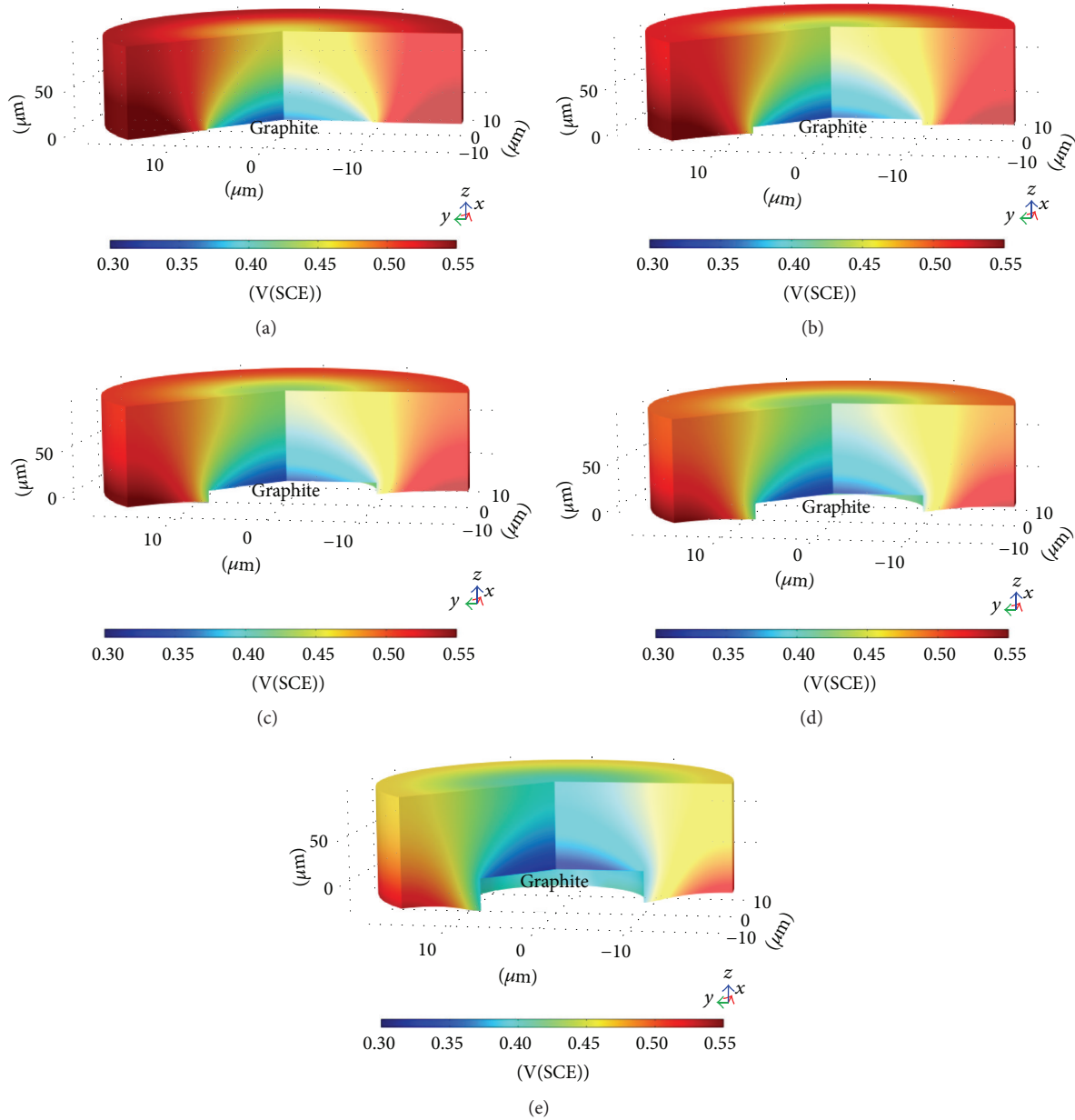


FIGURE 9: Surface electrolyte potential (V(SCE), the right vertical color bar) obtained by computer 3D simulation (the unit of x -, y -, and z -axes; μm) using COSOL Multiphysics on corrosion propagation with immersion time of ductile cast iron occurred in stagnant simulated cooling water (10,000 ppm NaNO_2) at 25°C ; (a) 0 hour, (b) 24 hours, (c) 48 hours, (d) 72 hours, and (e) 144 hours.

surface as shown in Figure 10(c). While spheroidized graphite was not observed, destroyed graphite and its location were identified; this result provides the evidence that graphite can be peeled off layer by layer as discussed above. Oxygen was detected more on the Fe-depleted areas and dim spots of nitrogen were detected. This oxygen comes from the sufficient NaNO_2 . It will be discussed below.

The depth profile on the passivated surface was obtained using XPS to determine the role of nitrite ion on the passivation of steel and iron. Figure 12 shows the depth profile using XPS on the passive film of carbon steel passivated for 24 hours in simulated cooling water (1,000 ppm NaNO_2) at

25°C . Oxygen and nitrogen were enriched at the outer surface and Fe drastically increased with etch time. Figures 12(b) and 12(c) show that iron oxide was enriched at the outer surface. Nitrogen was only detected before sputtering and was not detected at any sputtered depths. This provides evidence that nitrogen is present only on the outermost surface, even with the NaNO_2 addition to the solution. Figure 13 shows the depth profile using XPS on the passive film of ductile cast iron passivated for 24 hours in simulated cooling water (100,000 ppm NaNO_2) at 25°C . Oxygen and nitrogen were enriched at the outer surface and Fe is drastically increased with etch time. Figures 13(b) and 13(c) show that iron oxide

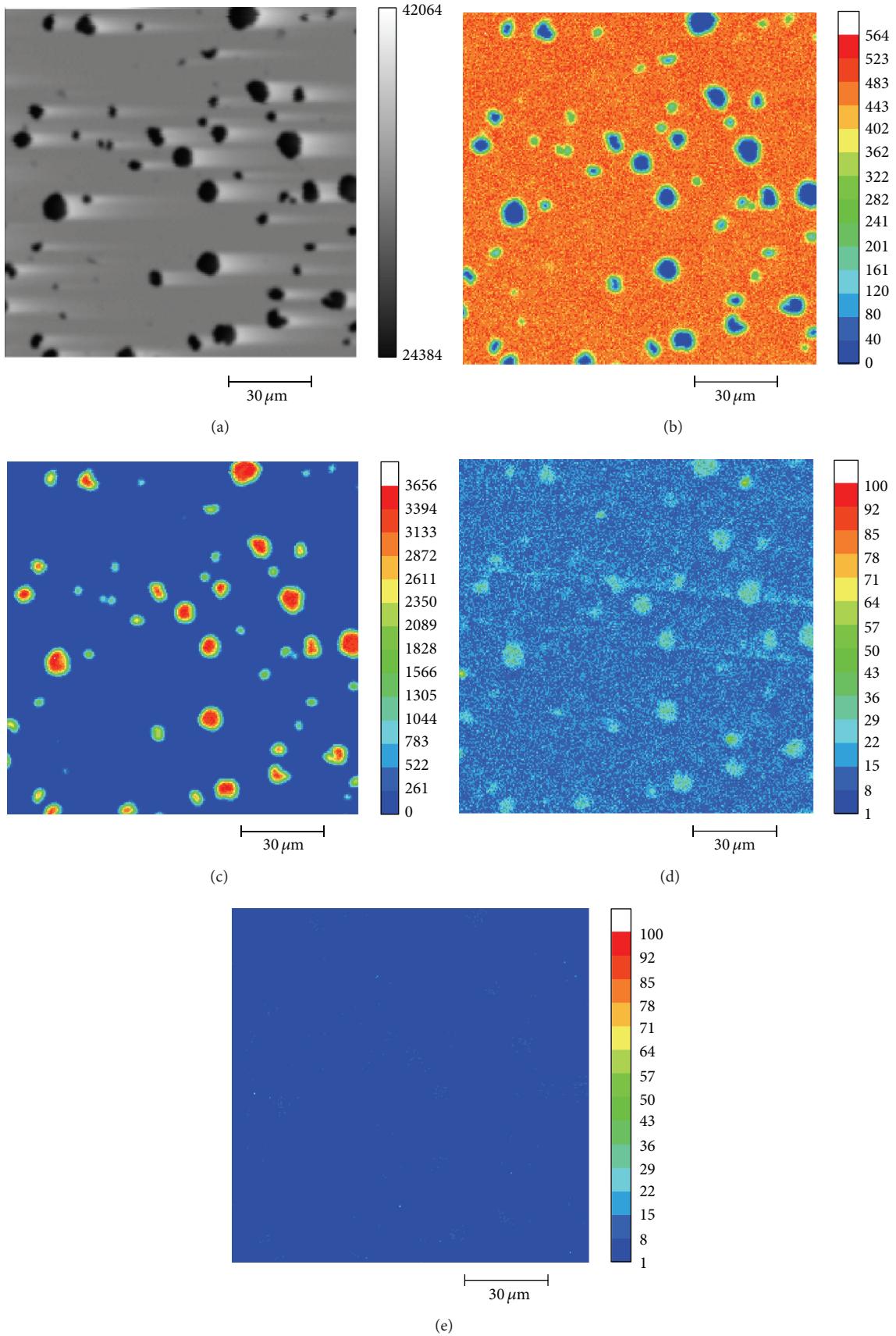


FIGURE 10: Elemental distribution analyzed by EPMA on the surface of ductile cast iron passivated in simulated cooling water (100,000 ppm NaNO_2) at 25°C for 72 hours; (a) SEM image, (b) Fe, (c) C, (d) O, and (e) N.

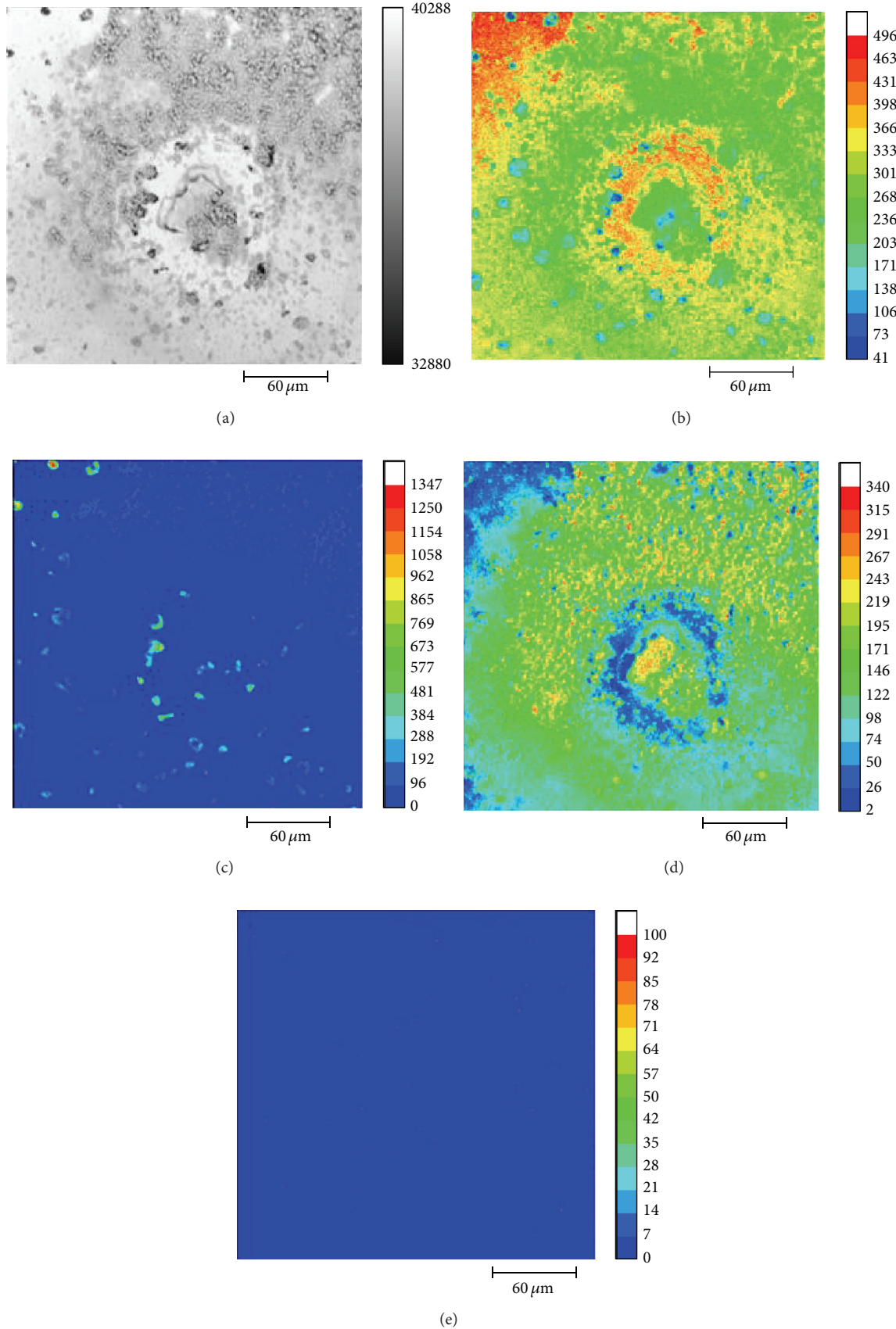


FIGURE 11: Elemental distribution analyzed by EPMA on the surface of ductile cast iron corroded in simulated cooling water (10,000 ppm NaNO_2) at 25°C for 72 hours; (a) SEM image, (b) Fe, (c) C, (d) O, and (e) N.

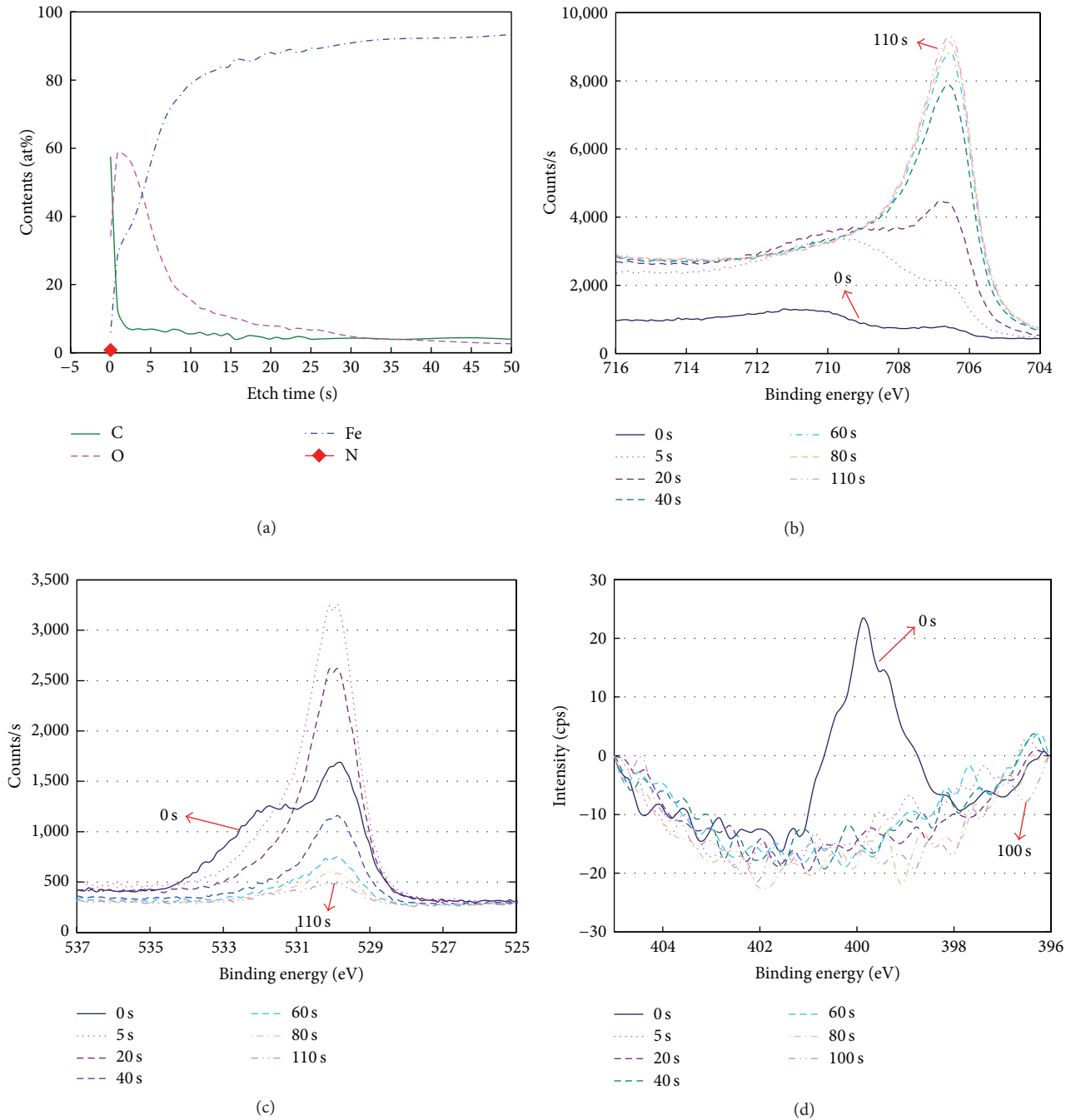


FIGURE 12: Depth profile by XPS on passive film of carbon steel passivated for 24 hours in simulated cooling water (1,000 ppm NaNO₂) at 25°C; (a) depth profile, (b) Fe_{2p} detail scan, (c) O_{1s} detail scan, and (d) N_{1s} detail scan.

was enriched at the outer surface. Nitrogen was only detected before sputtering and at 10 seconds' etch time and was not detected at any sputtered depths. This provides evidence that nitrogen is present only on the outermost surface, even with the NaNO₂ addition to the solution. However, nitrogen of passivated ductile cast iron was detected at a slightly deeper depth than that of the passivated carbon steel. This behavior seems to be related to the corrosion and passivation between graphite and matrix in ductile cast iron.

Figure 14 shows the deconvolution of the chemical species determined by XPS on the surface of (a, b, c) carbon steel passivated in 1,000 ppm NaNO₂ and (a', b', c') ductile cast iron passivated in 100,000 ppm NaNO₂. Regardless of the alloys and sputtering time (0 sec. and 10 sec.), the passive films formed by NaNO₂ addition were composed of iron oxides (Fe²⁺ and Fe³⁺). Also, nitrogen before sputtering exists as nitrogen compounds including NO⁻ (400.4, 399.2 eV), NH₄⁺ (401.1 eV), NH₃ (398.6, 399.8 eV), and NO (399.6 eV)

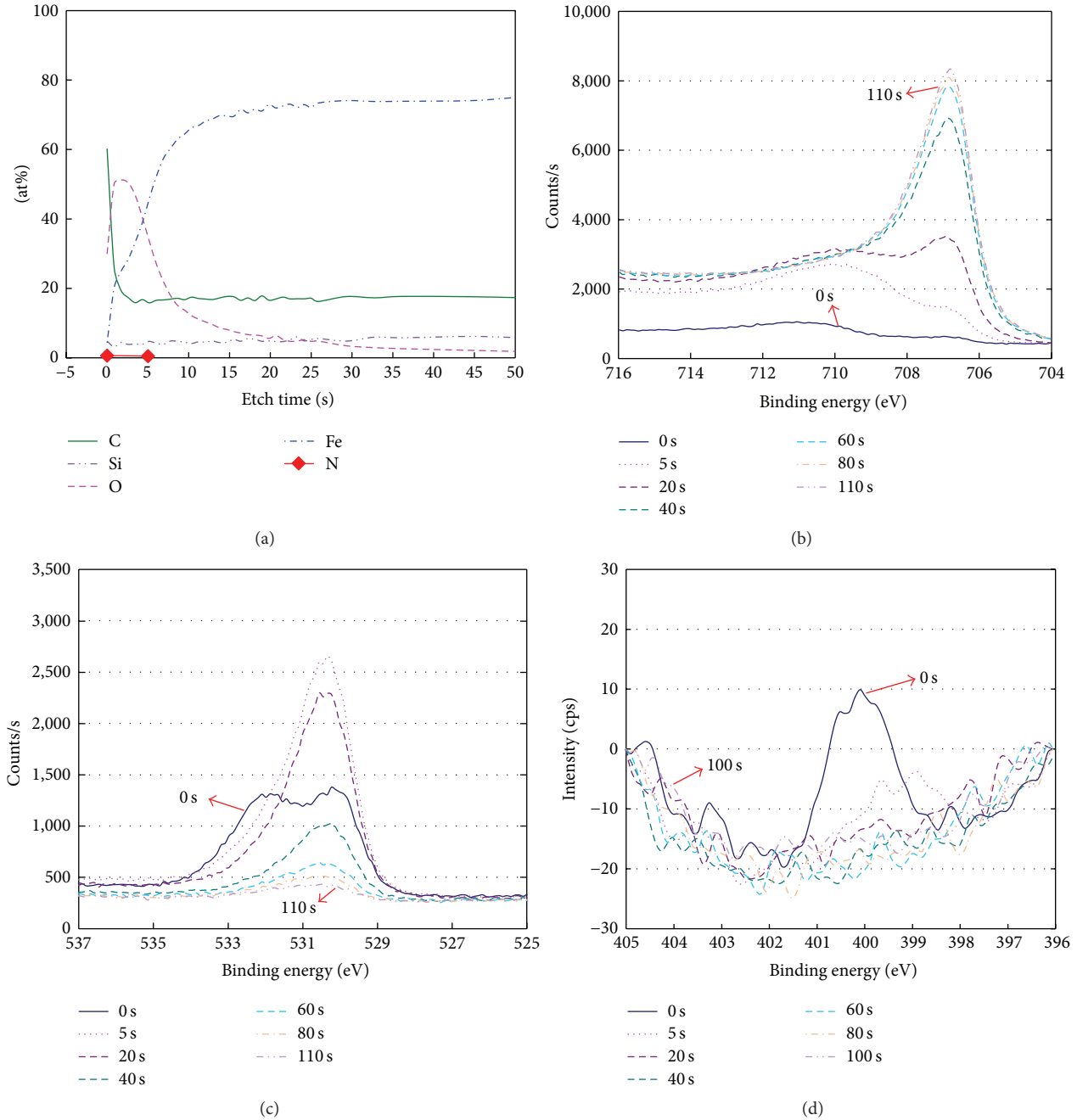


FIGURE 13: Depth profile by XPS on passive film of ductile cast iron passivated for 24 hours in simulated cooling water (100,000 ppm NaNO₂) at 25°C; (a) depth profile, (b) Fe_{2p} detail scan, (c) O_{1s} detail scan, and (d) N_{1s} detail scan.

[26, 27]. However, it should be noted that the chemical states of nitrogen on the passivated surface are not easy to identify by XPS.

Therefore, as discussed above, corrosion and its inhibition model can be proposed as follows. Figure 15 shows the corrosion and inhibition steps of ductile cast iron with nitrite addition. When no corrosion inhibitor is used, general corrosion and galvanic corrosion occur simultaneously and thus the surface may show relatively uniform corrosion (Figure 15(a)). Also, when the amount of corrosion inhibitor is insufficient

(e.g., 10,000 NaNO₂), some area may be passivated (red line) and galvanic corrosion can occur; finally, the iron then reveals localized corrosion (Figure 15(b)). However, when a sufficient corrosion inhibitor (e.g., 100,000 ppm NaNO₂ in Figure 15(c)) is used (even though galvanic corrosion between graphite and matrix has occurred), the entire surface can be passivated and thus corrosion can be inhibited. Also, it should be noted that NO₂⁻ ion is used to oxidize the matrix and can itself be reduced to nitric oxide; this compound can be absorbed on the surface of graphite and thus the enriched

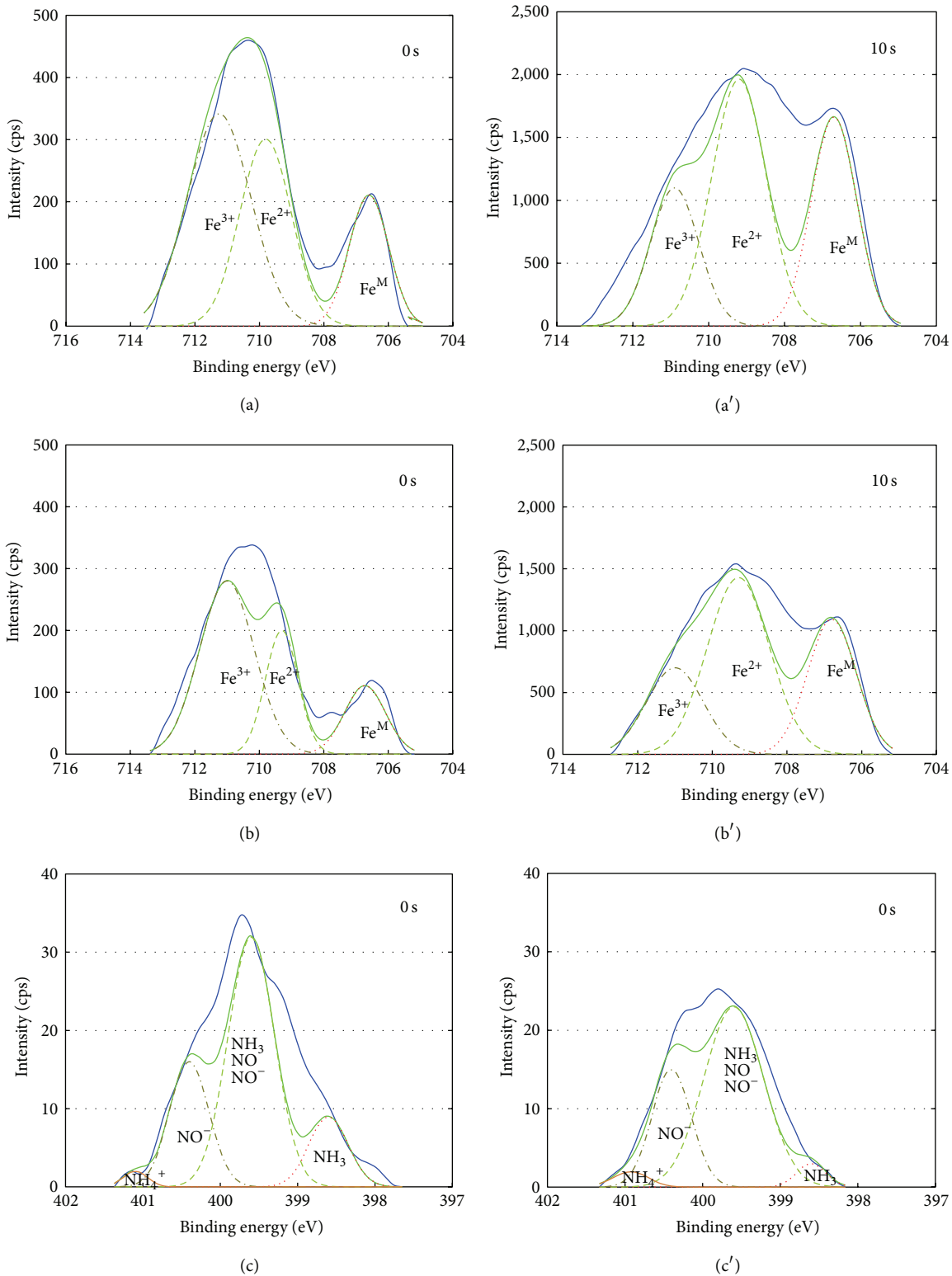


FIGURE 14: Deconvolution of the chemical species determined by XPS on the surface of (a, a', c) carbon steel passivated in 1,000 ppm NaNO₂ and (b, b', c') ductile cast iron passivated in 100,000 ppm NaNO₂; (a) and (a') Fe 2p, (b) and (b') Fe 2p, and (c) and (c') N 1s.

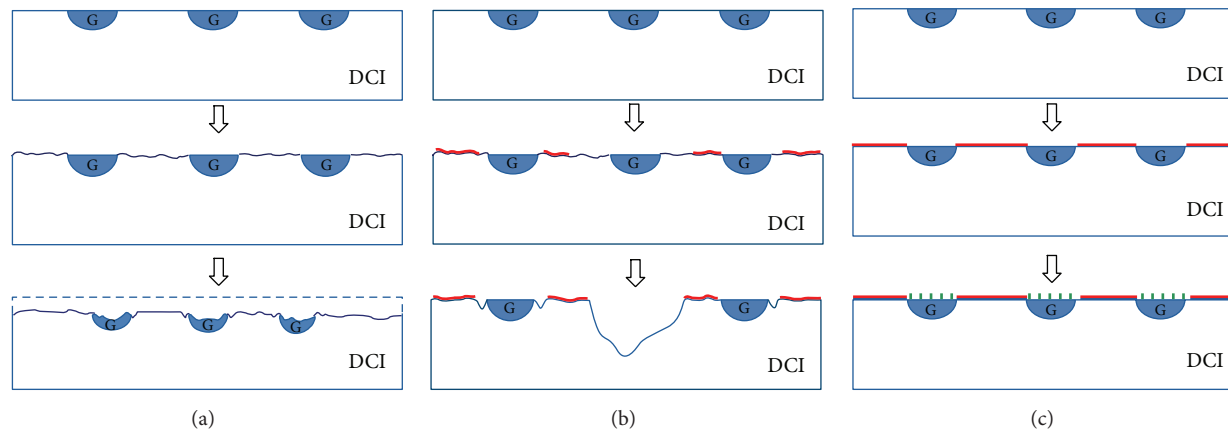


FIGURE 15: Corrosion and inhibition steps with nitrite addition of ductile cast iron; (a) without corrosion inhibitor, (b) with insufficient corrosion inhibitor (10,000 ppm NaNO_2), and with sufficient corrosion inhibitor (100,000 ppm NaNO_2) (G; graphite, red line; metallic oxide, dot line; nitrogen compound).

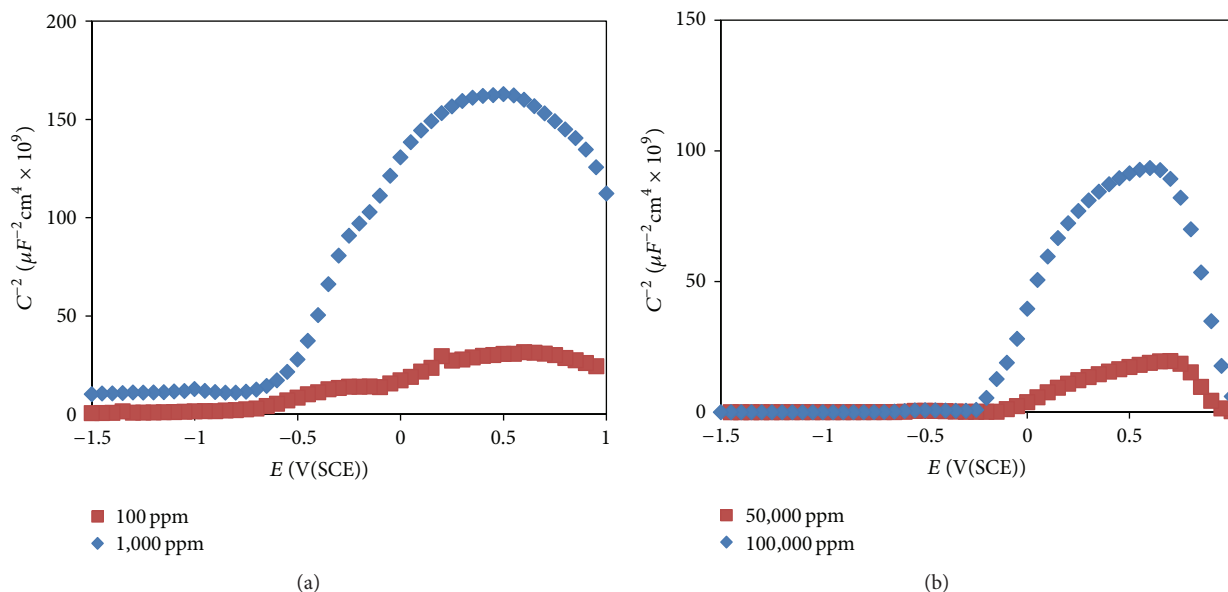


FIGURE 16: Effect of NaNO_2 addition on Mott-Schottky plot for the passive film formed in deaerated simulated cooling water at 25°C ; (a) carbon steel at +400 mV (SCE) and (b) ductile cast iron at 0 mV (SCE).

nitrogen compounds could be detected in the EPMA and XPS results. Therefore, since nitrite ion needs to oxidize the surface of the matrix and needs to passivate the galvanic corroded area and since it is absorbed on the surface of graphite, a larger amount of corrosion inhibitor is needed for ductile cast iron than for carbon steel.

On the other hand, passivated film of various alloys exhibits semiconductive properties [28–30]. Acquisition of Mott-Schottky plots is a usual way for semiconductor materials electrochemical characterization. Mott-Schottky plot (inverse square of space charge layer capacitance, C_{sc}^{-2} , versus semiconductor electrode potential E) gives doping density by slope of the straight line and flat band potential by intercept [31]. A positive slope in the plot indicates the N-type semiconductive properties. Figure 16 shows a Mott-Schottky

plot of the effect of NaNO_2 addition for the passive film formed in deaerated simulated cooling water at 25°C . Regardless of the alloys, the increasing inhibitor concentration strengthened the N-type properties. Also these plots revealed the N-type semiconductive properties of the passivated surface film due to nitrite addition.

4. Conclusions

- (1) While NaNO_2 addition can greatly inhibit the corrosion of carbon steel and ductile cast iron, in order to improve the similar corrosion resistance, *ca.* 100 times more NaNO_2 addition is needed for ductile cast iron than for carbon steel. A corrosion and inhibition mechanism is proposed whereby NO_2^- ion is added

to oxidize. The NO_2^- ion can be reduced to nitrogen compound and this compound may be absorbed on the surface of graphite. Therefore, since nitrite ion needs to oxidize the surface of matrix and needs to passivate the galvanic corroded area and since it is absorbed on the surface of graphite, a greater amount of corrosion inhibitor needs to be added to ductile cast iron than to carbon steel.

- (2) The passive film of carbon steel and ductile cast iron, formed by NaNO_2 addition, showed N-type semi-conductive properties and its resistance is increased; the passive current density is thus decreased and the corrosion rate is then lowered. In addition, the film is mainly composed of iron oxide due to the oxidation by NO_2^- ion; however, regardless of the alloys, nitrogen compounds (not nitrite) were detected at the outermost surface but were not incorporated in the inner oxide.

Conflict of Interests

The authors declare that there is no conflict of interests regarding the publication of this paper.

Acknowledgment

This work was supported by the Nuclear Power Core Technology Development Program of the Korea Institute of Energy Technology Evaluation and Planning (KETEP) granted financial resource from the Ministry of Trade, Industry & Energy, Republic of Korea (no. 20131520000100).

References

- [1] Plant Shutdown Caused by the Crack of the Essential Service Water System Concrete Pipe, Incident Report 7285: Hanul #1, Republic of Korea, 1998.
- [2] Firewater Supply Valve Downstream Buried Piping Leakage of Intake Area, Equipment Failure Report 06-Hanbit 4-1: Hanbit #4, Republic of Korea, 2006.
- [3] USNRC, "Generic aging lessons learned (GALL) report," Tech. Rep. NUREG-1801, Rev. 2, Division of Regulatory Improvement Programs, 2010.
- [4] EPRI, "Nondestructive evaluation; guided wave technology development and nuclear application assessment," Tech. Rep. EPRI-1015156, 2007.
- [5] EPRI, "Condition assessment of large-diameter buried piping; phase 2-vehicle design and construction," EPRI 1011829, EPRI, 2005.
- [6] NRC Inspection Manual, "Inspection of structures, passive components, and civil engineering features at nuclear power plants," Inspection Procedure 62002, United States Nuclear Regulatory Commission (USNRC), 1996.
- [7] E. McCafferty, *Introduction to Corrosion Science*, Springer, New York, NY, USA, 2009.
- [8] V. S. Sastri, *Corrosion Inhibitors, Principles and Applications*, Wiley, London, UK, 1998.
- [9] K. N. Mohana and A. M. Badiea, "Effect of sodium nitrite-borax blend on the corrosion rate of low carbon steel in industrial water medium," *Corrosion Science*, vol. 50, no. 10, pp. 2939–2947, 2008.
- [10] M. Cohen, "Inhibition of steel corrosion by sodium nitrite in water," *Journal of the Electrochemical Society*, vol. 93, no. 1, pp. 26–39, 1948.
- [11] R. Pyke and M. Cohen, "Rate of breakdown and mechanism of nitrite inhibition of steel corrosion," *Journal of the Electrochemical Society*, vol. 93, no. 3, pp. 63–78, 1948.
- [12] M. Cohen, R. Pyke, and P. Marier, "The effect of oxygen on inhibition of corrosion by nitrite," *Journal of The Electrochemical Society*, vol. 96, no. 4, pp. 254–261, 1949.
- [13] S. M. Matsuda and H. H. Uhlig, "Effect of pH, sulfates, and chlorides on behavior of sodium chromate and nitrite as passivators for steel," *Journal of the Electrochemical Society*, vol. 111, no. 2, pp. 156–161, 1964.
- [14] W. D. Robertson, "Molybdate and tungstate as corrosion inhibitors and the mechanism of inhibition," *Journal of the Electrochemical Society*, vol. 98, no. 3, pp. 94–100, 1951.
- [15] M. J. Pryor and M. Cohen, "The inhibition of the corrosion of iron by some anodic inhibitors," *Journal of the Electrochemical Society*, vol. 100, no. 5, pp. 203–215, 1953.
- [16] S. Karim, C. M. Mustafa, Md. Assaduzzaman, and M. Islam, "Effect of nitrite ion on corrosion inhibition of mild steel in simulated cooling water," *Chemical Engineering Research Bulletin*, vol. 14, pp. 87–91, 2010.
- [17] Y. T. Horng and Y. L. Tsai, "An investigation of mild steel with nitrogen-containing inhibitor in hydrochloric acid," *Corrosion Science and Technology*, vol. 2, no. 5, pp. 233–237, 2003.
- [18] L. Abosrra, M. Youseffi, and A. F. Ashour, "Effectiveness of calcium nitrite in retarding corrosion of steel in concrete," *International Journal of Concrete Structures and Materials*, vol. 5, no. 1, pp. 65–73, 2011.
- [19] R. Mehra and A. Soni, "Inhibition of corrosion of mild steel by nitrite, hydrogen phosphate and molybdate ions in aqueous solution of sodium chloride," *Indian Journal of Engineering & Materials Sciences*, vol. 9, no. 2, pp. 141–146, 2002.
- [20] ASME, *ASME Boiler & Pressure Vessel Section II—Part A, 'Ferrous Materials Specifications (Beginning to SA-450)'*, ASME, 2011.
- [21] Korean Agency for Technology and Standards, *KS D4311 Ductile Iron Pipe*, Korean Agency for Technology and Standards, Gyeonggi-do, South Korea, 2010.
- [22] D. D. Macdonald, "The point defect model for the passive state," *Journal of the Electrochemical Society*, vol. 139, no. 12, pp. 3434–3449, 1992.
- [23] Y. S. Kim, S. J. Park, and Y. R. Yoo, "Galvanic corrosion behavior between carbon steel bolted GECM(graphite epoxy composite material)/Al plates," *Corrosion Science and Technology*, vol. 12, no. 1, pp. 19–33, 2013.
- [24] P. Q. Dai, Z. R. He, W. Q. Wu, and Z. Y. Mao, "Mechanical behaviour of graphite in fracture of austempered ductile iron," *Materials Science and Technology*, vol. 18, no. 9, pp. 1052–1056, 2002.
- [25] J. R. Davis, *ASM Specialty Handbook: Cast Irons*, ASM International, Novelt, Ohio, USA, 1996.
- [26] C. D. Wagner, W. H. Riggs, L. E. Davis, J. F. Moulder, and G. E. Muilenberg, *Handbook of X-Ray Photoelectron Spectroscopy*, Perkin-Elmer, 1979.
- [27] Y. S. Kim, "Synergistic effect of nitrogen and molybdenum on localized corrosion of stainless steel," *Corrosion Science and Technology*, vol. 9, no. 1, pp. 20–28, 2010.

- [28] H. J. Jang, "Study on the semiconducting properties of the passive films formed on Ni-Cr alloys in pH 8.5 buffer solution," *Journal of Advanced Engineering and Technology*, vol. 2, no. 2, pp. 285–289, 2009.
- [29] A. Di Paola, "Semiconducting properties of passive films on stainless steels," *Electrochimica Acta*, vol. 34, no. 2, pp. 203–210, 1989.
- [30] C. Sunseri, S. Piazza, and F. Di Quarto, "Photocurrent spectroscopic investigations of passive films on chromium," *Journal of the Electrochemical Society*, vol. 137, no. 8, pp. 2411–2417, 1990.
- [31] A. S. Bondarenko and G. A. Ragoisha, "Variable Mott-Schottky plots acquisition by potentiodynamic electrochemical impedance spectroscopy," *Journal of Solid State Electrochemistry*, vol. 9, no. 12, pp. 845–849, 2005.

Research Article

Gas-Cooled Thorium Reactor with Fuel Block of the Unified Design

Igor Shamanin, Sergey Bedenko, Yuriy Chertkov, and Ildar Gubaydulin

National Research Tomsk Polytechnic University, 30 Lenin Avenue, Tomsk 634050, Russia

Correspondence should be addressed to Sergey Bedenko; bedenko@tpu.ru

Received 5 June 2015; Revised 11 August 2015; Accepted 16 August 2015

Academic Editor: Amritendu Roy

Copyright © 2015 Igor Shamanin et al. This is an open access article distributed under the Creative Commons Attribution License, which permits unrestricted use, distribution, and reproduction in any medium, provided the original work is properly cited.

Scientific researches of new technological platform realization carried out in Russia are based on ideas of nuclear fuel breeding in closed fuel cycle and physical principles of fast neutron reactors. Innovative projects of low-power reactor systems correspond to the new technological platform. High-temperature gas-cooled thorium reactors with good transportability properties, small installation time, and operation without overloading for a long time are considered perspective. Such small modular reactor systems at good commercial, competitive level are capable of creating the basis of the regional power industry of the Russian Federation. The analysis of information about application of thorium as fuel in reactor systems and its perspective use is presented in the work. The results of the first stage of neutron-physical researches of a 3D model of the high-temperature gas-cooled thorium reactor based on the fuel block of the unified design are given. The calculation 3D model for the program code of MCU-5 series was developed. According to the comparison results of neutron-physical characteristics, several optimum reactor core compositions were chosen. The results of calculations of the reactivity margins, neutron flux distribution, and power density in the reactor core for the chosen core compositions are presented in the work.

1. Introduction

Nowadays in many countries nuclear power development programs are established. In the Russian Federation federal special-purpose program “New Generation Nuclear Power Technologies for 2010–2015 and Perspective to 2020” was adopted. The basis of this program is a new technological platform: closed nuclear fuel cycle (CNFC) and fast neutron reactors.

Researches aimed at developing nuclear technologies capable of including natural uranium and thorium into the nuclear fuel cycle correspond to the new technological platform. First of all these are the technologies of CNFC and fast neutron reactors (BN-600, BN-800, and BN-1200 reactor types) and innovative projects of perspective types of low-power reactors and nuclear power reactors (10–100 MWt).

In recent years, a great variety of research works in the field of low-power reactors has been presented. A small modular reactor on fast neutrons with sodium coolant created by Toshiba and ARC-100 construction promoted by Advanced

Reactor Concepts are considered to be the most developed projects.

In Russia, the demonstration block “BREST-300-OD,” which will be put into operation at Siberian Chemical Combine by 2020, meets the well-developed concepts of low-power fast reactors. It is expected to be a new link of the perspective model of CNFC in Russia [1].

Another development direction in a small modular niche is occupied by high-temperature and super high-temperature reactors. In this direction a number of designs and detailed schemes with temperatures from 900 to 1500 K were presented, high-temperature gas-cooled reactors being the most advanced [2–10].

It is obvious that low-power nuclear reactors are not an original idea. However, the projects on designing thorium fuel reactors on their basis are considered very perspective in the field of nuclear power industry. Besides, the market of low-power nuclear reactors with thorium fuel can be very advantageous in Russia.

The purpose of the research is to develop the concept of a thorium low-power safe reactor based on the fuel block of the unified design.

It is supposed that during implementation of the concept all new available knowledge in the field of nuclear reactor industry and physics of neutrons will be applied. Development of the concept will allow starting a range of works which in their turn will result in the project of high-temperature gas-cooled thorium reactor (HTGTR) and further commercial realization.

It should be noted that in Russia nuclear technologies connected with commerciality of thorium low-power reactors are innovative, technically and economically are not investigated and are associated with significant financial investments.

2. Analysis of Information Materials of the Use of Thorium as Nuclear Power Plants Fuel

Due to calculation and experimental information (ENDSF (Evaluated Nuclear Structure Data File), EXFOR (Experimental Nuclear Reaction Data)) about neutron resonance absorption by thorium and uranium nuclei, one specific peculiarity can be reported. In the neutrons energy interval from 4 to 30 eV, when they interact with nuclei of U-238, two significantly powerful resonances with amplitudes of 11 000 and 8 000 barns (the cross section of absorption depends on the energy) can be observed. When neutrons interact with nuclei of Th-232 in the same energy interval, there is resonance of about 300 barns, but the amplitude is negligible in comparison with the resonances in the case with U-238. This peculiarity allowed explaining an important fact discovered in numerical experiments. When raw U-238 in oxide fuel composition (U, Pu)O₂ was substituted by raw Th-232, optimum ratio of the water (moderator) volume to the fuel volume in a multiplying system from fuel pins with the diameter to 0.012 m increased significantly (5 times). Numerical experiments were performed at the Institute of Safety and Reactor Technologies Researches (ISR-2) of Forschungszentrum Juelich (Germany, 1998-1999). In the researches physics of WWER reactors operating in long and super long fuel-element lifetimes (up to 10 years) on thorium, highly enriched uranium and plutonium were studied [11].

In further numerical experiments [11–13] and experimental works (the works were carried out on the basis of research reactor IRT-T, unique id of the works: RFMEFI59114X0001) one peculiarity (anomaly) was determined by the dependence of resonance absorption on the ratio of the moderator volume to the fuel volume in multiplying thorium system ((m% U, n% Th)O₂, (m% Pu, n% Th)O₂), operating in thermal neutrons spectrum. The anomaly lies in the fact that at fixed value of the characteristic size of the nuclear fuel elements in a definite interval of changes of the moderator volume ratio to the fuel volume ($V_{\text{mod}}/V_{\text{fuel}}$) there is sharp increase of the resonance neutrons absorption. In this interval the resonance absorption for uranium system exceeds absorption for plutonium by 3 and more times. Numerical experiments were carried out for multiplying systems with light-water and

graphite moderators. Anomaly manifested in case of graphite at characteristic sizes of the fuel kernel (300–400) microns.

Much smaller resonance absorption in the case when raw nuclide is Th-232 provides two main advantages. The first one is that strong internal block-effect in distribution of epithermal neutrons flux distribution in the fuel kernel volume, which results in absorption of decelerating neutrons in relatively thin marginal layers, is much smaller in thorium systems. As a result integral fission quantity in nuclear fuel element increases at unchanged size. It provides great increase of fuel use efficiency, due to increase of lifetime as well. The second one is that in thorium system there is bigger amount of the moderator. It causes significant increase of thermal inertia with all ensuing advantages such as safety and reliability [3, 4, 6, 11–16].

The numerical researches and experiments, the results of which were presented above, were carried out for fuel compositions, plutonium, and highly enriched U-235 served as an igniter in start-up loading of the reactor core (RC). Thus physics of the fuel composition and reactors neither in thorium-uranium nor in uranium-plutonium NFC was studied. In case of (m% Pu, n% Th)O₂ composition it was thorium-plutonium NFC with the maximum possible burn-up of fissionable nuclides of uranium, and plutonium formed and was burnable during nuclear fuel lifetime.

The results and the peculiarities of neutrons resonance absorption obtained in multiplying grids with thorium point out the necessity to change traditional design solutions for the grids, if the raw nuclide is Th-232.

The works performed within the framework of three state contracts (state contract number P777, 2010; agreement number 14.B37.21.0473, 2012; agreement number 14411.9990019.05110, 2014) allowed reviewing the decision for multiplying grids with thorium. Optimization of geometrical characteristics of fuel assemblies and nuclear fuel composition, particles size, and coatings of microcapsulated fuel (microfuel) dispersed into graphite of the fuel blocks of HTGTR operating with the maximum burn-up was made. The received scientific results and solutions made it possible to start complex neutron-physical calculations of HTGTR.

3. Calculation Model of the High-Temperature Gas-Cooled Thorium Nuclear Power Reactor

Design solutions accepted for HTGTR and neutron-physical characteristics necessary for comparison determined the reactor calculation model and the degree of RC elements specification.

Calculation model of HTGTR was created using MCU-5 program [17]. Geometrical module of MCU-5 allows simulating 3D systems with different complexity geometry using combinatorial approach based on description of complicated systems by combinations of elementary bodies and surfaces.

Detailed models of fuel pellets (FP) with heterogeneous fuel kernels, fuel assemblies, and RC of HTGTR were created. The temperature of all elements of the RC and core reflector was considered to be 1200 K. Realized in MCU possibilities of

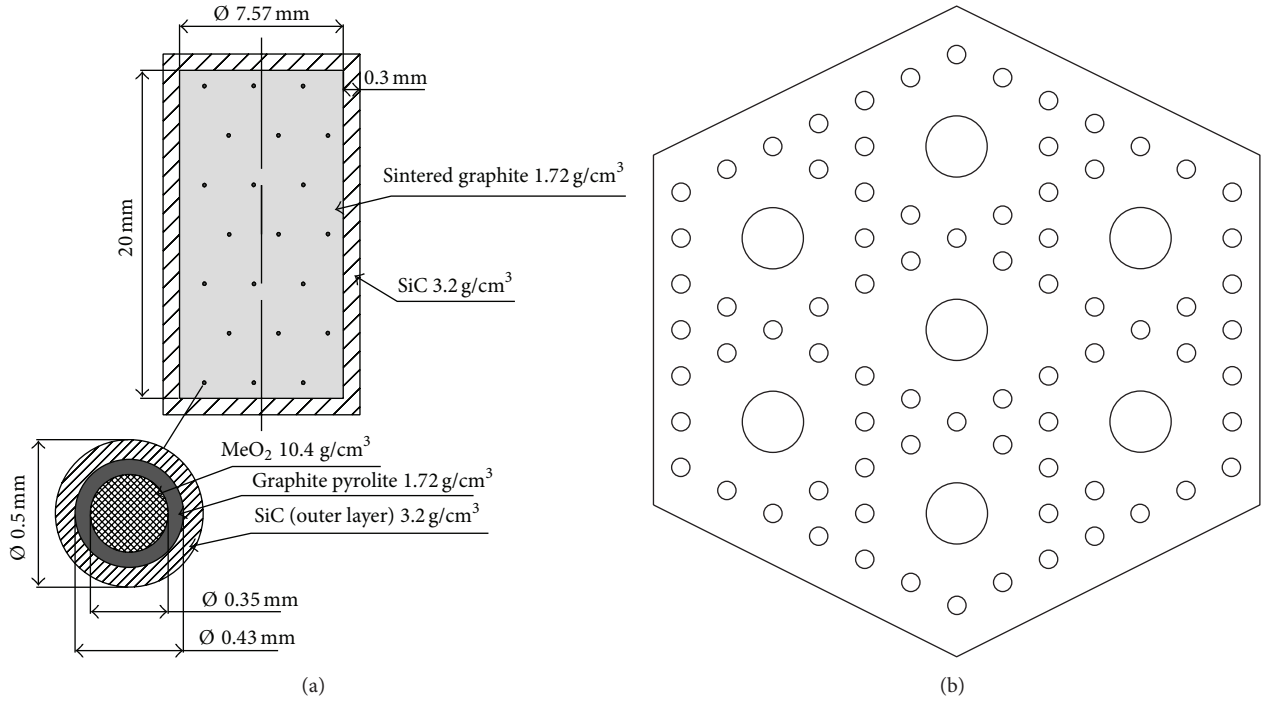


FIGURE 1: Calculation model of HTGTR fuel assembly: (a) 0500 and 1000 type fuel pellet of HTGTR; (b) HTGTR fuel assembly.

TABLE 1: Classification of FPs of HTGTR.

Fuel pellet type XXXX	Fuel volume (MeO ₂) (m ³)	Graphite volume (m ³)	SiC volume, (m ³)	Heavy metal mass (kg)
0500	$1.122 \cdot 10^{-8}$	$8.770 \cdot 10^{-7}$	$1.917 \cdot 10^{-7}$	$0.103 \cdot 10^{-3}$
1000	$2.245 \cdot 10^{-8}$	$8.539 \cdot 10^{-7}$	$2.036 \cdot 10^{-7}$	$0.206 \cdot 10^{-3}$
2000	$4.489 \cdot 10^{-8}$	$1.949 \cdot 10^{-6}$	$3.360 \cdot 10^{-7}$	$0.411 \cdot 10^{-3}$

describing complex geometrical objects, containing repeated elements with the help of grids, were used during the calculation model development.

Fuel pellet and fuel kernel: microfuel is a kernel from coated fissionable material dispersed into graphite matrix of cylindrical FPs, which are placed in the RC of HTGTR. Pu and Th-232 in equal proportions were used as fissionable material (heavy metal). Microfuel had bilayered coatings: layer 1: pyrolytic carbon (PyC) with the density of 1720 kg/m³; layer 2: silicon carbide (SiC) with the density of 3210 kg/m³. Configurations of the fuel kernel, coatings, and fuel pellets (see Figure 1) were chosen on the basis of scientific results obtained in [3, 4, 6, 11–16].

Preliminary estimates of energy production efficiency showed that bilayered coating decreases the fuel cost component considerably. Safety barrier is created by SiC coating on the fuel pellet surface.

Taking into account that coatings of microfuel are made from materials, in which cross sections do not have significant resonance peaks, the method of partial homogenization was used. In this approximation the fuel kernel coatings homogenize with the graphite matrix filling new volume with new concentrations. Acceptability of homogenization

was testified in the works of the authors in [5, 7, 17–21]. Homogenization of the fuel kernel is an impermissible approximation and it immediately causes noticeable deviation of k_{eff} (effective multiplication coefficient) (to 7-8%) from more precise simulation [5, 7, 20, 21] and experimental results [5, 19].

Three types of FPs of HTGTR were considered in the calculations. FPs of 0500 and 1000 type have the following constructional characteristics (see Figure 1(a)): diameter of $8.17 \cdot 10^{-3}$ m (with SiC surface layer); height of $2.06 \cdot 10^{-2}$ m (with SiC surface layer); volume of $1.08 \cdot 10^{-6}$ m³.

FPs of 2000 type have the following constructional characteristics: diameter of $1.2 \cdot 10^{-2}$ m (with SiC surface layer); height of $2.06 \cdot 10^{-2}$ m (with SiC surface layer); volume of $2.33 \cdot 10^{-6}$ m³. Close classification of the considered FPs is presented in Table 1.

Depending on the heavy metal composition in the FPs, the fuel assemblies of XXXXB and XXXXZ type were considered (see Figure 1(b)).

The fuel assembly of XXXXB type (of the first type) is Pu, 10%; Th-232, 90%. The fuel assembly of XXXXZ type (of the second type) is Pu, 50%; Th-232, 50%. The modifications of isotope composition of Pu in FPs are given in Table 2.

TABLE 2: Isotope composition of Pu in FPs of HTGTR.

Pu isotope composition modification	Pu-238 (%)	Pu-239 (%)	Pu-240 (%)	Pu-241 (%)	Pu-242 (%)
1	1.8	59	23	12.2	4
2	0	94	5	1	0

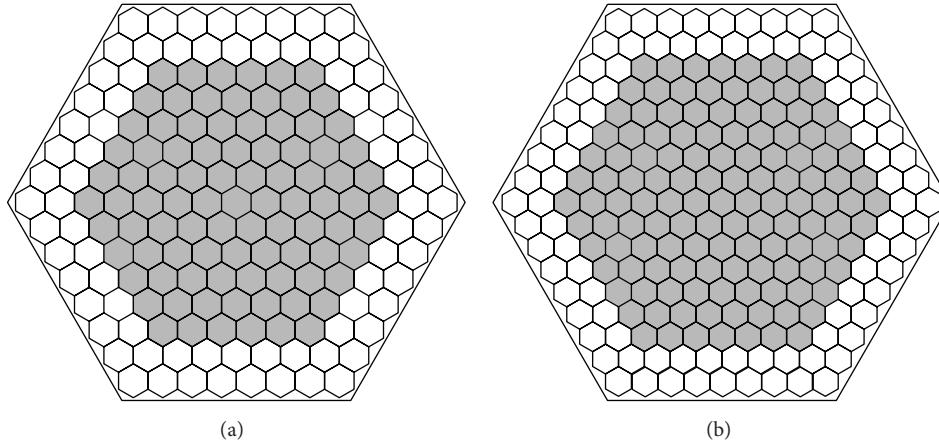


FIGURE 2: Calculation model of HTGTR reactor core: (a) small reactor core with the reflector; (b) large reactor core with the reflector.

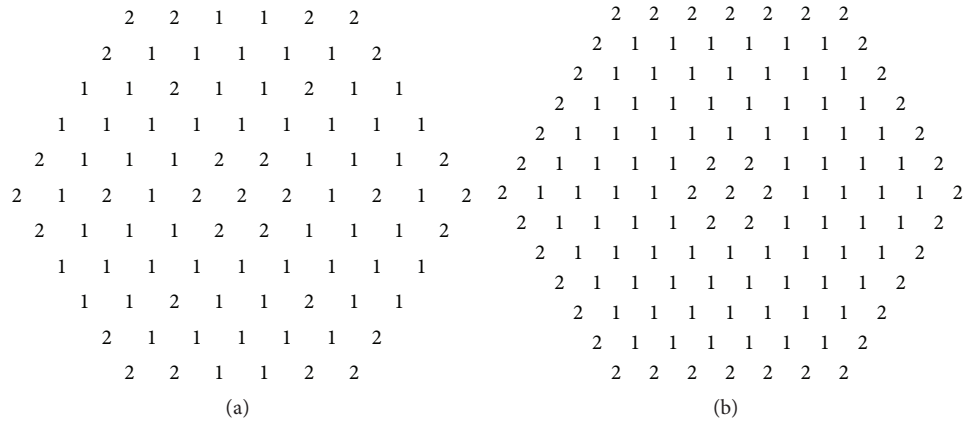


FIGURE 3: Arrangement schemes of fuel assemblies of the first and second type for small and large reactor cores: (a) small reactor core; (b) large reactor core.

Example. Fuel assembly 0500Z2 is a fuel assembly of the second type which consists of FPs of 0500 type (see Table 1) and has the second isotope composition of Pu (see Table 2). FP: fuel volume (MeO_2) is equal to $1.122 \cdot 10^{-8} \text{ m}^3$; graphite volume is $8.770 \cdot 10^{-7} \text{ m}^3$; SiC volume equals $1.917 \cdot 10^{-7} \text{ m}^3$; heavy metal mass is $0.103 \cdot 10^{-3} \text{ kg}$. Percentage of heavy metal, %, is Pu, 50; Th-232, 50. Isotope composition of Pu (%) is 238, 0; 239, 94; 240, 5; 241, 1; 242, 0.

Fuel Assembly (Fuel Block of the Unified Construction). It is a hexagon graphite fuel block with the width across the flats of 0.2 m and height of 0.8 m; 78 holes with the diameter of $8.2 \cdot 10^{-3} \text{ m}$ for FPs of 0500 and/or 1000 type; 7 holes with the diameter of $2.4 \cdot 10^{-2} \text{ m}$ for passing gaseous coolant (helium) (see Figure 1(b)).

Reactor Core. Cores are loaded with specified fuel assemblies by two methods (see Figures 2 and 3):

- (1) Small reactor core consists of fuel assemblies with fuel-containing parts, each about 2.4 m long, surrounded by two graphite blocks without holes; at the top and the bottom the reactor core is covered by 0.3 m thick graphite.
- (2) Large reactor core consists of fuel assemblies with fuel-containing parts, each about 2.0 or 2.4 m long, surrounded by two rows of graphite blocks without holes; at the top and at the bottom the reactor core is surrounded by 0.3 m thick graphite.

TABLE 3: Calculation results of effective multiplication coefficient k_{eff} and reactivity margin of the calculated type of HTGTR.

Number	Reactor core height (m)	Reactor core type	Fuel pellets type	Isotope composition of Pu	k_{eff}	$\Delta k/k$ (%)
1	2	Large	1000	1	1.0591	5.57
2	2	Large	1000	2	1.2445	19.65
3	2	Large	500	1	0.9611	-4.06
4	2	Large	500	2	1.1243	11.06
5	2.4	Small	1000	1	1.0611	5.75
6	2.4	Small	1000	2	1.2471	19.81
7	2.4	Small	500	1	0.9785	-2.20
8	2.4	Small	500	2	1.1475	12.85
9	2.4	Large	1000	2	1.2665	21.49
10	2.4	Large	500	2	1.1612	13.76
11	2.4	Large	1000	1	1.0801	7.80
12	2.4	Large	500	1	0.9921	-1.52

4. Neutron-Physical Calculations of High-Temperature Gas-Cooled Thorium Reactor

Neutron-physical calculations were carried out using the calculation code of MCU created in Russian National Research Center “Kurchatov Institute.” MCU program is intended for precision simulation of the processes of neutrons and photons transfer by analogue and nonanalogue methods of Monte-Carlo on the basis of evaluated nuclear data in any reactor types, considering changes of reactor material isotope composition during the lifetime [17].

BURNUP module was used for calculating the reactor lifetime. The module is a part of the program MCU5 and is intended for calculating composition changes of the reactor fissile isotopes and absorbing materials during its lifetime. The module provides possibility of calculation prediction of reactor materials nuclide composition and multiplying properties of the reactor depending on the fuel burn-up during its operation. Calculation of isotope composition changes during the reactor lifetime was performed at the given dependence of medium power in the system on time.

Constant MCU5 package is based on nuclear data bank MCUDB50. Library ACE/MCU being a part of MCUDB50 is point-to-point presented neutron-physical constants received from the files of evaluated nuclear data (ENDF/B-VII.0, JEFF-3.1.1, and JENDL-4.0) using the international program NJOY-99. Library BNAB/MCU (a part of MCUDB50) is an extended and modified version of 26-group constants system BNAB-78. Other sources included into nuclear data bank MCUDB50 are Russian (Russian National Library of Evaluated Neutron Data, Resonant Parameters Library, Moderators Generalized Phonon Spectrum Library, Library of Evaluated Neutron Data, etc.) and available international libraries (ENDSF, EXFOR).

Thus nuclear data bank MCUDB50 comprises constants obtained in group and point-to-point approximation, which allowed using in calculations statistic algorithms based on Monte-Carlo method and multigroup approximations using subgroup parameters in calculations of group coefficients in decomposed Boltzmann equation.

The schemes of fuel assemblies arrangement (of the first and second types) for small and large reactor cores of HTGTR are presented in Figure 3.

Results of k_{eff} calculation using MCU-5 for all considered calculation variants of HTGTR are presented in Table 3.

Calculation variants with the first isotope composition of Pu have the least values of k_{eff} from all variants; thus they were excluded from any further consideration.

Calculation variants 2, 6, and 9 of the high-temperature gas-cooled thorium reactor with fuel assemblies of 1000B2 and 1000Z2 type (see Table 3) are the reactor with small and large cores with fuel assemblies of the first and second types, fuel pellets of 1000 type having the second isotope composition of Pu (see Tables 1 and 2).

The distributions of neutron fluxes and power densities were obtained for the selected variants; irregularity coefficient estimation was carried out.

Irregularity coefficient of neutron flux distribution is ~ 1.5 for large reactor cores (calculation variants 2 and 9) and ~ 1.4 for small reactor core (calculation variant 6). Axial irregularity coefficient of power density for the reactor core with the height of 2 m (calculation variant 2) is ~ 1.25 , and for the reactor core with the height of 2.4 m (calculation variants 6 and 9) it is ~ 1.31 . Radial distribution irregularity coefficient does not exceed the value of ~ 3 .

For calculation modification 9, that is, for HTGTR large reactor core with fuel assemblies of 1000B2 and 1000Z2 type, the reactivity margin is 21.49%. When the reactor operates on the power of 60 MWt, the steady-state poisoning effect is $\sim 3.5\%$ and the reactivity loss rate is $\sim 0.123\%$ per day. It allows evaluating the reactor lifetime which is not more than 150 days.

In case of the small reactor core (calculation variant 2) the reactivity margin has a slightly smaller value ($\sim 20\%$), but due to significantly smaller sizes the reactivity loss rate is higher compared to the large reactor core; consequently, the reactor lifetime does not exceed 110 days.

The calculations showed that the modification, when the reactor core consists of fuel assemblies of the same type (e.g., 1000Z1 and 1000Z2 type) containing equal amount of Th-232 and Pu, is considered more perspective. Initial

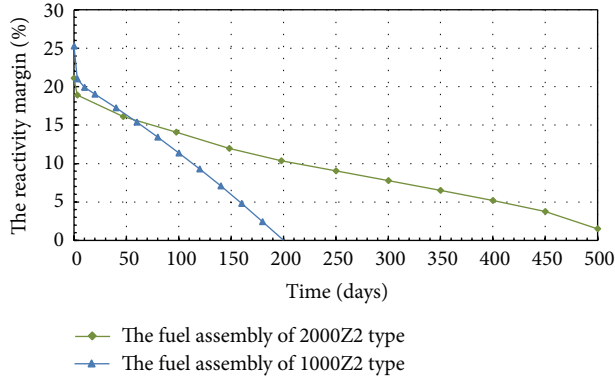


FIGURE 4: Change of the reactivity margin of HTGTR with fuel assemblies of 1000Z2 and 2000Z2 type.

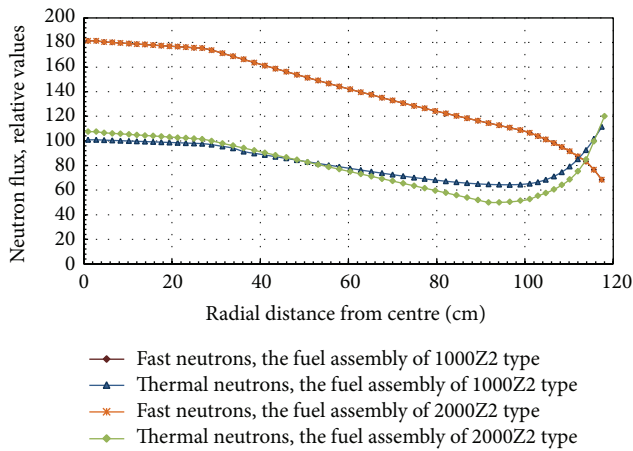


FIGURE 5: Radial flux density distribution of fast and thermal neutrons in the large core.

reactivity margin of HTGTR with fuel assemblies of 1000Z2 type increases up to 25.3%, and the reactor lifetime continues up to 210 days (see Figure 4).

Such reactor core loading allowed reducing power and neutrons flux distribution tilts in comparison with earlier calculation variants (see Figures 5 and 6). Approximately 1.7% of Th-232 burns up in the reactor with fuel assembly of 1000Z2 type; accumulation of U-233 is ~10% of this amount (considering the burn-up of the latter).

One more way of creating HTGTR was an attempt to increase fuel loading. Fuel of 2000 type was used (see Table 4).

Such fuel is used for arranging the biggest RC (with 381 fuel assemblies of 2000Z2 type) with the height of 2.4 m. The mass of plutonium in such RC increases by ~4 times, the initial reactivity margin of HTGTR being 21.1%, while the rate of reactivity loss decreases to 0.035% per day and lifetime increases to 510 effective days (see Figure 4).

Figures 5 and 6 show the distribution of power density and neutron flux in large reactor core with fuel assemblies of 2000Z2 type radially.

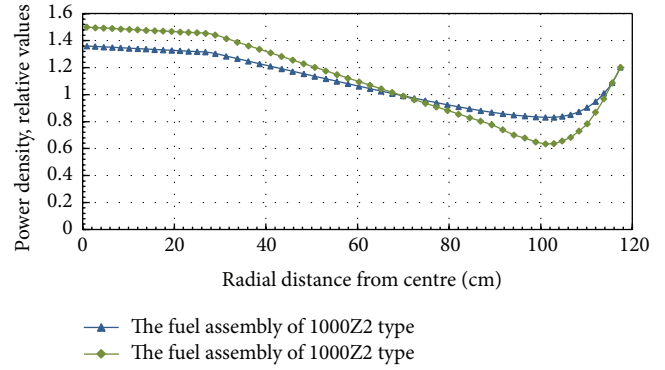


FIGURE 6: Radial power density distribution in the large core.

TABLE 4: Basic design parameters of the reactor.

Performance	Value
Full thermal reactor power (MWt)	60
Neutrons flux density:	
Thermal (n/cm ² /s)	$2.8 \cdot 10^{-13}$
Fast (n/cm ² /s)	$4.8 \cdot 10^{-13}$
Reactor geometrical parameters:	
Equivalent diameter of reactor core with reflector (m)	3.1
Height of reactor core with reflector (m)	3.0
Reactor core geometrical parameters:	
Reactor core equivalent diameter (m)	2.4
Reactor core height (m)	2.4
Fuel assembly type (fuel block of the unified design)	2000Z2
Number of fuel assemblies in the reactor core (pcs)	381
Fuel assembly geometrical parameters:	
Width across the flats (m)	0.2
Height (m)	0.8
Fuel pellets number (pcs)	3120
Heavy metal mass (kg)	1.282
Fuel pellet geometrical parameters:	
Height (m)	0.020
Diameter (m)	0.012
Heavy metal mass (kg)	$0.411 \cdot 10^{-3}$
Full starting core fuelling:	
Mass of Th (kg)	244
Mass of Pu (kg)	244
Maximum reactivity margin ($\Delta k/k$), %	21.3
Full-power reactor operation time (days)	510

5. Conclusion

Several optimum arrangements of the reactor cores (calculation variants 2, 6, and 9) intended for low-power industry and creation of mobile nuclear power installations with the capacity to 60 MWt were chosen from tens of HTGTR calculation variants.

Calculation variants 2, 6, and 9 of HTGTR with the fuel assemblies of 1000B2 and 1000Z2 type (see Table 3) are a reactor with small and large reactor cores with fuel assemblies of the first and second type and fuel pellets of 1000 type, which have the second isotopic composition of Pu (see Table 2).

The main disadvantage of these modifications of HTGTR is that Pu-239 does not manage to burn up and U-233 to accumulate to appreciable amount during short reactor lifetime (150 days for the large reactor core and 110 days for small reactor cores).

The calculations showed that the most perspective solution is when the reactor core consists of fuel assemblies of the same type and contains equal amount of Th-232 and Pu. In this case initial reactivity margin for the large reactor core loaded with fuel assemblies of 1000Z2 type increases up to 25.3% and the lifetime increases to 210 effective full power days (see Figure 4). During 210 days, 1.7% of Th-232 burns up in the reactor with fuel assembly of 1000Z2 type; accumulation of U-233 is ~10% of this amount (considering the burn-up of the latter). At such loading the distributions of flux density and power density become uniform over the whole reactor (see Figures 5 and 6).

One more way of creating HTGTR was an attempt to increase fuel loading. Fuel of 2000 type was used. Such fuel is used for arranging the biggest reactor core (with 381 fuel assemblies) with the height of 2.4 m. The mass of plutonium in such reactor core increases by ~4 times, the initial reactivity margin of HTGTR being 21.1%, while the rate of reactivity loss decreases to 0.035% per day and lifetime increases to 510 effective days (see Figure 4).

It should be noted that only the first stage of neutron-physical calculations researching the possibility of creating thorium reactor has been performed. In the calculation model of the reactor the control rods were not considered.

Conflict of Interests

The authors declare that there is no conflict of interests regarding the publication of this paper.

Acknowledgments

The research was performed at the support of Board for Grants of the President of the Russian Federation, competition for young scientists and postgraduate students for getting the presidential scholarship, Grant no. SP-295.2015.2. Experimental researches for verification of calculations were carried out at IRT-T at the financial support of the Ministry of Education and Science of the Russian Federation (works unique identifier RFMEFI59114X0001), Agreement no. 14.591.21.0001 of 15.08.2014.

References

- [1] E. F. Seleznev, *Fast Breeder Reactor Kinetics*, Nauka, Moscow, Russia, 2013, (Russian).
- [2] A. I. Kiryushin, N. N. Ponomarev-Stepnoi, and E. S. Glushkov, "Project of the GM-MHR high-temperature helium reactor with gas turbine," *Nuclear Engineering and Design*, vol. 173, pp. 119–129, 1997.
- [3] H. Nabelek, W. Kühnlein, W. Schenk, W. Heit, A. Christ, and H. Ragoss, "Development of advanced HTR fuel elements," *Nuclear Engineering and Design*, vol. 121, no. 2, pp. 199–210, 1990.
- [4] N. N. Ponomarev-Stepnoi, N. G. Abrosimov, A. V. Vasyaev et al., "Similarity of high-temperature gas-cooled reactor technologies and designs in Russia and USA," *Atomic Energy*, vol. 108, no. 2, pp. 89–96, 2010 (Russian).
- [5] N. G. Kodochigov, J. P. Suharev, E. V. Marova et al., "Analytical and experimental study of the GT-MGR core neutronic characteristics," *Atomic Energy*, vol. 102, no. 1, pp. 63–68, 2007 (Russian).
- [6] M. Fu, T. Liang, Y. Tang, X. U. Zhichang, and C. Tang, "Preparation of UO₂ kernel for HTR-10 fuel element," *Journal of Nuclear Science and Technology*, vol. 41, no. 9, pp. 943–948, 2004.
- [7] V. Şeker and Ü. Çolak, "HTR-10 full core first criticality analysis with MCNP," *Nuclear Engineering and Design*, vol. 222, no. 2-3, pp. 263–270, 2003.
- [8] M. Miletić, R. Fukač, I. Pioro, and A. Dragunov, "Development of gas cooled reactors and experimental setup of high temperature helium loop for in-pile operation," *Nuclear Engineering and Design*, vol. 276, pp. 87–97, 2014.
- [9] R. Stainsby, K. Peers, C. Mitchell, C. Poette, K. Mikityuk, and J. Somers, "Gas cooled fast reactor research in Europe," *Nuclear Engineering and Design*, vol. 241, no. 9, pp. 3481–3489, 2011.
- [10] W. J. Lee, Y. W. Kim, and J. Chang, "Perspectives of nuclear heat and hydrogen," *Nuclear Engineering and Technology*, vol. 41, no. 4, pp. 412–426, 2009.
- [11] I. V. Shamanin, A. A. Ukhov, H. J. Rutten, K. A. Haas, and W. Sherer, *The Use of (Th,U,Pu)O₂ Fuel in a Water Water Energy Reactor: Physics and Fuel Cycle Simulation by Means of the V.S.O.P. (97) Computer Code*, Forschungszentrum Juelich GmbH, Institute for Safety Research and Reactor Technology, Jülich, Germany, 1999.
- [12] I. Shamanin, S. Bedenko, and I. Gubaydulín, "Advantages of thorium nuclear fuel for thermal-neutron reactor," *Advanced Materials Research*, vol. 1084, pp. 275–279, 2015.
- [13] A. Talamo and W. Gudowski, "Performance of the gas turbine-modular helium reactor fuelled with different types of fertile TRISO particles," *Annals of Nuclear Energy*, vol. 32, no. 16, pp. 1719–1749, 2005.
- [14] H.-J. Allelein, M. J. Kania, H. Nabelek, and K. Verfondern, "Thorium fuel performance assessment in HTRs," *Nuclear Engineering and Design*, vol. 271, pp. 166–170, 2014.
- [15] C. Tang, B. Liu, Z. Li, Y. Quan, H. Zhao, and Y. Shao, "SiC performance of coated fuel particles under high-temperature atmosphere of air," *Nuclear Engineering and Design*, vol. 271, pp. 64–67, 2014.
- [16] M. J. Kania, H. Nabelek, K. Verfondern, and H.-J. Allelein, "Testing of HTR UO₂ TRISO fuels in AVR and in material test reactors," *Journal of Nuclear Materials*, vol. 441, no. 1–3, pp. 545–562, 2013.
- [17] D. S. Oleynik, D. A. Shkarovskiy, E. A. Gomin et al., "The status of MCU-5," *Physics of Atomic Nuclei*, vol. 75, no. 14, pp. 1634–1646, 2012.
- [18] R. Kelly and D. Ilas, "Verification of a depletion method in SCALE for the Advanced High-Temperature Reactor," *Nuclear Technology*, vol. 183, no. 3, pp. 391–397, 2013.
- [19] V. P. Garin, A. E. Glushkov, E. S. Glushkov et al., "Evaluated benchmark experiments in critical assemblies modeling HTGR

peculiarities at the Astra facility,” *Questions of Atomic Science and Technics. Physics of Nuclear Reactors*, vol. 2, pp. 75–96, 2009 (Russian).

- [20] B. K. Chukbar, “Verification of statistical method CORN for modeling of microfuel in case of high grain concentration,” *Questions of Atomic Science and Technics. Physics of Nuclear Reactors*, no. 1-2, pp. 15–21, 2014 (Russian).
- [21] R. Plukiene and D. Ridikas, “Modelling of HTRs with Monte Carlo: from a homogeneous to an exact heterogeneous core with microparticles,” *Annals of Nuclear Energy*, vol. 30, no. 15, pp. 1573–1585, 2003.

Research Article

Fabrication of UO_2 Porous Pellets on a Scale of 30 kg-U/Batch at the PRIDE Facility

Sang-Chae Jeon, Jae-Won Lee, Ju-Ho Lee, Sang-Jun Kang, Kwang-Yun Lee, Yung-Zun Cho, Do-Hee Ahn, and Kee-Chan Song

Korea Atomic Energy Research Institute, Daedeok-daero 989-111, Yuseong-gu, Daejeon 305-353, Republic of Korea

Correspondence should be addressed to Sang-Chae Jeon; scjeon@kaeri.re.kr

Received 1 July 2015; Accepted 11 August 2015

Academic Editor: Kisor K. Sahu

Copyright © 2015 Sang-Chae Jeon et al. This is an open access article distributed under the Creative Commons Attribution License, which permits unrestricted use, distribution, and reproduction in any medium, provided the original work is properly cited.

In the pyroprocess integrated inactive demonstration (PRIDE) facility at the Korea Atomic Energy Research Institute (KAERI), UO_2 porous pellets were fabricated as a feed material for electrolytic reduction on an engineering scale of 30 kg-U/batch. To increase the batch size, we designed and modified the corresponding equipment for unit processes based on ceramic processing. In the course of pellet fabrication, the correlation between the green density and sintered density was investigated within a compaction pressure range of 106–206 MPa, in terms of the optimization of processing parameters. Analysis of the microstructures of the produced UO_2 porous pellets suggested that the pellets were suitable for feed material in the subsequent electrolytic reduction process in pyroprocessing. This research puts forth modifications to the process and equipment to allow the safe mass production of UO_2 porous pellets; we believe these results will have immense practical interest.

1. Introduction

Nuclear reprocessing is the process of chemically treating spent nuclear fuel to recover plutonium (Pu) and uranium (U). The aqueous process, PUREX, has conventionally been used for this purpose. However, pyroprocessing has recently emerged as one of the key technologies that can reduce nuclear waste while improving the efficiency of resource use in the nuclear fuel cycle. This is because, among other advantages over PUREX, pyroprocessing is less proliferative as it does not enable the separation of Pu from other impurities [1]. Pyroprocessing is a process that starts with the head-end process, followed by electrolytic reduction, electrorefining, electrowinning, and salt purification [1–3].

The head-end process includes chopping, mechanical or oxidative decladding, and high-temperature voloxidation as unit processes. During the head-end process, uranium and transuranic (TRU) elements are recovered from spent fuel, while fission products such as Kr, Xe, H-3, C-14, Cs, and I are removed [4–6]. Another important goal of the head-end process is the fabrication of a proper feed material for the subsequent electrolytic reduction process. The feed material can take on different physical forms depending on

the decladding method used: mechanical decladding results in crushed particles, whereas oxidative decladding results in porous pellets or granules. Compared to mechanical decladding, oxidative decladding results in a high recovery rate of the fuel material from rod-cuts [3]. However, during the oxidative decladding process, uranium oxide undergoes a change in phase from a UO_2 pellet to a U_3O_8 powder. In this viewpoint, the UO_2 porous pellet form, which can be prepared from the U_3O_8 powder via ceramic processing, has attracted much interest as a promising feed form for the following electrolytic reduction [6–9].

The fabrication of a UO_2 porous pellet involves pelletizing and sintering of U_3O_8 pellets at high temperature under a H_2 -containing atmosphere [6]. In this regard, there have been many studies that have investigated the reduction behaviors and microstructural variations of U_3O_8 under reducing atmosphere [10–15]. However, the majority of such investigations have been carried out on a lab scale. Therefore, in order to achieve engineering-scale production (50 kg-U/batch), for example, at the PRIDE facility [9], it is necessary to determine if the fabrication process and the corresponding equipment need to be modified to suit mass production.

TABLE 1: Fabrication process of UO_2 porous pellets and its chemical/physical form during the various stages.

Process	Starting material	Oxidation	Mixing	Pelletizing	Sintering
Chemical/ physical Form	UO_2 / dense pellet	U_3O_8 / powder	$\text{U}_3\text{O}_8 + \text{EBS}^a$ / powder	$\text{U}_3\text{O}_8 + \text{EBS}^a$ / pellet	UO_2 / porous pellet

^aEthylene bis stearamide, $(\text{CH}_2\text{NHC}(\text{O})\text{C}_{19}\text{H}_{35})_2$.

In the present experiment, based on the literature and conventional ceramic processing, a fabrication process was adapted to meet the needs of the fabrication scale in PRIDE facility: oxidation, mixing, pelletizing, and sintering. Towards this end, the fabrication equipment was newly designed and improved by introducing new structures. In addition, the relationship between the green density and sintered density under compaction pressure was investigated in the course of mass production. From a practical aspect, the results of this investigation can be employed to the mass production of UO_2 porous pellets, which can be used as a feed material for the subsequent electrolytic reduction process.

2. Materials and Methods

2.1. Fabrication of Porous Pellets. Similar to conventional ceramic processing, the fabrication of UO_2 porous pellets in the PRIDE facility involves four sequential processes: oxidation, mixing, pelletizing, and sintering. The fabrication process of the porous pellets and the chemical/physical form of the produced uranium oxides after each process are summarized in Table 1. Considering the purpose of the PRIDE facility, the fabrication equipment was designed to accommodate a capacity of 50 kg-U/batch; a schematic drawing of this equipment is shown in Figure 1. The porous UO_2 pellets were fabricated in the PRIDE facility as follows: UO_2 pellets with a diameter of 8.05 mm, a height of 10.08 mm, and a weight of 5.20 g were prepared as the starting material. The geometrical density of UO_2 pellets was about 92.47% on average, much higher than the theoretical density of UO_2 , 10.96 g/cm³. The UO_2 pellets were oxidized to U_3O_8 powder at 480°C for 16 h under a 75% O_2 -Ar atmosphere in a rotating drum furnace, which was equipped with a double chamber: an inner chamber made of INCONEL 600 and an outer chamber of SUS 304 stainless steel. A schematic drawing and a photograph of the rotating drum furnace are shown in Figure 1(a). On the inside wall of the inner chamber, a spiral screw structure is formed to allow transport of the UO_2 feed pellets and/or produced U_3O_8 powders back and forth by rotating the chambers. After complete oxidation of the UO_2 pellets, the oxidized U_3O_8 powder was recovered by reverse rotation of the chambers. The recovered U_3O_8 powder was mixed with 2 wt% of acrawax (ethylene bis stearamide (EBS), $\text{C}_{38}\text{H}_{76}\text{O}_2\text{N}_2$, CAS #: 110-30-5) by using a tubular mixer for 30 min. Acrawax is a well-known lubricant used to minimize die wall friction during the subsequent pelletizing process. The powder mixture containing EBS was then pressed into a pellet shape using the rotary press machine shown in

Figure 1(b). A schematic drawing of the driving part of the rotary press shows 13 sets of die and punches (Figure 1(b)). In a single rotation cycle, U_3O_8 powder is injected into the hole of the die, followed by compaction of the filled powder in the die by the upper and lower punches and ejection of the pelletized U_3O_8 ; this cycle can be repeated continuously. The hole of the die used in this experiment was designed to be 6.6 mm wide, and the rotation speed of the rotary press was optimized to be 5 rpm during the pelletizing process. The green pellets obtained after pressing were sintered and reduced in a vertical-type sintering furnace that helped to minimize the temperature gradient throughout the heating zone. The heating elements penetrating the ceiling surface of the furnace chamber allow the samples to be completely surrounded by the heating element. The green pellets were put into five zirconia crucibles, which can contain ~13 kg of U_3O_8 pellets, and then sintered at 1350°C for 12 h under 4% H_2 -Ar atmosphere.

2.2. Characterization of Porous Pellets. The microstructures of the U_3O_8 powders and UO_2 pellets were observed by scanning electron microscopy (SEM, Philips XL-30, Netherlands) after polishing using diamond paste. The pore sizes and size distributions were measured from the SEM images using the image processing software, Matrox Inspector 2.1 (Matrox Inc. Canada). The crystal structure of the fabricated UO_2 pellets was examined using X-Ray Diffraction (XRD, Rigaku Mini-Flex, Japan). The XRD experiments were performed over the 2θ range of 20–80° and at a scan speed of 6°/min and a step size of 0.01°. The pellets were crushed into powder form in an agate mortar and pestle prior to the measurements.

3. Results and Discussion

Figure 2 shows the variations in the temperature and O_2 concentration during the oxidation process of UO_2 to U_3O_8 in a rotating drum furnace (Figure 2(a)) and macro/microscopic images of the resultant oxidized U_3O_8 powder (Figure 2(b)). The oxidation temperature was determined based on a previous report on the oxidation of UO_2 to U_3O_8 [16]. This was done taking into account the temperature difference measured during the preliminary test between the two different positions of the rotating drum furnace: temperature of heating element (T_{he}) and inside chamber (T_{inside}). Through the heat treatment at 470–480°C for 16 h, fine U_3O_8 powders were produced without significant agglomerates, as shown in Figure 2(b), indicating homogeneous oxidation of UO_2 into U_3O_8 .

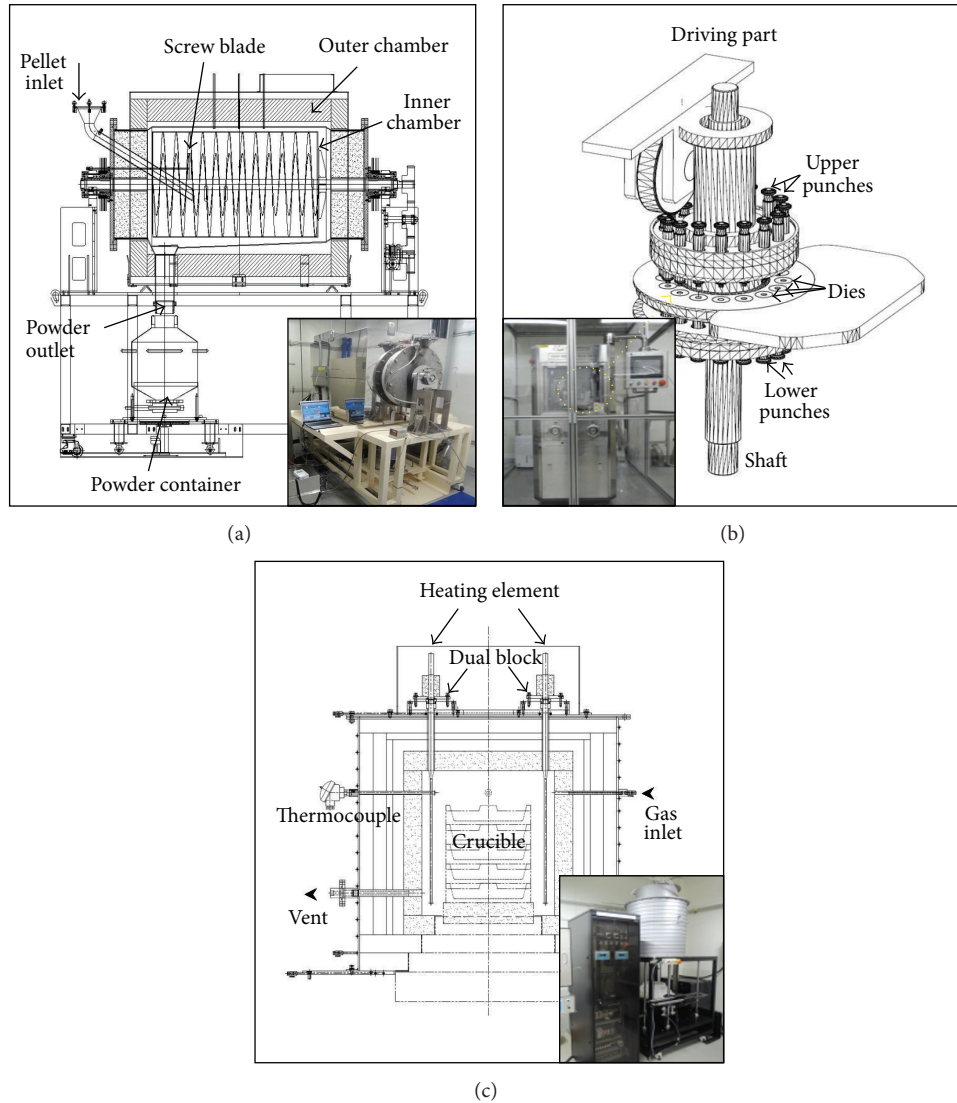


FIGURE 1: Schematic drawings and photographs of (a) rotating drum furnace, (b) driving part of rotary press, and (c) sintering furnace constructed in PRIDE.

During the oxidation, the phase change is accompanied by volumetric expansion ($\sim 23.6\%$) due to the difference in density between the two phases: 10.96 g/cm^3 for UO_2 and 8.37 g/cm^3 for U_3O_8 [13]. The U_3O_8 powder particles, therefore, become popcorn shaped. In our experiment as well, the U_3O_8 powder particles were popcorn shaped, with an average particle size of $4.63 \mu\text{m}$, as shown in Figure 2(b) [17, 18]. Both fine particle size and uniform phase of the produced U_3O_8 powder are conditions necessary for securing good compactibility during the following pelletizing process. Before the pelletizing process, $0.2 \text{ wt}\%$ of acrawax was added to the U_3O_8 powders. Acrawax is a well-known lubricant material in powder metallurgy, and it reduces the friction between the die and the wall while improving the mechanical strength of the green pellet [19]. After addition of the acrawax, the powders were mixed using a tubular mixer for 30 min to improve the uniformity of the powders.

The mixed U_3O_8 powders were then compacted into pellets using a rotary press, as shown in Figure 2(b). The rotary press exhibited excellent production yield: 3,500 pellets per hour (7 kg-U/h). The rough shape of the U_3O_8 powder indicates that it has poor flowability, which leads to the failure of uniform die filling during the pelletizing process. To improve the flowability, in this experiment, a mechanical feeder was installed. Figure 3(a) shows a schematic of the mechanical feeder attached at the feeding part of the rotary press. It consists of three impellers and a powder scraper, which allow a constant amount of U_3O_8 powders to be filled in the rotating dies. With the rotary press machine, around 30 kg of U_3O_8 powders were compressed into green pellets, as shown in Figure 3(b).

With an aim of optimizing the processing parameters in the pelletizing experiment, the effect of compaction pressure on the density of green pellets was examined. The compaction

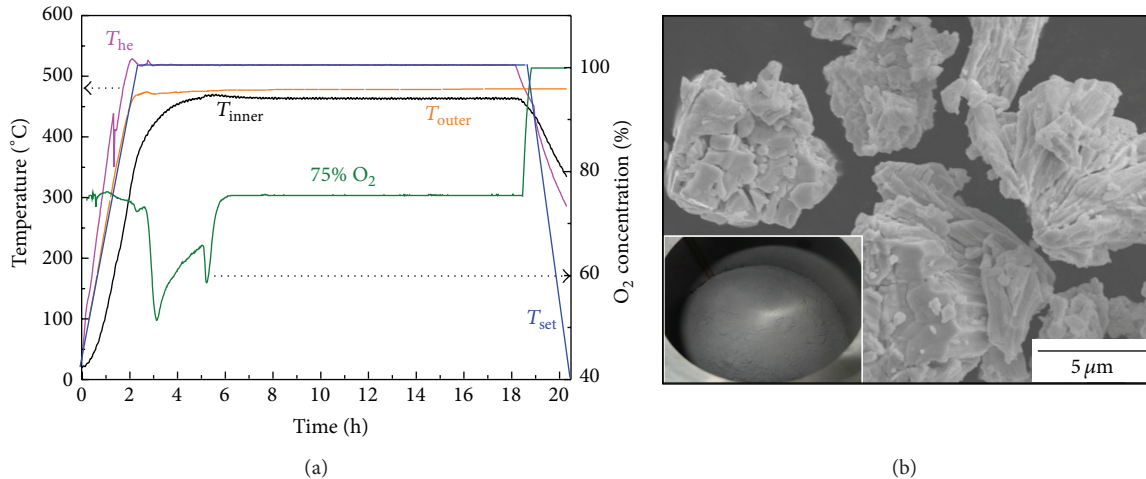


FIGURE 2: Experimental conditions and results of oxidation process: (a) variations in temperature and O₂ concentration and (b) produced U₃O₈ powder.



FIGURE 3: Modification of the equipment and results of pelletizing process: (a) schematic drawings and a photograph of the mechanical feeder attached to rotary press and (b) produced U₃O₈ green pellets.

pressure could be controlled by regulating the amount of U₃O₈ powder filled into die hole and the pressing depth of upper punch. In this case, the compaction pressure ranged from approximately 100 to 200 MPa. The density of pellets increased linearly with the compaction pressure in the range of 60.33 to 68.14% TD, as listed in Table 2. The geometrical information and green density values for pelletization under different pressures are also summarized in Table 2. The pellets have similar size and weight, with little standard deviation in the values, thus indicating that a uniform amount of powders was filled and uniform force was applied during the pelletizing process using a rotary press machine. Figure 4 shows photographs of the green pellets pressed under different compaction pressure values. It is evident that the surface of the pellets becomes smoother with increasing compaction pressure.

To ensure that the U₃O₈ green pellets are suitable as feed for electrolytic reduction, they must be sintered and reduced

to UO₂ phase by heat treatment in the furnace. As shown in Figure 1(c), a vertical-type furnace was constructed for heat treatment of the green pellets (50 kg/batch). A vertical-type furnace was used in order to minimize the temperature gradient throughout the heating zone. The sample loaded at the center of the furnace was surrounded by the heating element. To secure mechanical stability up to high temperatures, the green pellets were placed in zirconia crucible that was 320 mm in diameter and 10 mm thick. Each crucible contained ~13 kg of U₃O₈ pellets and could be stacked tightly on another crucible.

Figure 5 shows the programmed and measured temperature variations during sintering of the U₃O₈ green pellets. The sintering was conducted at 1350°C for 12 h under a reducing atmosphere using a gas containing hydrogen (4% H₂-Ar balanced). The thermal history includes dewaxing treatment at 700°C for 1 h to remove the added acrawax. The retarded heating and cooling rate could be attributed to

TABLE 2: Green and sintered density and % TD (theoretical density) of pellets under different compaction pressures.

Compaction pressure (MPa)	Pellet height (mm)	Pellet weight (g)	Green density (g/cm ³)	% TD ^a (%)
106 {33}	6.78 {0.03}	1.17 {0.03}	5.05 {0.13}	60.33 {1.51}
160 {43}	6.34 {0.03}	1.19 {0.03}	5.50 {0.14}	65.73 {1.63}
206 {52}	6.02 {0.06}	1.17 {0.03}	5.70 {0.11}	68.14 {1.37}

^aTheoretical density compared to U₃O₈ (8.37 g/cm³).

{ } Standard deviation.

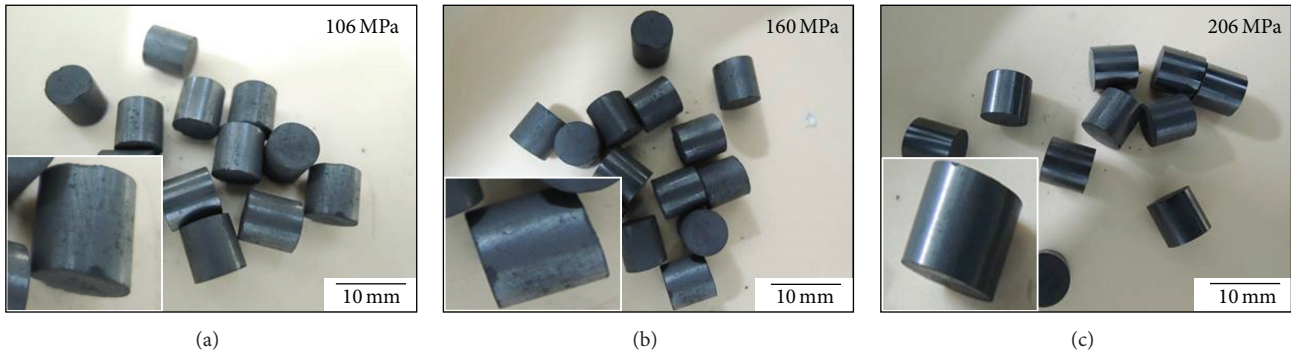


FIGURE 4: Green pellets pressed under different pressures: (a) 106, (b) 160, and (c) 206 MPa.

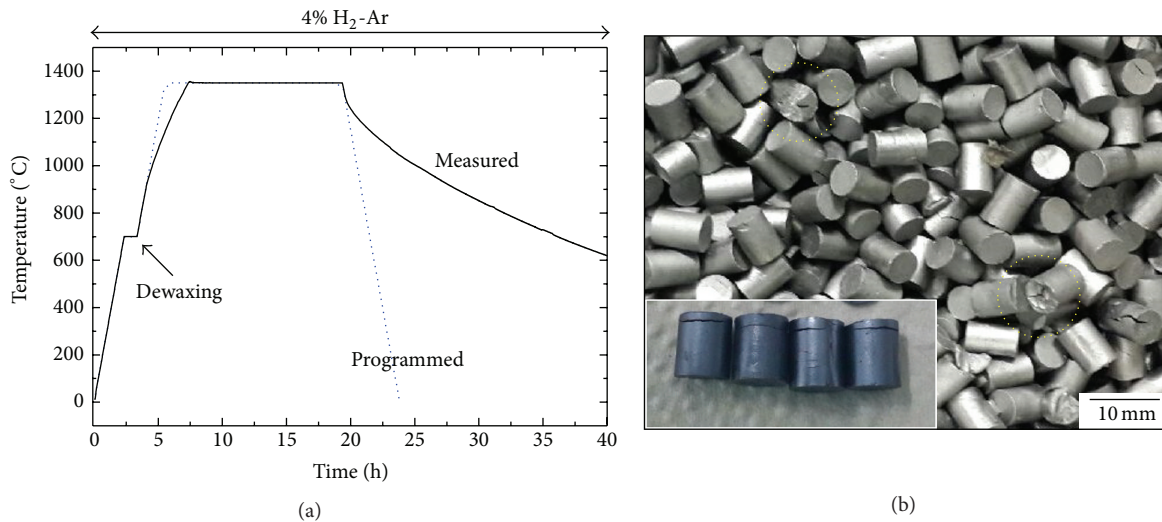


FIGURE 5: Experimental conditions and results of oxidation process: (a) thermal profile of sintering process and (b) produced UO₂ sintered pellets. The inset in (b) and dashed circles indicate delamination defects.

the thick refractory ceramics coated inside the heating zone. Figure 5(b) shows the sintered UO₂ pellets with a scale of 30 kg-U/batch. Among the produced pellets, delamination cracks are observed at the end of some pellets, as shown in the inset photograph. The dashed circles in Figure 5(b) show the pellets that were crushed owing to the delamination cracks. The delamination crack is known to result from severe friction between the die and the wall during the pelletizing process [20]. When cracks are formed in the pellets, dust particles (<45 μm), which escape the cathode basket and

infiltrate into the molten salt in the electrolytic reduction process, can be formed. The crack formation can be avoided by further optimizing the processing conditions, such as the amount of acrawax, mixing time, and compaction pressure.

Figure 6 shows the XRD patterns of the sintered pellets extracted from different crucibles: top and bottom floor. All patterns are similar to that of the UO₂ phase, without any second phase. This indicates that all of the sintered pellets have the UO₂ phase, irrespective of their position in the furnace during the sintering. It also implies that the reduction

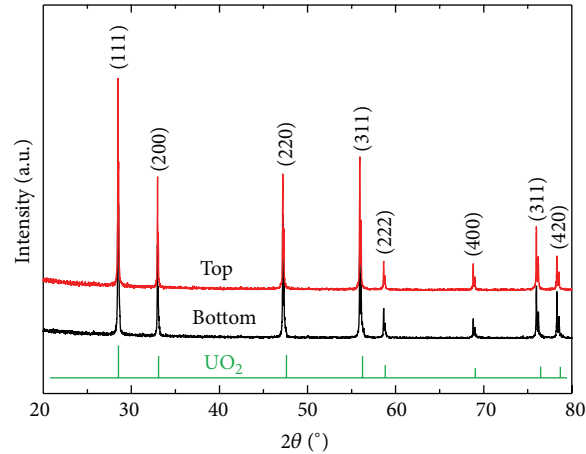


FIGURE 6: XRD patterns of sintered pellets extracted from the bottom and top crucibles.

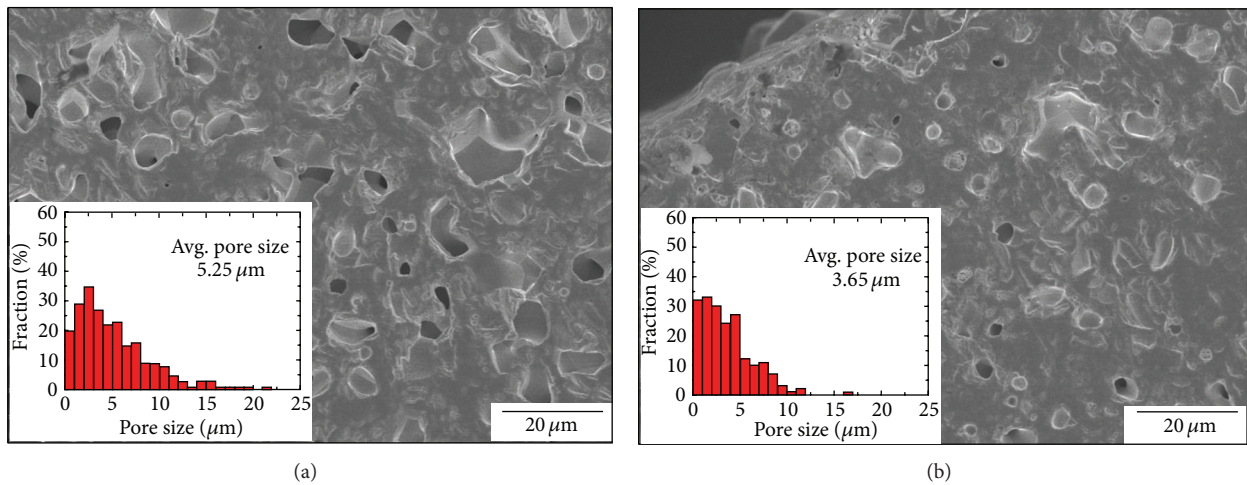


FIGURE 7: SEM micrographs and measured pore size distributions of sintered pellet: (a) inside and (b) surface.

of U_3O_8 to UO_2 was completed during the previous sintering process.

Figure 7 shows SEM micrographs of different positions in a pellet: inside and surface. The pore structures at the center/surface of the porous pellet were clearly observed after mechanical polishing but with no etching. Except a slight difference in the size of the pores and their connectivity, both from the inside and from the surface, a porous microstructure with interconnected micropores is clearly seen in the SEM micrographs. Compared to the pores on the surface, the pores inside the pellets were larger and more interconnected. The average pore size inside and on the surface of the pellets was 5.25 and 3.65 μm , respectively. This could be attributed to the preceding densification of the surface region, resulting in the escape of gas trapped in the pores deep inside the pellet.

Figure 8 shows the relationship between the green density of the U_3O_8 pellets and the sintered density of the UO_2 pellets with respect to the compaction pressure. In the following

electrolytic reduction process, the density of a porous pellet is one of the major factors determining the reduction efficiency [20]. Generally, the sintered density of UO_2 pellets strongly depends on the green density of U_3O_8 pellets, which is determined by the compaction pressure in the pelletizing process. Therefore, to fabricate porous UO_2 sintered pellets within a suitable density range, the relationship between the compaction pressure, green density of U_3O_8 pellets, and sintered density of UO_2 pellets should be clarified. In this experiment, the following linear relationship was obtained in the compaction pressure range from 106 to 206 MPa:

$$SD (\%) = 0.35GD (\%) + 39.87 (\%), \quad (1)$$

where SD and GD are the percentages of sintered density and green density, respectively. This provides technical data for the fabrication of UO_2 porous pellets in large batches and can help in ensuring the quality assurance and quality control (QA/QC) of the porous pellets.

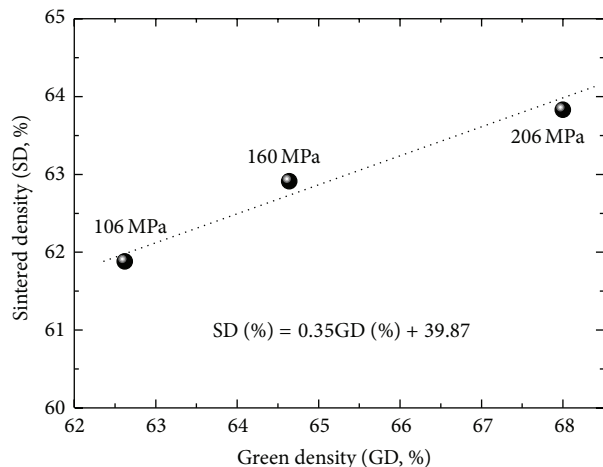


FIGURE 8: Relationship between green density (GD) and sintered density (SD) with compaction pressure.

4. Conclusions

UO₂ porous pellets, which are promising as a feed material for the electrolytic reduction process in pyroprocessing, were fabricated in the PRIDE facility at an engineering scale. The fabrication processing was based on conventional ceramic processing, which consists of oxidizing, pelletizing, and sintering. To meet the demand for scaling up, three kinds of fabrication equipment were constructed, and the drawbacks in scaling up were addressed at the stage of design and fabrication. A screw structure in the rotating drum furnace helps to convey a large amount of powders/pellets by rotating the chambers in the oxidation process, a mechanical feeder improves the flowability of the U₃O₈ powders into the hole of dies during the pelletizing process, and a vertically penetrating heating element structure reduces the temperature gradient throughout the large space during the sintering process. In addition, this paper clarifies the relationship between green density, sintered density, and the compaction pressure in terms of the optimization of processing parameters as a practical aspect of the fabrication of UO₂ porous pellets.

Conflict of Interests

The authors declare that they have no conflict of interests regarding the publication of this paper.

Acknowledgment

This work was supported by the National Research Foundation of Korea (NRF) grant funded by the Korea government (MEST) (no. 2012M2A8A5025696).

References

[1] K.-C. Song, H. Lee, J.-M. Hur, J.-G. Kim, D.-H. Ahn, and Y.-Z. Cho, "Status of pyroprocessing technology development in

Korea," *Nuclear Engineering and Technology*, vol. 42, no. 2, pp. 131–144, 2010.

- [2] J.-H. Yoo, C.-S. Seo, E.-H. Kim, and H.-S. Lee, "A conceptual study of pyroprocessing for recovering actinides from spent oxide fuels," *Nuclear Engineering and Technology*, vol. 40, no. 7, pp. 581–592, 2008.
- [3] H. Lee, G.-I. Park, K.-H. Kang et al., "Pyroprocessing technology development at KAERI," *Nuclear Engineering and Technology*, vol. 43, no. 4, pp. 317–328, 2011.
- [4] J. G. Asquith and L. F. Grantham, "A low-decontamination approach to a proliferation-resistant fuel cycle," *Nuclear Technology*, vol. 41, no. 2, pp. 137–148, 1978.
- [5] J. Y. Colle, J.-P. Hiernaut, D. Papaioannou, C. Ronchi, and A. Sasahara, "Fission product release in high-burn-up UO₂ oxidized to U₃O₈," *Journal of Nuclear Materials*, vol. 348, no. 3, pp. 229–242, 2006.
- [6] Y. Sakamura and T. Omori, "Electrolytic reduction and electrorefining of uranium to develop pyrochemical reprocessing of oxide fuels," *Nuclear Technology*, vol. 171, no. 3, pp. 266–275, 2010.
- [7] E.-Y. Choi, J.-M. Hur, I.-K. Choi et al., "Electrochemical reduction of porous 17 kg uranium oxide pellets by selection of an optimal cathode/anode surface area ratio," *Journal of Nuclear Materials*, vol. 418, no. 1–3, pp. 87–92, 2011.
- [8] H.-S. Lee, G.-I. Park, J.-W. Lee et al., "Current status of pyroprocessing development at KAERI," *Science and Technology of Nuclear Installations*, vol. 2013, Article ID 343492, 11 pages, 2013.
- [9] S.-C. Jeon, J.-W. Lee, S.-J. Kang et al., "Temperature dependences of the reduction kinetics and densification behavior of U₃O₈ pellets in Ar atmosphere," *Ceramics International*, vol. 41, no. 1, pp. 657–662, 2014.
- [10] H. Chevrel, P. Dehaut, B. Francois, and J. F. Baumard, "Influence of surface phenomena during sintering of overstoichiometric uranium dioxide UO_{2+x}," *Journal of Nuclear Materials*, vol. 189, no. 2, pp. 175–182, 1992.
- [11] M. Pijolat, C. Brun, F. Valdivieso, and M. Soustelle, "Reduction of uranium oxide U₃O₈ to UO₂ by hydrogen," *Solid State Ionics*, vol. 101–103, no. 1, pp. 931–935, 1997.
- [12] C. Brun, F. Valdivieso, M. Pijolat, and M. Soustelle, "Reduction by hydrogen of U₃O₈ into UO₂: nucleation and growth, influence of hydration," *Physical Chemistry Chemical Physics*, vol. 1, no. 3, pp. 471–477, 1999.
- [13] K. W. Song, K. S. Kim, and Y. H. Jung, "Densification behavior of U₃O₈ powder compacts by dilatometry," *Journal of Nuclear Materials*, vol. 279, no. 2–3, pp. 356–359, 2000.
- [14] F. Valdivieso, M. Pijolat, M. Soustelle, and J. Jourde, "Reduction of uranium oxide U₃O₈ into uranium dioxide UO₂ by ammonia," *Solid State Ionics*, vol. 141–142, pp. 117–122, 2001.
- [15] J. H. Yang, Y. W. Rhee, K. W. Kang, K. S. Kim, K. W. Song, and S. J. Lee, "Formation of columnar and equiaxed grains by the reduction of U₃O₈ pellets to UO_{2+x}," *Journal of Nuclear Materials*, vol. 360, no. 2, pp. 208–213, 2007.
- [16] F. Valdivieso, V. Francon, F. Byasson, M. Pijolat, A. Feugier, and V. Peres, "Oxidation behaviour of unirradiated sintered UO₂ pellets and powder at different oxygen partial pressures, above 350°C," *Journal of Nuclear Materials*, vol. 354, no. 1–3, pp. 85–93, 2006.
- [17] K. W. Song and M. S. Yang, "Formation of columnar U₃O₈ grains on the oxidation of UO₂ pellets in air at 900°C," *Journal of Nuclear Materials*, vol. 209, no. 3, pp. 270–273, 1994.

- [18] J. H. Yang, K. W. Kang, K. S. Kim, Y. W. Rhee, and K. W. Song, "Recycling process for sinter-active U_3O_8 powders," *Journal of Nuclear Science and Technology*, vol. 47, no. 6, pp. 538–541, 2010.
- [19] M. M. Baum, R. M. Becker, A. M. Lappas et al., "Lubricant pyrolysis during sintering of powder metallurgy compacts," *Metallurgical and Materials Transactions B*, vol. 35, no. 2, pp. 381–392, 2004.
- [20] J. S. Reed, *Principles of Ceramics Processing*, John Wiley & Sons, New York, NY, USA, 1996.

Research Article

Cyclic Stress Response and Fracture Behaviors of Alloy 617 Base Metal and Weld Joints under LCF Loading

Seon Jin Kim,¹ Rando Tungga Dewa,¹ Woo Gon Kim,² and Min Hwan Kim²

¹*Pukyong National University, 365 Shinsunro, Nam-gu, Busan 608-739, Republic of Korea*

²*Korea Atomic Energy Research Institute, 989-III Daedeokdaero, Yuseong-gu, Daejeon 305-353, Republic of Korea*

Correspondence should be addressed to Seon Jin Kim; sjkim@pknu.ac.kr

Received 4 June 2015; Accepted 31 August 2015

Academic Editor: Kaushik Das

Copyright © 2015 Seon Jin Kim et al. This is an open access article distributed under the Creative Commons Attribution License, which permits unrestricted use, distribution, and reproduction in any medium, provided the original work is properly cited.

Cyclic stress response and fracture behaviors of Alloy 617 base metal (BM) and Alloy 617 weld joints (WJ) are investigated under strain controlled low cycle fatigue (LCF) loading. Axial fully reversed total-strain controlled tests have been conducted at room temperature with total strain ranges of 0.6, 0.9, 1.2, and 1.5%. At the all testing conditions, weld joint specimens have shown higher peak stresses than the base metal specimens, whereas the plastic strain accumulation of the base metal specimens is comparatively higher than those of the weld joint specimens. The cyclic stress response behavior of both base metal and weld joint specimens revealed initial cyclic hardening during first small number of cycles followed by progressive softening to failure. Higher strain amplitudes decreased the fatigue lives for both base metal and weld joint specimens; subsequently weld joint specimens had lower fatigue resistances relative to base metal specimens. Furthermore, the cracking in weld joint specimens initiated in the weld metal (WM) region. The crack initiation and propagation showed transgranular mode for both base metal and weld joint specimens; especially weld joint specimens showed a wedge type crack initiation about 45 degrees to the loading direction because of the dendritic structure.

1. Introduction

The very high temperature gas-cooled reactor (VHTR) is currently the most promising reactor among the Generation-4 reactors for producing electricity and hydrogen economically. The VHTR structural components like the reactor internals, piping, hot gas ducts (HGD), and intermediate heat exchangers (IHX) are designed for a design life of 30–60 years at 950°C and 3–8 MPa in He impurities. The HGD and IHX are key components, and their materials have potential for use in nickel-based superalloys such as Alloy 617, Haynes 230, Hastelloy-X, and Alloy 800H. The Alloy 617 does have the distinction of possessing very high creep resistance at elevated temperatures when compared with other nickel based alloys. In addition to its high temperature strength, it also has excellent resistance to wide range of corrosive environments and is readily formed and welded by conventional techniques. For this reasons, Alloy 617 is considered as one of the leading candidates because of its highest allowable design stress compared to other superalloys

for construction of the IHX associated with the reformer system [1–4].

The LCF loadings are suspected to a result of power transients and temperature gradient induced thermal strain during operation as well as startups and shutdowns and also the fluctuated work load, each of which produces cyclic loading [2, 5]. LCF situation is characterized by high plastic strain in low frequency and the fatigue life is about $<10^4$ cycles. Although the low cycle fatigue behavior of Alloy 617 base metal has been studied by many researchers [5–9], less information is available on the welded joints [10]. Extensive high temperature low cycle fatigue studies of welded joints in Alloy 617 and austenitic stainless steels have shown markedly lower lives in weld areas [10, 11]. In mechanical structures, the welded components are unavoidable and some of the components were joined by various welding techniques. Moreover, the welded joints are more brittle than the base metal and may have several original defects [1]. In addition, the welded joints are microstructurally and mechanically heterogeneous, which could form one of the potential sites

TABLE 1: The chemical composition of Alloy 617 plate used in this study (wt.%).

		C	Ni	Fe	Si	Mn	Co	Cr	Ti	P	S	Mo	Al	B	Cu
ASTM	Min	0.05	Bal.	10.0	20.0	8.0	0.8
Spec.	Max	0.15	Bal.	3.0	0.5	0.5	15.0	24.0	0.6	0.015	0.015	10.0	1.5	0.006	0.5
	Alloy 617	0.08	53.11	0.949	0.084	0.029	12.3	22.2	0.4	0.003	<0.002	9.5	1.06	<0.002	0.0268

of the fatigue failure. The welded section material could be considerably affected by the welding process which is responsible for heterogeneities. Therefore, the fatigue damage evolution mechanisms such as fatigue crack initiation and crack propagation could be different and the evaluation of fatigue damage of welded joints must be confirmed [11].

Current research activities at Korea Atomic Energy Research Institute (KAERI) and Pukyong National University (PKNU) focus on the study of low cycle fatigue behavior of Alloy 617 base metal and the welded joint specimens were machined from GTAW butt-welded with temperature between passes under 177°C and the postheat-treatment was not conducted because the Ni-based superalloy was not normally applied. After welding, the soundness of the weldments was investigated by ultrasonic, tensile, and bending tests. In the present paper, in order to understand the baseline of high temperature low cycle fatigue behavior for Alloy 617 welded joints, initial strain-controlled low cycle fatigue testing was performed in air at room temperature with a constant strain ratio ($R = -1$), as listed in ASTM Standard number E606-92 [12]. This paper focuses on the comparative investigation on cyclic stress response and fracture behaviors of Alloy 617 base metal and Alloy 617 welded joints under LCF loading. The cyclic stress response behaviors have been investigated at room temperature condition in air with four different total strain ranges of 0.6, 0.9, 1.2, and 1.5%. And also, to clearly compare the low cycle fatigue fracture modes of Alloy 617 base metal and the welded joint specimens, the microscopic investigations were examined for selected specimens.

2. Experimental Procedures

2.1. Materials and Specimens. The chemical composition of the Alloy 617 (UNS 06617) used in this study is given in Table 1. The amount of each element was well within the ASTM Standard B 168-08 specifications [13]. Base metal specimens were machined from 25 mm thick rolled plate and the weld joint specimens were machined from gas tungsten arc welding (GTAW) butt-welded plate such that the loading direction was oriented transverse to the welding direction. Fatigue specimens especially for weld joint, used for this experiment, were machined and located in the upper side of weld pad as seen in Figure 1(a). Figure 1(b) shows the cylindrical specimen's shape and dimensions of LCF specimens with 6.0 mm of diameter in the reduced section with a parallel length of 18 mm and a gauge length of 12.5 mm. The cross weld specimens that were machined from the weld pad have a reduced section contained BM, Heat Affected Zone (HAZ), and WM with the optical microstructures which have been shown in Figure 2, respectively. The welded specimens were prepared which have a single V-groove of

80° of an angle and joined from the GTAW process. Hence, a filler metal was used for KW-T617 (brand name). It was prepared according the AWS specifications, AWS A 5.14-05 ERNiCrMo-1 (UNS N06617), and the diameter was 2.4 mm. After welding process, the soundness of the weldments was evaluated by ultrasonic, tensile, and bending tests. The details of the welding procedure are shown in [1].

2.2. Low Cycle Fatigue Test Procedures. Fully reversed ($R = -1$) total axial strain-controlled LCF tests were conducted at four different total strain ranges of 1.5, 1.2, 0.9, and 0.6% at room temperature on Alloy 617 base metal (BM) and Alloy 617 welded joints (WJ) in air by using a servohydraulic machine (Instron 8516 capacity 100 kN) equipped at a constant frequency of 0.25 Hz. Consequently, the strain rate was varied between $3 \cdot 10^{-3} \text{ s}^{-1}$ and $7.5 \cdot 10^{-3} \text{ s}^{-1}$ depending on total strain range. According to [7, 10, 14], fatigue life could be defined to a 20–30% drop in the maximum tensile stress measured at half-life, when the tests were terminated based upon 100% peak load drop of the stable value or complete fracture. The fatigue life is not very sensitive to the exact value of load drop used to define failure because of the rapidly falling peak stress during the final crack propagation phase. A triangular strain-time wave form was employed for all tests. In the all tests, the push-pull mode ramp rates are equal. A closed loop servohydraulic testing system equipped with a high precision extensometer with 12.5 mm gage length was attached to the gauge section for carefully monitoring and recording the real time data of stress and strain in detail. Furthermore, the fatigue crack initiation and propagation mechanisms were investigated to discover the fracture mode and the failure mechanism of this material for selected specimens by using optical microscopy (OM) and scanning electron microscopy (SEM). The specimens for OM observations were prepared by cutting into two parts which then mounted and polished the cut surface. Afterward, the specimens were etched in a solution containing hydrochloric acid, ethanol, and copper II chloride.

3. Results and Discussion

3.1. Tensile Properties and Cyclic Stress Response Behavior. The tensile tests have been first done as a reference data for Alloy 617 BM and Alloy 617 WJ. The tensile test specimens were machined into a rectangular cross section with a gage length of 28.5 mm, width of 6.25 mm, and thickness of 1.5 mm. Further details of the tensile test preparation can be found in [1]. Figure 3 shows the stress-strain curves for BM and weldment specimens. The unique tensile properties were observed from each specimens. Table 2 shows the results of the tensile property measurements at RT condition. However, the WJ

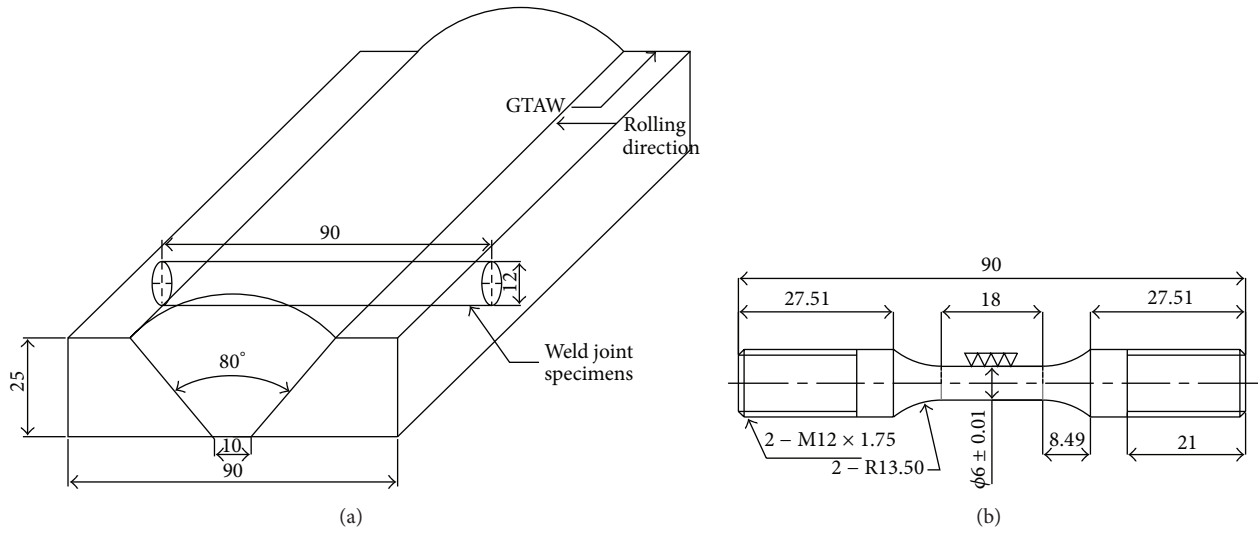


FIGURE 1: (a) The weld pad configuration for WJ specimen. (b) The cylindrical specimen's shape and dimension for Alloy 617 BM and Alloy 617 WJ.

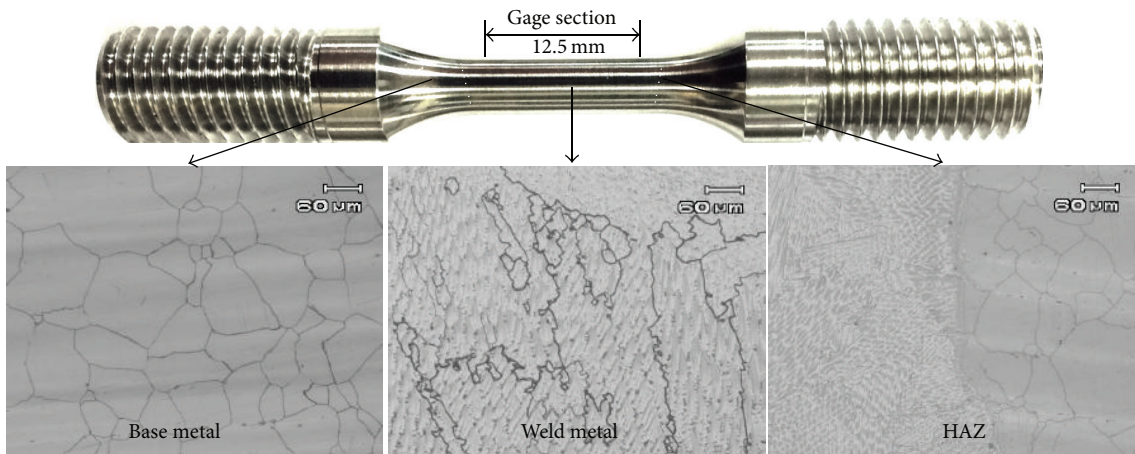


FIGURE 2: Microstructures with respect to LCF welded specimen.

specimen showed a higher 0.2% yield stress (YS) value than that of the BM at RT operation. It is notable that the ultimate tensile strength (UTS) values of the BM were comparatively higher than the WJ. Therefore, the BM ductility from the tensile elongation increased significantly compared with that of the WJ.

For strain-controlled tests, a material's cyclic stress response behavior can be characterized by examining its stress response as a function of cycle number. Generally, a material's initial response during LCF is to harden through a small number of cycles and then reach a period of either cyclic saturation or cyclic softening, depending on the microstructure and temperature and total strain range [15]. Comparison of peak and valley stresses response curves at total strain range conditions of (a) 0.6% and (b) 1.5% as a function of number of cycles to failure is illustrated in Figure 4 under continuous cyclic loading condition. The cyclic stress response was almost symmetrical in tension and compression.

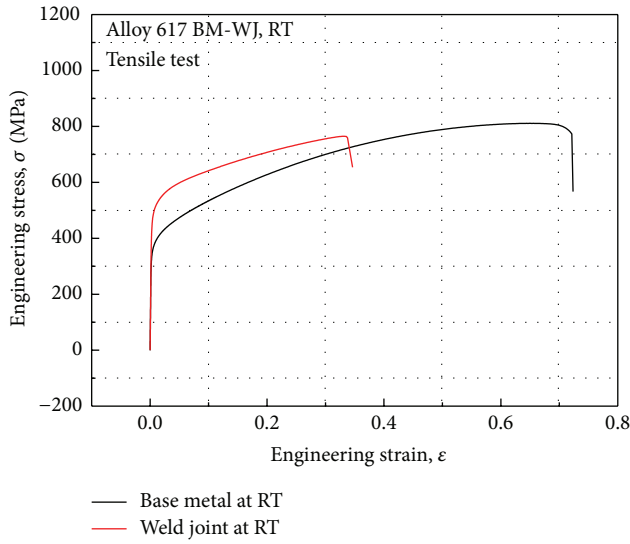
As shown in Figure 4, the WJs exhibit a higher cyclic stress response compared with that of the BMs, because of the harder zone in WJ. It is believed that higher stress range caused a short life in WJs. And also, the stress amplitude response curves at four total strain ranges as a function of number of cycles to failure are illustrated in Figure 5 under continuous cyclic loading. The cyclic stress response for both BM and WJ exhibited a cyclic softening regime for the major portion of the life after a brief period of initial hardening. The short period of cyclic initial hardening was observed about 2–200 cycles for both BM and WJ specimens and remained softening phase until failure. At the lower strain range (0.6%), the saturation regime was also visible. The similar cyclic stress response behavior was exhibited for both BM and WJ specimens. However, the WJ specimens showed a slow degradation in stress amplitude response compared to the BM specimens. About the end of the tests, the stress amplitude decreased rapidly, indicating the formation of microcracks and their subsequent growth [16]. In order to

TABLE 2: The tensile mechanical properties of Alloy 617.

Temp. (°C)	Base metal			Weld joint (GTAW)		
	YS (MPa)	UTS (MPa)	EL (%)	YS (MPa)	UTS (MPa)	EL (%)
RT	346.6	811.1	59.9	462	764.9	24.6

TABLE 3: The experimental results of LCF for Alloy 617 BM and Alloy 617 WJ.

Specimen reference	N_f	$\Delta\varepsilon_T$ (%)	$\Delta\varepsilon_e/2$ (%)	$\Delta\varepsilon_p/2$ (%)	$\Delta\sigma/2$ (MPa)	Specimen reference	N_f	$\Delta\varepsilon_T$ (%)	$\Delta\varepsilon_e/2$ (%)	$\Delta\varepsilon_p/2$ (%)	$\Delta\sigma/2$ (MPa)
BM-RT150	1409	1.5	0.315	0.435	583.037	WJ-RT150	416	1.5	0.367	0.383	665.854
BM-RT120	3410	1.2	0.279	0.321	552.406	WJ-RT120	1485	1.2	0.326	0.274	656.179
BM-RT090	13042	0.9	0.245	0.205	505.539	WJ-RT090	2924	0.9	0.293	0.157	621.123
BM-RT060	42360	0.6	0.222	0.078	474.208	WJ-RT060	28422	0.6	0.273	0.027	545.578

FIGURE 3: Stress-strain curves for Alloy 617 BM and Alloy 617 WJ in tensile tests at RT condition with a strain rate of 5.85×10^{-4} 1/s.

clearly investigate the effects of initial cyclic hardening for BM and WJ specimens, the cyclic hardening factor is considered. The cyclic hardening factor can be calculated as follows [17]:

$$H_s = \frac{(\sigma_a)^p - (\sigma_a)^1}{(\sigma_a)^1} \times 100\%, \quad (1)$$

where σ_a^p is the stable stress amplitude and σ_a^1 is the stress amplitude at the first cycle. The dependence of cyclic hardening on total strain range is shown in Figure 6. The degree of cyclic strain hardening for BM specimens increased linearly with total strain range. However, Alloy 617 WJ specimens in this work increased to 1.2% total strain range and slightly decreased at 1.5% of total strain range. The BM specimens showed relatively higher value of H_s compared to WJ specimens at all total strain ranges.

In order to further investigate the nature of cyclic stress response for BM and WJ specimens, the stable hysteresis loops were evaluated and investigated at half-life period of fatigue life. Figure 7 shows the shape of the hysteresis loops

for (a) Alloy 617 BM and (b) Alloy 617 WJ specimens in each total strain range at room temperature. The stable loop remains unchanged until the crack initiation occurs. At the half-life cycle, the hysteresis loops were all asymmetric at both BM and WJ specimens, where the peak stresses of WJ specimen at each total strain range were greater than the BM. The shape shows significant dependence on the material property (namely, BM and WJ) and total strain range, normally short and fat for the BM, while the WJ shows long and narrow hysteresis loop. The presented hysteresis loops showed that the total stress range increases with increasing total strain range, as known monotonic strain hardening behavior [15].

3.2. Fatigue Life Evaluation. From the viewpoint of engineering applications, the best way to describe the low cycle fatigue behavior is to use the fatigue life of the alloy as a function of total strain ranges at the BM and WJ, shown in Table 3. It was found that the material properties had a significant influence on the LCF life. The LCF fatigue resistance of the BM is higher than the WJ due to mechanical aspect as well as fine grain size and slip band grain boundary interaction at all the testing conditions. It should be pointed out that the total strain range governs the stress level in this investigation. The fatigue life-strain relationship under the total strain range controlled condition is often described using the Coffin-Manson equation, which is

$$\frac{\Delta\varepsilon_t}{2} = \varepsilon_f' (2N_f)^c + \frac{\sigma_f'}{E} (2N_f)^b, \quad (2)$$

where $\Delta\varepsilon_t/2$ is the total strain amplitude, $\Delta\varepsilon_e/2$ is the elastic strain amplitude, $\Delta\varepsilon_p/2$ is the plastic strain amplitude, and $2N_f$ is the number of reversals to failure. σ_f' is the fatigue strength coefficient, b is the fatigue strength exponent, ε_f' is the fatigue ductility coefficient, c is the fatigue ductility exponent, and E is the elastic modulus.

Figure 8 shows the Coffin-Manson equation plots for the BM and WJ specimens. Those data were analyzed using a least squares fit method, and the coefficients and exponents in the Coffin-Manson equation were determined and are listed in Table 4. The material constants K' and n' are cyclic

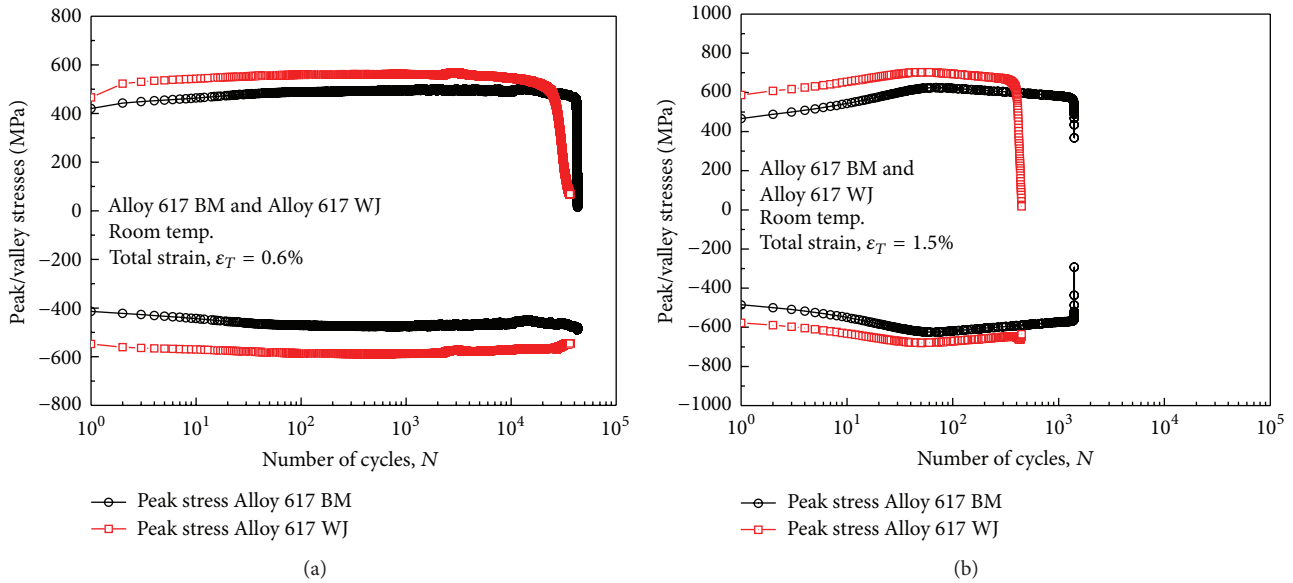


FIGURE 4: Peak/valley stresses versus number of cycles in LCF with total strain controlled of (a) 0.6% and (b) 1.5%.

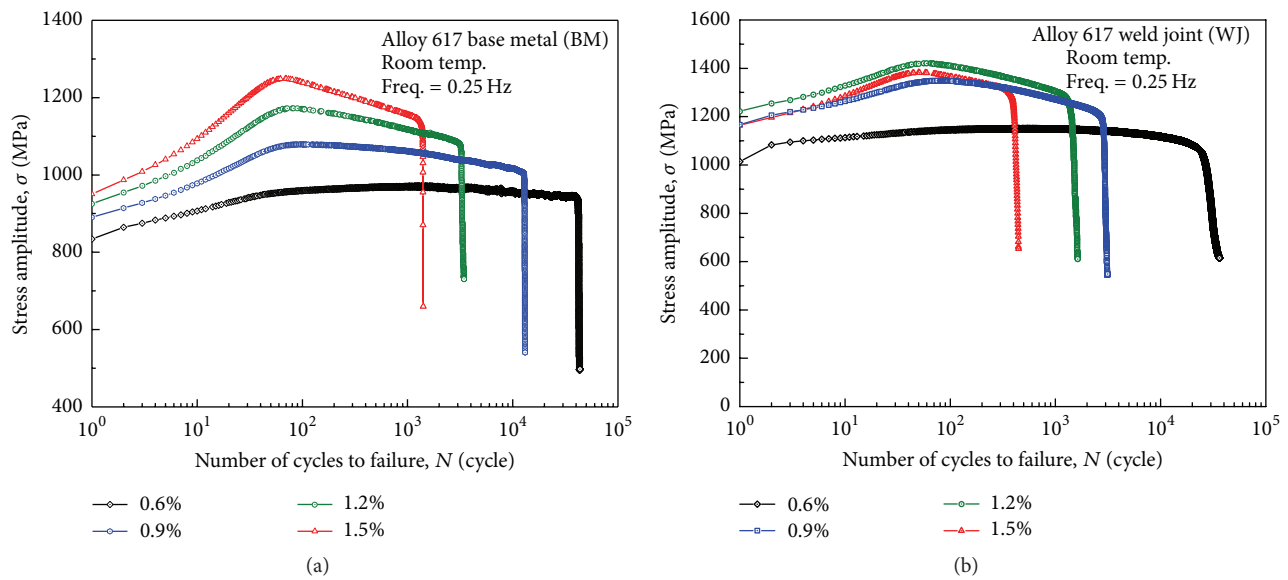


FIGURE 5: The stress amplitude as a function of number of cycles for (a) Alloy 617 BM and (b) Alloy 617 WJ.

strength coefficient and cyclic strain hardening exponent. Those values were obtained by fitting a power law relationship to the stress amplitude. The strain-life curves were simply fitted and related to (2). In both logarithmic coordinates, those that were plotted by two straight lines with slopes b and c , the intercepts with the vertical axis of the two straight lines represent the constants σ_f'/E and ϵ_f' . It is obvious that the cyclic lives were found to be strong function of material property, namely, BM and WJ. At higher total strain ranges, the plastic strain tends to be higher than the elastic strain and plays a dominant role for dislocations. The fatigue resistance of WJ specimen is lower than that of BM specimen.

In Figure 8, although the alloys exhibit similar elastic fatigue life, the ductility of the BM is superior to that of the

WJ, which is responsible for their longer transition of fatigue life, N_t [17]. From the regression parameters that are listed in Table 4, we can back substitute the values at any desired conditions to obtain the predicted lives. The LCF lives of the BM and WJ can be predicted by the Coffin-Manson equations and well coincided with the experimental data.

3.3. Fracture behavior of the BM and WJ. It is interesting to note that the fracture surface morphologies between the BM and WJ distinctly showed different crack mechanism. Figure 9 shows fractured specimens that illustrate failure occurring inside of the gauge section for BM and WJ. Cracks in BM specimen are flat-type related to the fatigue loading direction, whereas the WJ reveals relatively wedge-type

TABLE 4: Coefficients and exponents for regression analysis of the BM and WJ.

Specimen	ε'_f	c	σ'_f (MPa)	b	\bar{E} (GPa)	n'	K'
BM-RT	0.501	-0.567	1519.55	-0.104	214.4	0.118	1086.43
WJ-RT	0.398	-0.654	1213.04	-0.069	214.4	0.076	1023.29

TABLE 5: The schematic diagrams of failure pattern for Alloy 617 BM and Alloy 617 WJ tested at RT.

Specimen type	Total strain ranges (%)				Failure mode
	0.6	0.9	1.2	1.5	
Base metal					
Weld joint					

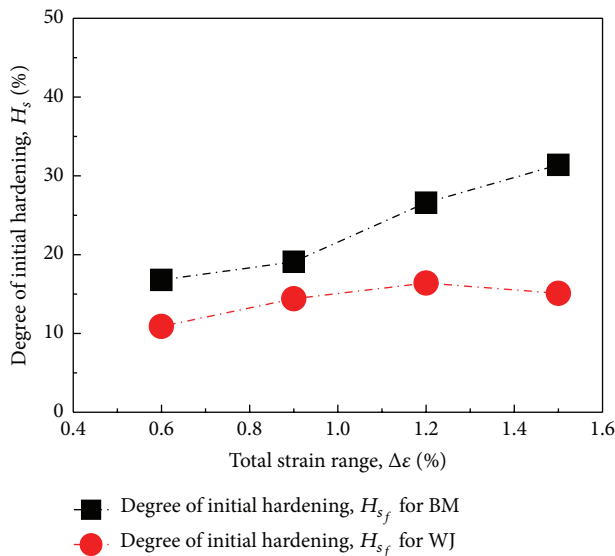


FIGURE 6: The degree of cyclic hardening factor on total strain range in Alloy 617 BM and Alloy 617 WJ.

(star/shear shape), as shown in Figure 9. However, as total strain range levels increased, the fracture mode of the WJ progressively changed into flat mechanism. The schematic diagrams of failure pattern for BM and WJ specimens are shown in Table 5. Table 5 represents a more damaging effect

of differentiation in material property on life reduction, on the base information of the surface of failed samples that the crack source (CS) for the BM is located at one point of specimen surface; conversely, the crack initiation for WJ specimens emerged from multiple points on the specimen surface.

In this investigation, the continuous cycling tested specimens were examined using SEM (Hitach JEOL JSM 5610) to provide a great illustration of crack initiation and propagation. The fracture surfaces of crack initiation and propagation of Alloy 617 BM are revealed in Figure 10. SEM image of fracture surface for BM specimen shows the transgranular crack initiation (Figure 10(a)). Figure 10(b) shows, in the near of crack initiation site, cleavage-like features that were also observed in any fracture surface along the crack propagation and pattern of fatigue striations could be seen in BMs. With the help of the cross section of OM photograph in Figure 10(c), the fatigue crack propagation site was essentially characterized by typical fatigue striations which were perpendicular to the fatigue loading direction. The grain boundary sliding is restricted and the plastic cyclic strain provided by transgranular cracking. The transgranular cracking is more obvious in the BM specimens owing to its material properties. Eventually, the characteristics of BM are uniform and stable which caused the increasing of the fatigue crack resistance and resulted in a longer fatigue life.

Figure 11 shows typical fractograph for WJ specimen that experienced a transgranular crack initiation and propagation.

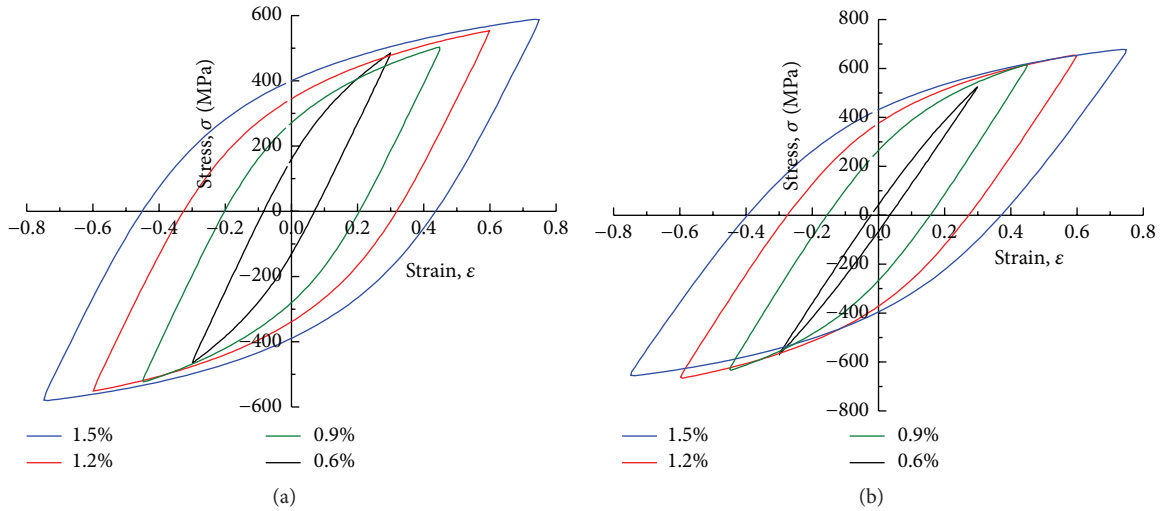


FIGURE 7: Stable hysteresis loops for a half-life at each total strain range for (a) Alloy 617 BM and (b) Alloy 617 WJ.

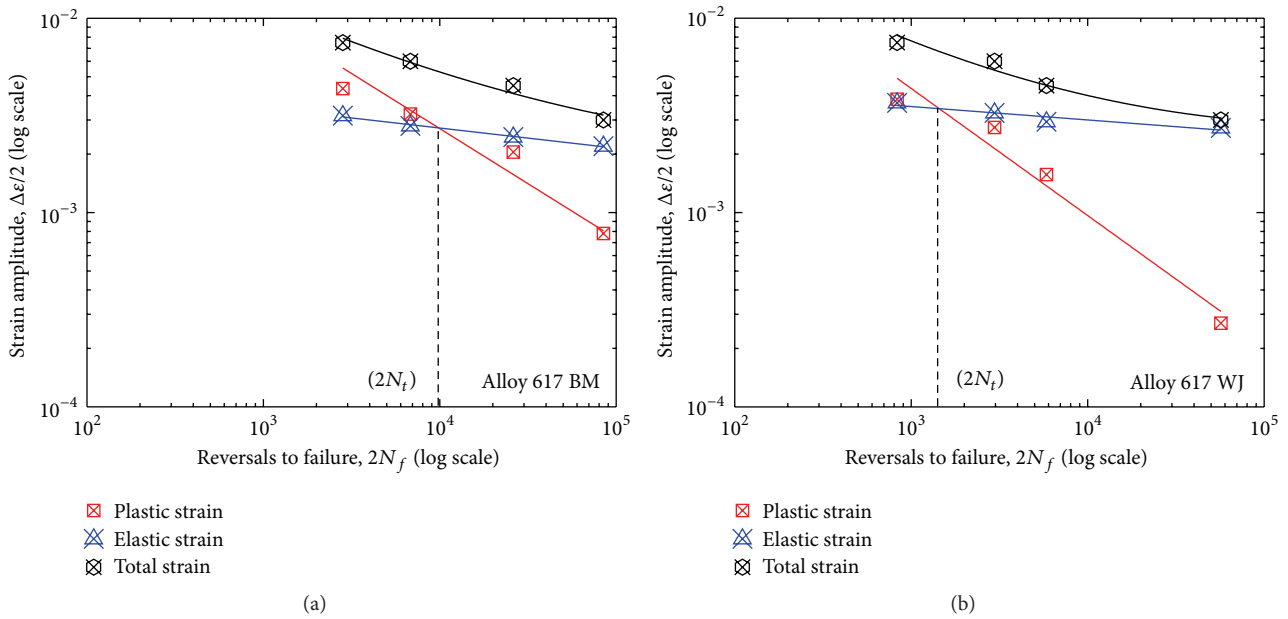


FIGURE 8: Coffin-Manson equation plots of (a) the BM and (b) the WJ.

Figure 11(a) shows SEM fractograph of several points on initiation site. However, the crack propagation stage was not significantly different than BM despite the dissimilarity in microstructure. The propagation mode for WJ appears to be sharper edges which followed dendritic paths and the fatigue striation was observed in the high magnification SEM image, shown in Figure 11(b). Shankar et al. reported for high strength materials [18] that the resistance to transgranular crack propagation in HAZ is less due to its coarse-grain size; that is, the smaller the grain boundary area, the less the number of crack-arrest events that causes the crack front to be held back and necessitates the crack initiation phase to occur in the adjacent grain. Somehow the fatigue life was less for WJs relative to those of BMs due to localized strain concentration in the HAZ region. Polák and Man [19] stated

that the fatigue crack initiation in crystalline materials is related to the strain localization in the form of slip bands. This localized plastic strain results from dislocation mechanics which play an important role in the fatigue response of the material. The role of slip bands that contain extrusions and intrusions leads to the production of point defects that will develop into small cracks. At the beginning, the WJ may have original some defects in the microstructures [1] that could accelerate initiation for cracking during the service. Typical OM image of fracture surface in Figure 11(c) shows that the transgranular crack initiation of 45 degrees normal to the fatigue loading direction and failure occurred in the weld metal zone. It is interesting to note that such crack path deviations are obvious in this work. This could be associated with the heterogeneities which contribute to significant local

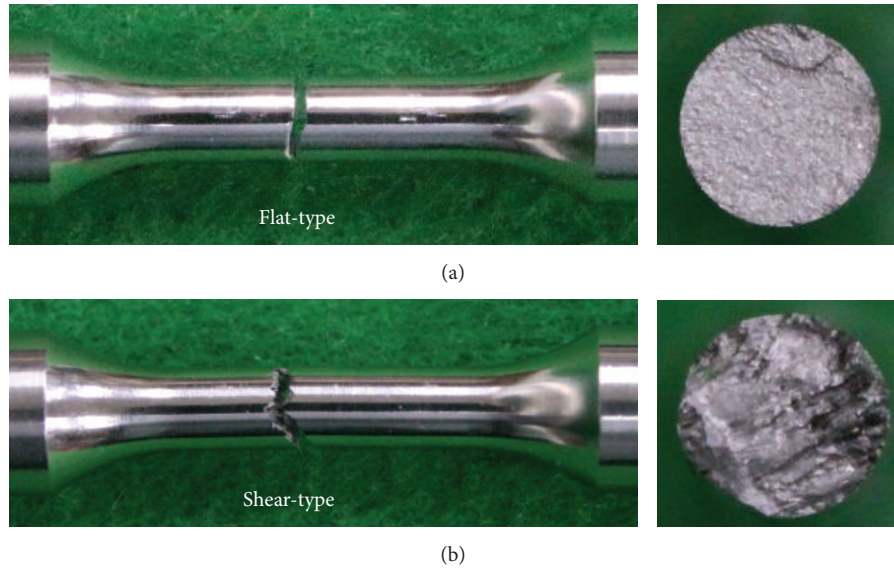


FIGURE 9: The fracture surface morphologies for (a) the BM and (b) WJ tested under total strain range, 0.6% condition.

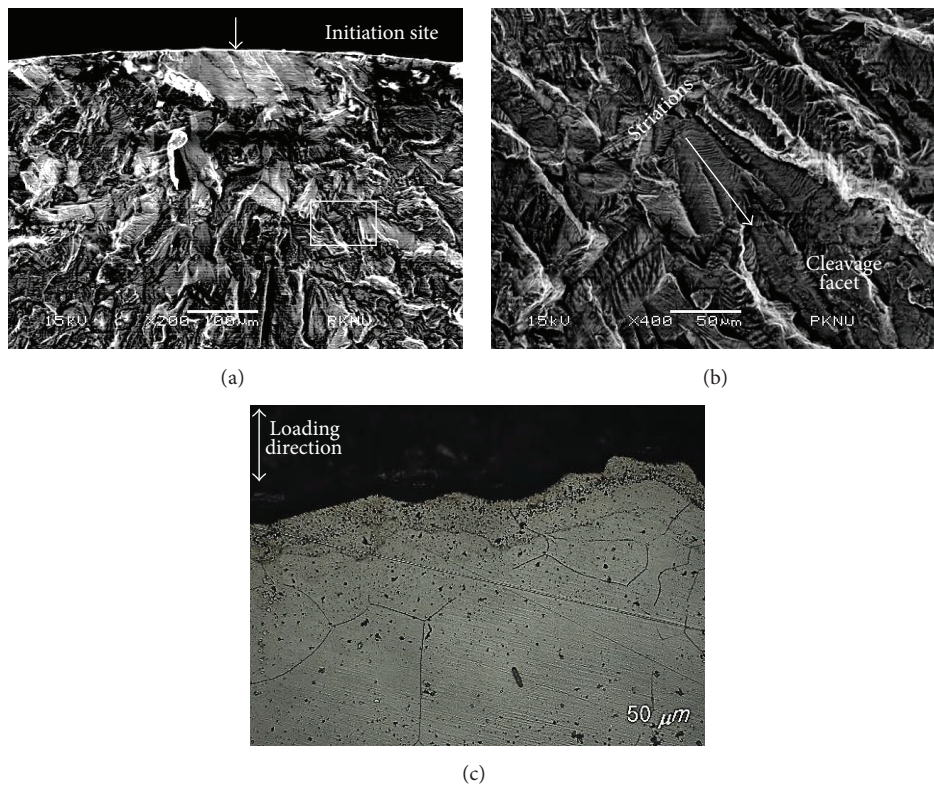


FIGURE 10: (a) SEM images representing a crack initiation site; (b) typical propagation SEM image showing fatigue striations; and (c) cross-sectional OM image of surfaces for Alloy 617 BM tested at 0.6% total strain range.

variations in the crack propagation at WJ specimens and also the coarse grain size in the weld metal zone and agree with the findings of previous work on Alloy 617 weldments [10]. Previously, Kim et al. [1] investigated the measurement of hardness for Alloy 617 welded joints; it showed that the weld zone showed a sharp increase compared to the BM and WM region because it was affected by thermal generated during

the welding process. In particular pay attention to the fact that the possible weakness of the WM as well as the presence of microstructural heterogeneity, including the coarse grain size, can cause a reduction in fatigue resistance.

Figure 12 shows typical SEM fractographs of failed specimens tested at 1.5% total strain range for BM and WJ specimens. The failure region is larger at higher strain

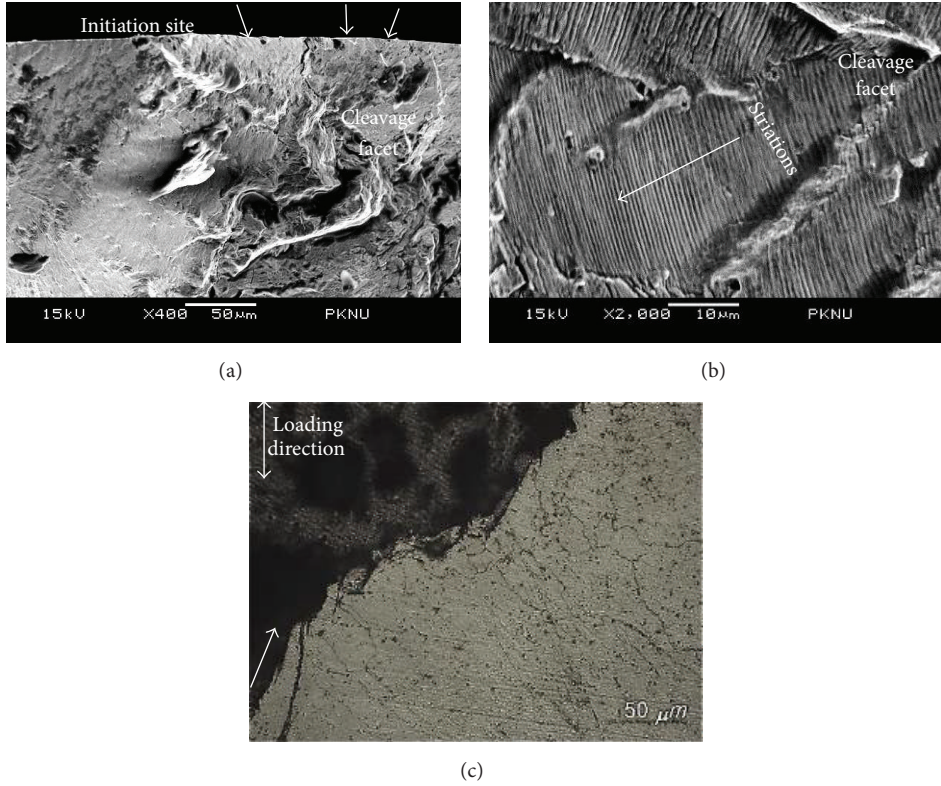


FIGURE 11: (a) SEM fractograph; (b) the crack propagation stage; (c) OM view of the fracture surfaces for Alloy 617 WJ tested at 0.6% total strain range.

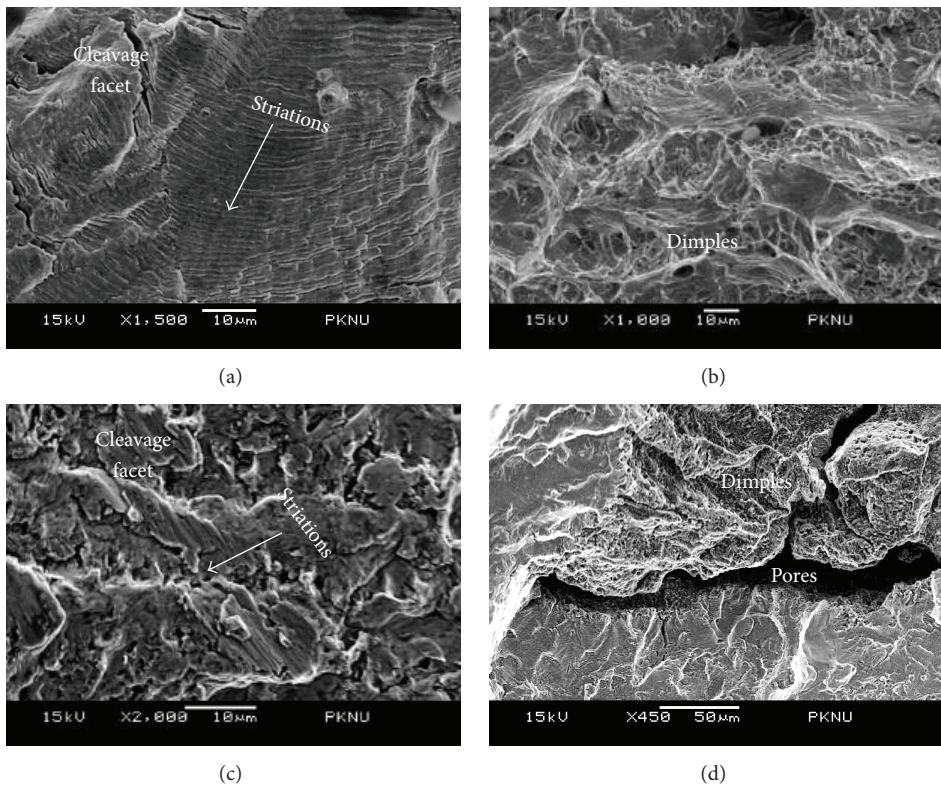


FIGURE 12: SEM images of the fractograph representing a crack propagation for low and high magnifications for ((a), (b)) Alloy 617 BM and ((c), (d)) Alloy 617 WJ, tested at 1.5% total strain range, respectively.

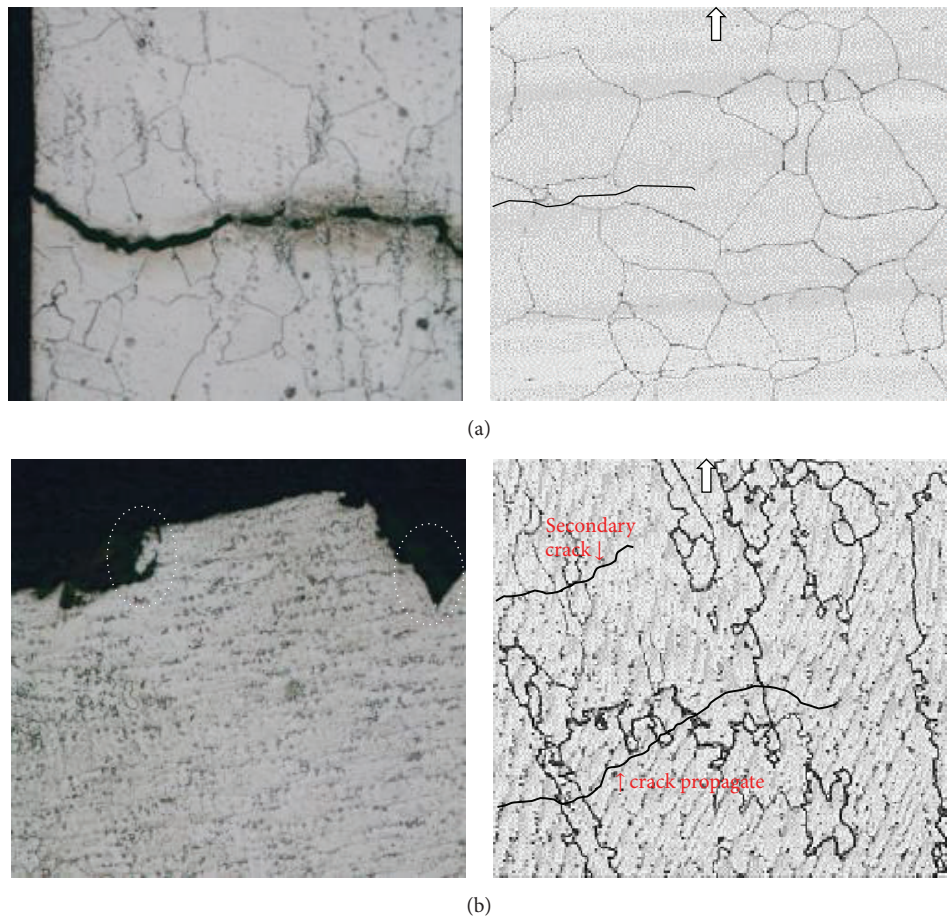


FIGURE 13: Schematic illustrations of the failure mechanism in pure fatigue representing a transgranular crack initiation and propagation along the fracture surfaces for (a) Alloy 617 BM and (b) Alloy 617 WJ, tested at 1.5% total strain range, RT.

range and somehow the propagation stage looks different. In Figures 12(a) and 12(c), the propagation area of samples tested at a higher strain amplitude of 1.5% had a smaller propagation area in both BM and WJ, compared with the samples tested at a lower strain amplitude of 0.6% (Figures 10 and 11), due to the higher cyclic stress response. The spacing of well-developed striations was also observed to be larger with increase in total strain range. However, at higher strain range, the fatigue striations will not be seen clearly in WJ due to reduction in crack propagation rate and fatigue life. Figures 12(b) and 12(d) show the propagation stage that was taken at higher magnification for BM and WJ, respectively. The fact that the WJ represents more obvious sharp edges and cleavage facets followed dendritic paths with several pores located at higher strain range. However, fracture surfaces show dimple ruptures due to the occurrence of microvoids in the failure region for BM and WJ tested at 1.5% total strain range. Furthermore, the size of the crack propagation area was mainly associated with the applied strain amplitude in both BMs and WJ specimens. The higher the applied total strain range was, the smaller the propagation area was.

The LCF failure mode outlined above has been presented in advance at room temperature and selected total strain condition. The mode is schematically illustrated and compared to micrographs of Alloy 617 crack paths in Figure 13.

It should be noted that the secondary cracks or the fracture surface could describe the mode of failure of this alloy under these specific conditions. The fatigue crack initiation and propagation are dominated by the crack that traveled cut along the grain boundaries, and it is relative to the pure fatigue phenomena. In the current work, testing condition such as temperature did not contribute well to this mechanism result, despite being at all investigated total strain ranges. The premature of crack propagation which manifests deviations in WJs (Figure 13(b)) which were expected from the presence of microstructural heterogeneity includes the dendritic structure.

Future work for high temperature LCF testing is planned specifically on all WJ specimens to distinguish the fatigue behavior of Alloy 617 welded joints by GTAW process.

4. Conclusions

The strain-controlled LCF testing of Alloy 617 base metal and Alloy 617 the welded joints was performed at four different total strain ranges, 0.6, 0.9, 1.2, and 1.5% at room temperature in air conditions. The cyclic stress response for both BM and WJ specimens exhibited a cyclic softening regime for the major portion of the fatigue life after a brief period of initial hardening. The short period of cyclic initial hardening

was observed about 2–200 cycles for both BM and WJ specimens and remained softening phase until failure. The WJ specimens have shown a higher cyclic stress response than the BM specimens. Contrarily, the BM showed a higher value of degree of initial hardening, H_s , compared to WJ. Furthermore, the material constants have been evaluated and characterized by the Coffin-Manson relationship. The great results appeared and can be well compared with the experimental data.

Fatigue resistance was decreased with increasing the total strain ranges; thereafter the fatigue lives of WJ specimens were reduced relative to those of BM specimens. The low cycle fatigue crack initiation and propagation occurred in transgranular mode for BM and WJ specimens in this work. Furthermore, the fracture behavior of the BM is very flat related to the fatigue loading axis, whereas that of the WJ is relatively wedge-type (star/shear shape) and consequently transgranular cracking initiation is 45 degrees normal to the fatigue loading axis. Cracks in WJ specimens initiated in weld metal region.

Conflict of Interests

The authors declare that there is no conflict of interests regarding the publication of this paper.

Acknowledgment

This research was supported by Nuclear Research & Development Program through the National Research Foundation of Korea (NRF) funded by the Ministry of Science, ICT & Future Planning (NRF-2014M2A8A2020785).

References

- [1] W.-G. Kim, J.-Y. Park, I. M. W. Ekaputra, S.-D. Hong, S.-J. Kim, and Y.-W. Kim, "Comparative study on the high-temperature tensile and creep properties of Alloy 617 base and weld metals," *Journal of Mechanical Science and Technology*, vol. 27, no. 8, pp. 2331–2340, 2013.
- [2] S. J. Kim, P. H. Choi, R. T. Dewa, W. G. Kim, and M. H. Kim, "Low cycle fatigue properties of Alloy 617 base metal and weld joint at Room Temperature," *Procedia Materials Science*, vol. 3, pp. 2201–2206, 2014.
- [3] J. P. Strizak, C. R. Brinkman, and P. L. Rittenhouse, "High temperature low-cycle fatigue and tensile properties of Hastelloy X and alloy 617 in air and HTGR-helium," in *Proceedings of the IAEA Specialists' Meeting on 'High Temperature Metallic Materials for Application in Gas Cooled Reactors'*, Oak Ridge National Laboratory, Vienna, Austria, May 1981.
- [4] H. Nickel, F. Schubert, and H. Schuster, "Evaluation of alloys for advanced high-temperature reactor systems," *Nuclear Engineering and Design*, vol. 78, no. 2, pp. 251–265, 1984.
- [5] L. J. Carroll, C. Cabet, M. C. Carroll, and R. N. Wright, "The development of microstructural damage during high temperature creep-fatigue of a nickel alloy," *International Journal of Fatigue*, vol. 47, pp. 115–125, 2013.
- [6] X. Chen, Z. Yang, M. A. Sokolov, D. L. Erdman III, K. Mo, and J. F. Stubbins, "Effect of creep and oxidation on reduced fatigue life of Ni-based alloy 617 at 850 °C," *Journal of Nuclear Materials*, vol. 444, no. 1–3, pp. 393–403, 2014.
- [7] T. C. Totemeier and H. Tian, "Creep-fatigue interactions in INCONEL 617," *Materials Science and Engineering A*, vol. 468–470, pp. 81–87, 2007.
- [8] K. B. S. Rao, H. Schiffers, H. Schuster, and H. Nickel, "Influence of time and temperature dependent processes on strain controlled low cycle fatigue behavior of alloy 617," *Metallurgical Transactions A*, vol. 19, no. 2, pp. 359–371, 1988.
- [9] M. A. Burke and C. G. Beck, "The high temperature low cycle fatigue behavior of the nickel base Alloy IN-617," *Metallurgical Transactions. A*, vol. 15, no. 4, pp. 661–670, 1984.
- [10] T. C. Totemeier, "High-temperature creep-fatigue of alloy 617 base metal and weldments," in *Proceedings of the 8th International Conference on Creep and Fatigue at Elevated Temperatures, ASME Pressure Vessels and Piping Conference*, vol. 9, pp. 255–260, July 2007.
- [11] G. V. P. Reddy, R. Sandhya, M. Valsan, and K. B. S. Rao, "High temperature low cycle fatigue properties of 316(N) weld metal and 316L(N)/316(N) weld joints," *International Journal of Fatigue*, vol. 30, no. 3, pp. 538–546, 2008.
- [12] ASTM International, "ASTM E 606-92, standard practice for strain-controlled fatigue testing," in *Annual Book of ASTM Standards*, vol. 03.01, p. 569, ASTM International, Baltimore, Md, USA, 2002.
- [13] ASTM International, *Standard Specification for Nickel-Chromium-Iron Alloys (UNS N06600, N06601, N06603, N06690, N06693, N06025, N06045, and N06696) and Nickel-Chromium Cobalt Molybdenum Alloy (UNS N06617) Plate, Sheet, and Strip*, ASTM International, West Conshohocken, Pa, USA, 2008.
- [14] O. Fatoba and R. Akid, "Low cycle fatigue behaviour of API 5L X65 pipeline steel at room temperature," *Procedia Engineering*, vol. 74, pp. 279–286, 2014.
- [15] J. K. Wright, L. J. Carroll, J. A. Simpson, and R. N. Wright, "Low cycle fatigue of alloy 617 at 850 °C and 950 °C," *Transactions of the ASME—Journal of Engineering Materials and Technology*, vol. 135, no. 3, Article ID 031005, 8 pages, 2013.
- [16] K. B. S. Rao, H. Schuster, and G. R. Halford, "Mechanisms of high-temperature fatigue failure in alloy 800H," *Metallurgical and Materials Transactions A: Physical Metallurgy and Materials Science*, vol. 27, no. 4, pp. 851–861, 1996.
- [17] J. Kang, F. C. Zhang, X. Y. Long, and B. Lv, "Cyclic deformation and fatigue behaviors of Hadfield manganese steel," *Materials Science and Engineering A*, vol. 591, pp. 59–68, 2014.
- [18] V. Shankar, M. Valsan, K. B. S. Rao, and S. D. Pathak, "Low cycle fatigue and creep-fatigue interaction behavior of modified 9Cr-1Mo ferritic steel and its weld joint," *Transactions of the Indian Institute of Metals*, vol. 63, no. 2-3, pp. 622–628, 2010.
- [19] J. Polák and J. Man, "Fatigue crack initiation—the role of point defects," *International Journal of Fatigue*, vol. 65, pp. 18–27, 2014.

Research Article

Corrosion Control of Alloy 690 by Shot Peening and Electropolishing under Simulated Primary Water Condition of PWRs

Kyung Mo Kim, Hee-Sang Shim, Myung Ji Seo, and Do Haeng Hur

Korea Atomic Energy Research Institute, 989-111 Daedeok-daero, Yuseong-gu, Daejeon 305-353, Republic of Korea

Correspondence should be addressed to Kyung Mo Kim; kmkim@kaeri.re.kr

Received 3 June 2015; Accepted 20 August 2015

Academic Editor: Randhir Singh

Copyright © 2015 Kyung Mo Kim et al. This is an open access article distributed under the Creative Commons Attribution License, which permits unrestricted use, distribution, and reproduction in any medium, provided the original work is properly cited.

This work clarifies the effect of surface modifications on the corrosion rate of Alloy 690, a nickel-based alloy for steam generator tubes, under the simulated test conditions of the primary water chemistry in nuclear power plants. The surface stress was modified by the shot peening and electropolishing methods. The shot peening treatment was applied using ceramic beads with different intensities by varying the air pressure and projection angle. The corrosion rate was evaluated by gravimetric analysis and the surface was analyzed by scanning electron microscopy (SEM). The corrosion rate of Alloy 690 was evaluated from the influence of the stress state on the metal surface. Based on the observation of the surface after the corrosion test, the oxide composition and its structure were affected by the surface modifications. The corrosion behavior of Alloy 690 was distinguished by the shot peening intensity on the surface, and additional electropolishing was effective at reducing the dissolution of nickel ions from the metal surface.

1. Introduction

The dissolution control of nickel from steam generator (SG) tubes is important to reduce the radioactive dose rate and deterioration of fuel performance in the operation of pressurized water reactors (PWRs). The major sources of the radiation field in the primary coolant circuit including the reactor are known to be neutron reactions with nickel and cobalt ions in water. Corrosion products released from metal surface in the coolant circuit can be deposited on the reactor core forming the crud on the fuel surface during operation of power plant. The corrosion products prevent heat transfer from the fuel to the coolant and induce the growth of crud on the fuel cladding. The composition of the fuel crud consists mainly of nickel ferrite, which indicates that its primary source is the nickel contained in the SG tube materials [1, 2]. Higher crud buildup might cause an increase in the axial offset anomalies through the corrosion products deposited on the surface of the fuel cladding [3–5]. To avoid problems originating from crud buildup, the primary water chemistry has been improved by various

means, such as loading of hydrogen overpressure, reduction of the electrochemical potential, coordinated adjustment of the boron and lithium concentration, and zinc addition [3–8]. Zinc addition in operating PWR plants shows reducing radiation dose rates [3]. It is recommended on primary chemistry control to reduce the corrosion products for PWR type plants with plant-specific optimization. These alleviation methods need an exact evaluation of chemical conditions in primary coolant and effects on component integrity [4].

The corrosion properties are affected by the material's surface states including roughness, residual stress, and work hardening under the conditions of the reactor water chemistry [9]. The Alloy 600 SG tube material has been replaced with Alloy 690, which is resistant to stress corrosion cracking. However, the metal cations released from the surface might be accumulated in the primary circuit over long operation times, and other unknown manufacturing processes may affect the integrity of the Alloy 690 surface [2]. Clauzel et al. observed the corrosion behavior of Alloy 690 manufactured from various suppliers and classified the tubes according to their metallurgical properties, release, and corrosion

TABLE 1: Chemical composition of Alloy 690.

C	Cr	Fe	Ni	Si	Mn	Ti	Al	S
0.015	28.2	9.5	Bal.	0.1	0.26	0.21	0.04	<0.002

properties in relation to microstructure, surface impurities, microhardness, roughness, and carbon content [10]. Guinard et al. [11] and Huang et al. [12] have studied the impact of different surface-state conditions, as well as the cold working, and electropolishing of Alloy 690 on its corrosion-release rate.

There are many studies on the metal-surface improvement using electropolishing and shot peening. The corrosion rate of electropolished stainless steel was lowered by more than a factor of three relative to that of machined surfaces in mild alkaline, hydrogenated water at 260°C, and this reduction was explained by the decrease in surface microstrain [13]. It is known that the higher equilibrium concentration of Cr in Alloy 690 results in good resistance against failure induced by intergranular attack (IGA) and stress corrosion cracking (SCC) in high-temperature water environments [14]. Zhang et al. reported that the SCC of Alloy 690 was reduced by shot peening and electropolishing treatments [9]. Some studies also showed that compressive residual stresses inhibit the initiation of SCC [15, 16]. However, the effects of the surface states on the corrosion and metal-ion dissolution properties of Alloy 690 have not been clearly evaluated, and the combined application of shot peening and electropolishing treatments on SG tubes needs to be experimentally studied.

The aim of this work is to study the reduction in the dissolution of metal ions from the Alloy 690 surface through surface modification in the simulated water chemistry of the primary system of PWRs. In this work, the applicability of shot peening and electropolishing on SG tube material was investigated, and the effect of these surface treatments on the corrosion-release behavior was evaluated.

2. Experimental

2.1. Material Preparation. The corrosion experiments were performed on Alloy 690 which was manufactured by POSCO Specialty Steel with the chemical composition listed in Table 1. The specimens were heat processed in two steps, namely, mill annealing (MA) and thermal treatment (TT), after being cold-rolled to the thickness of about 1.5 mm. The samples were mill annealed at 1100°C for 5 min, followed by water quenching, and then thermally treated at 715°C for 10 h in a vacuum furnace under the pressure of about 5×10^{-6} Torr. The specimens were manufactured in plate shape with size of 45 mm in length and 15 mm in width. All the specimens have a hole of 3 mm in diameter in order to hang on a tree in the autoclave for high-temperature corrosion test.

2.2. Surface Treatment. Shot peening was performed on the flat specimens using ceramic beads (0.125 ~ 0.250 mm in size). The shot peening process was conducted using a

pressure-type blast machine (MPTB-01 model) manufactured by Korea Shot Blast Co., and the maximum air pressure for the shot peening instrument was 5 bars. The intensity and coverage during the shot peening process were measured using N-type Almen strips. Almen strips are flat metal strips that were exposed to shot peening under the same conditions as the specimens. Residual surface compressive stresses will make the strip bow upward in the middle when released. The height of this convexly bowed arc is an index of the intensity of the shot peening and was measured using a TSP-3 Almen gauge (Electronics Inc., USA). The surface microstrain was determined from high-resolution X-ray diffraction (HR-XRD) measurements. For the residual stress evaluation of Alloy 690, Young's modulus of 211 GPa and Poisson's ratio of 0.289 were used.

Table 2 lists the surface-processing procedures applied for shot peening and electropolishing of the specimens. The first test was performed to investigate the effect of only varying the air pressure used for shot peening on the corrosion behavior (specimens B–D).

Further shot peening processes were conducted at different angles and distances from the nozzle of the shot peening machine, namely, at 30° and 75 mm (SP30), 45° and 100 mm (SP45), and 90° and 150 mm (SP90). In this test series, the shot peening air pressure was maintained at 1 bar for all specimens. After the shot peening treatment, the SP45 and SP90 specimens were further electropolished to improve the roughness of the shot-peened surfaces, marked as EP45 and EP90 specimens.

The electropolishing process was applied using the instrument type ElectroMet 4 (Buehler Co., IL). The electrolyte for electropolishing was a mixture of 70% phosphoric acid (H_3PO_4), 15% sulfuric acid (H_2SO_4), and 15% methanol (CH_3OH). Electropolishing was conducted at 10 V and 1.6 to 1.7 A, thereby maintaining the electrolyte temperature of 40°C and 50 cc/min circulation speed for about 1.5 min. The surface morphology and roughness were investigated by scanning electron microscopy (SEM, JEOL JSM-5400 model) and the surface microhardness was measured using a Vickers hardness tester equipped with a pyramidal diamond indenter. The loading condition was 25 g for 10 s.

2.3. Corrosion Test and Oxide Analysis. A recirculation loop with Hastelloy autoclave system was used during the long corrosion tests. The test environment simulated the primary water chemistry in a PWR. Dissolved oxygen (DO), dissolved hydrogen (DH), pH, and conductivity were monitored at room temperature using sensors manufactured by Orbisphere and Mettler Toledo. The temperature and pressure were maintained at 330°C and 150 bars, respectively, during the corrosion tests. The composition of the test solution was lithium (LiOH, 2 ppm), boron (H_3BO_4 , 1,200 ppm), DH (35 cc/kg), and less than 5 ppb of DO. The flow rate of the loop system was 3.8 L/h, and the corrosion tests were conducted for 500 h.

The corrosion rate was evaluated by gravimetric analysis using an alkaline permanganate ammonium citrate (AP/AC) descaling process: 1% $KMnO_4$ and 5% NaOH were exposed to the inner tube surface at 90°C for 3 min [17–19]. This

TABLE 2: Conditions of the specimen's surface treatments.

Specimen ID	Shot peening				Electropolishing
	Air pressure (bar)	Distance (mm)	Angle (°)	Time (sec)	
A	—	—	—	—	—
B	0.5	50	90	60	—
C	1	50	90	60	—
D	2	50	90	30	—
SP30	1	75	30	300	—
SP45	1	100	45	300	—
SP90	1	150	90	300	—
EP45	1	100	45	300	Yes
EP90	1	150	90	300	Yes

method involves multiple applications and enables reverse extrapolation to correct for base-metal losses during the removal of the corrosion oxides.

The morphology and chemical composition of the surface oxide layers were analyzed using SEM and X-ray photoelectron spectroscopy (XPS). The XPS analysis was carried out using a spectrometer model Thermo Fisher Scientific (Theta Probe AR-XPS) XPS, equipped with Al K α X-ray source (1486.6 eV) and operated at 15 kV and 150 W. The depth profiling was conducted in intervals of 60 s through Ar sputtering at the energy of 2 keV and at the spot size of 400 μ m.

3. Results and Discussion

3.1. Surface Stress State. The shot peening intensity was measured in dependence on the applied air pressure, as shown in Figure 1. The shot-peened surface shows saturation of its intensity value as the exposure time is held constant. The saturation time for a given test piece may be defined as the time necessary to attain a deflection such that, by doubling the treatment time, the deflection does not increase by more than 10%. The arc deflection at saturation defines the peening intensity. The shot peening intensity was measured to be 10.1 N at an air pressure of 2 bars and a shot peening time of 30 s. When the air pressure was reduced to 1 bar and 0.5 bars, the intensities decreased to 7.36 N and 5.51 N, respectively, for a shot peening time of 60 s. After these shot peening times, the intensity values showed no further increase.

The XRD patterns of the oxide layers are obtained to determine the crystal faces as a measure of the residual stress. The XRD patterns of the specimens shown in Figure 2 indicate that the shot peening treatment did not change the crystal structure of Alloy 690. The residual stress induced by shot peening on the surface was measured by an HR-XRD instrument, and the results are shown in Figure 3. The residual stress was measured employing the Ni crystal faces of (111) and (311) at the surface of the specimens. The two stress levels are different but show a similar pattern in dependence on the air pressure applied during the shot peening. The results indicate that specimen D shot-peened at an air pressure of 2 bars shows lower residual stress than specimen B surface treated at an air pressure of 0.5 bars,

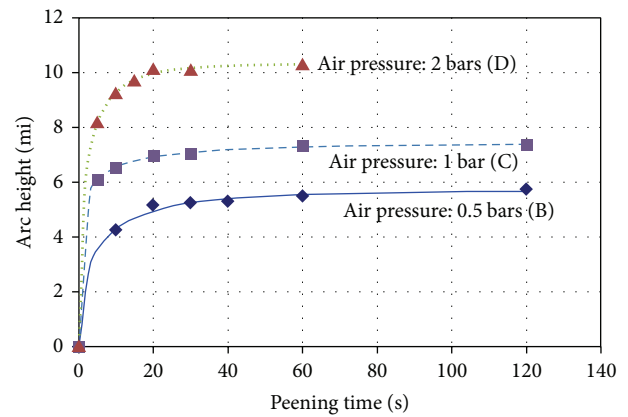


FIGURE 1: Shot peening intensity at different air pressure conditions.

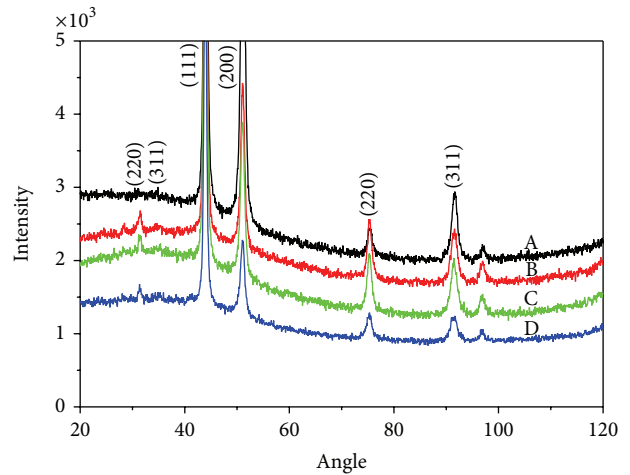


FIGURE 2: X-ray diffraction patterns of Alloy 690 at different shot peening intensity.

contrary to expectations, and it is considered with the change of surface morphology as explained with the next figures (Figures 4 and 5). In Figure 3, the Vickers microhardness indentations are depicted along with the residual stress values. The microhardness was measured at the distance of 20 μ m from the shot-peened surface. The hardness increases

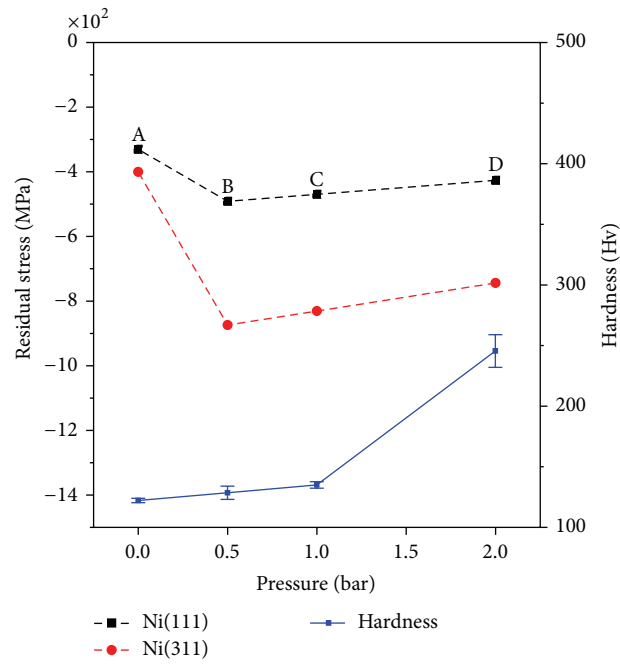


FIGURE 3: Residual stress and microhardness at different shot peening air pressure.

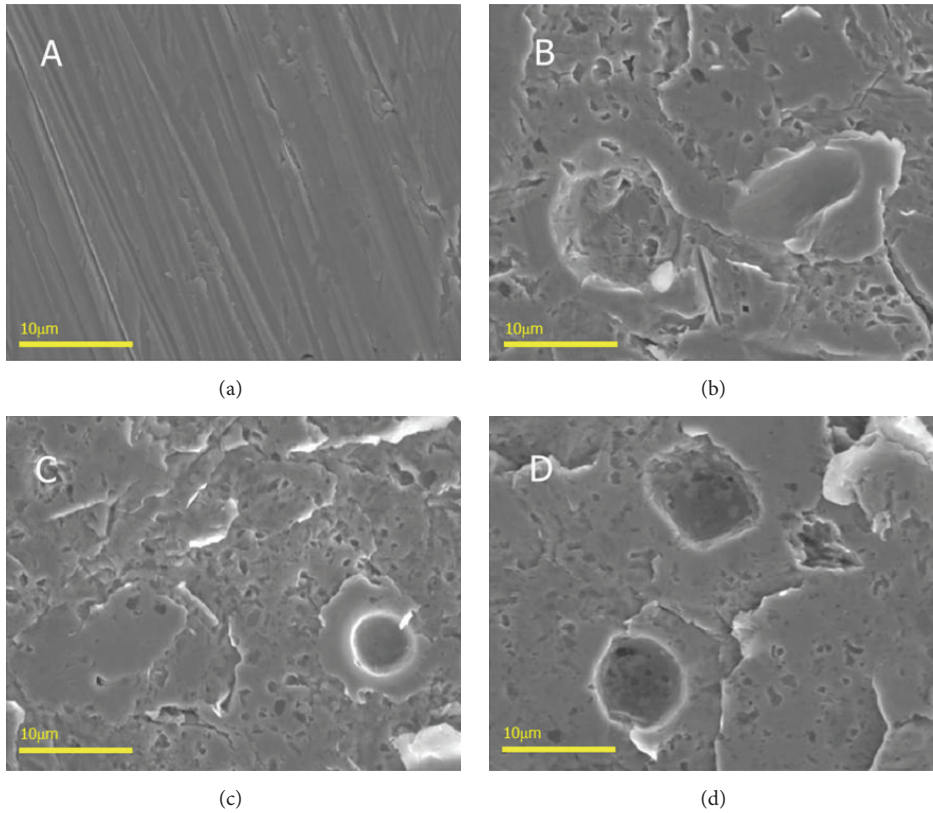


FIGURE 4: SEM photographs of the surface of shot-peened specimens at different air pressure.

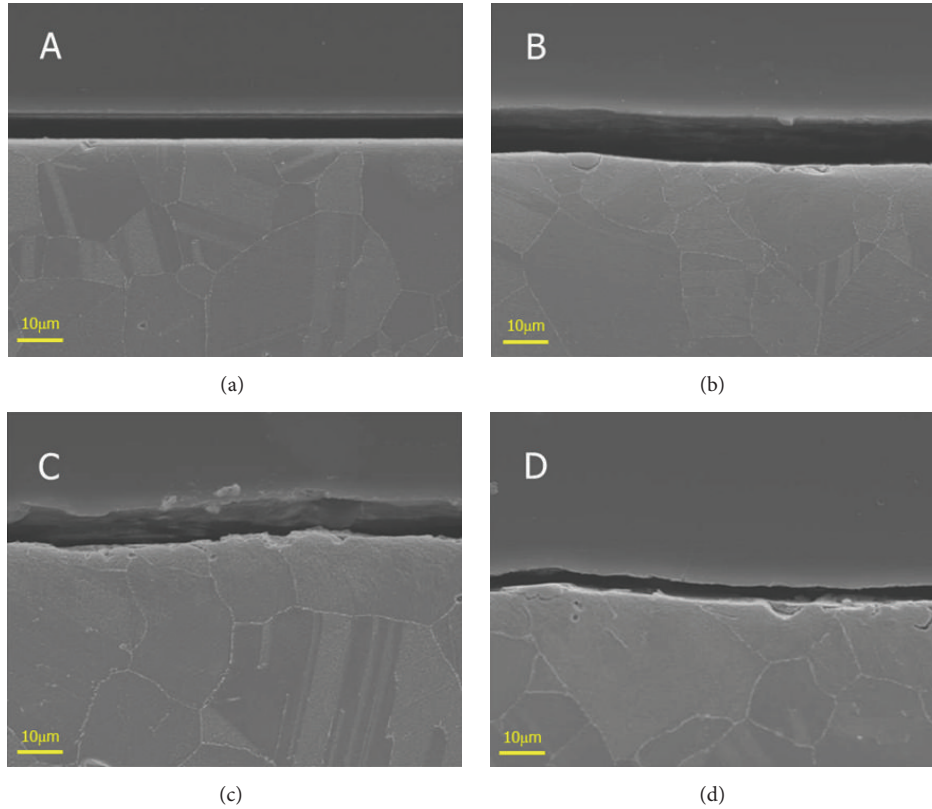


FIGURE 5: SEM photographs of the depth profile of the surface layer of shot-peened specimens at different air pressure.

with the shot peening intensity, and specimen D accordingly shows the hardest state.

The surface morphology of the specimens was observed by SEM and is shown in Figure 4. Scratches are observed at the surface of specimen A, but the shot peening treatment removes them, as shown in Figures 4(b)–4(d). The shot peening causes circular indentations and imprints of the shot peening beads at the surface are more clearly formed at increasing shot peening intensity. The surface layer of the alloy was slightly smeared and/or redistributed by the shot peening. No particle embedment is observed and the occurrence of bead contamination is not considered. The depth profile (Figure 5) shows the breakaway of some small parts at the outer surface at high shot peening intensity. The decrease of the residual stress at higher shot peening intensities of specimen D, as shown in Figure 3, can be explained as the stress relief induced from microcracking by excessive shot peening intensity over metal fracture stress.

High intensity of the shot peening (higher than about 7 N) might cause problems such as crack initiation. To improve the surface integrity, the intensities were lowered by changing the incident angle and the distance from the peening nozzle. The shot peening intensity is determined to be about 4.5–6 N based on the Almen-strip measurements, as shown in Figure 6. The intensity difference between samples SP30 and SP45 was affected more by the incidence angle than by the distance. On the other hand, the intensity value of the

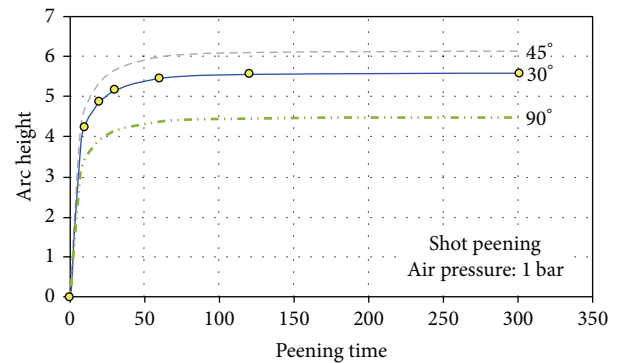


FIGURE 6: Almen-strip saturation curves at different shot peening incidence angles.

SP90 sample shows higher variation in dependence on the distance than on the angle. Figure 7 shows the values of the residual stress and microhardness. The changes induced by electropolishing after the shot peening were not large compared with the values already obtained by applying only shot peening.

The surface morphologies of all specimens are shown in Figure 8. The surfaces processed by shot peening (Figures 8(b)–8(d)) show a slightly larger number of dimples and a scaled appearance, similar to Figure 4, but these structures

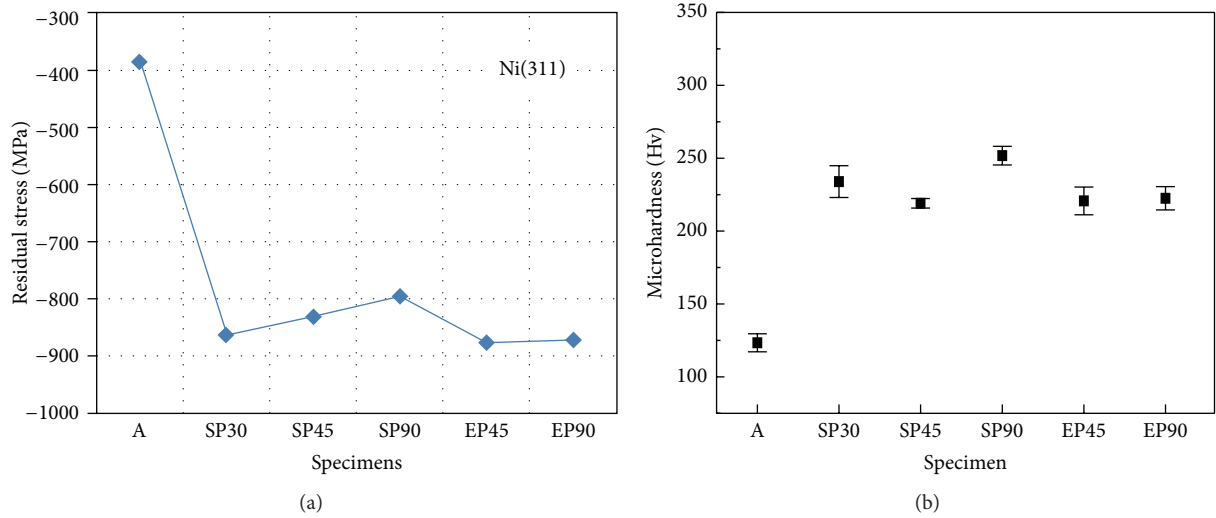


FIGURE 7: (a) Residual surface stress measured by XRD and (b) microhardness measured at the depth of $20\ \mu\text{m}$ from the surface of shot-peened and electropolished specimens. The specimen labels distinguish the different surface treatments: shot peening at 1 bar with angles of 30° (SP30), 45° (SP45), and 90° (SP90) and electropolishing after shot peening with angles of 45° (EP45) and 90° (EP90).

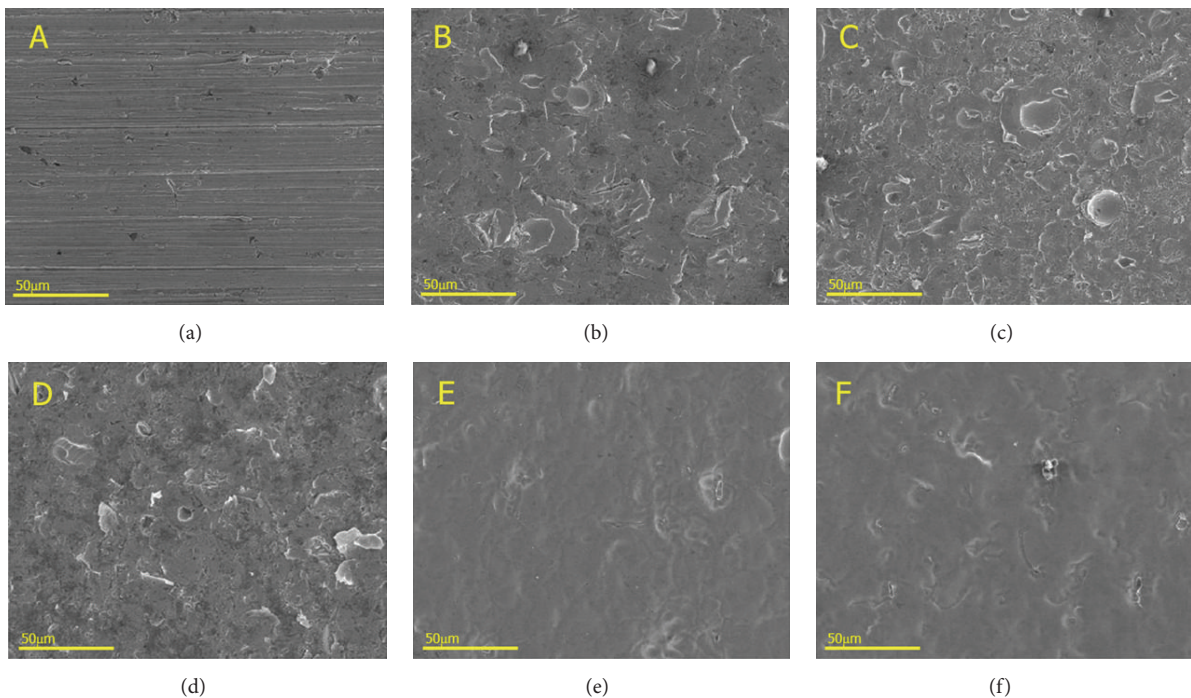


FIGURE 8: SEM photographs of the surface before the corrosion tests for specimens of (a) reference, (b) SP30, (c) SP45, (d) SP90, (e) EP45, and (f) EP90.

are formed to a lesser degree than in case of high shot peening intensity. The samples being subject to the electropolishing treatment show blunt dimples induced by the shot peening but an overall smoother surface achieved by electropolishing in comparison to the samples processed only by shot peening (Figures 8(e)–8(f)). It is known that deformation twinning and the number of dislocations increase upon increasing the peening intensity, which was inferred from TEM observations of the surface of nickel-based alloys [20].

3.2. Corrosion Behavior Modified by Surface Treatments. Immersion tests were performed using specimens processed by shot peening at different intensities with or without electropolishing treatment in primary water chemistry environment, and the corrosion rates were measured, as shown in Figure 9. The corrosion rate at different air pressures of the shot peening was measured to be $1.45\ \text{mg}/\text{m}^2\ \text{h}$ for as-received specimen A (Figure 9(a)). The corrosion rates of the specimens treated at different shot peening intensities are

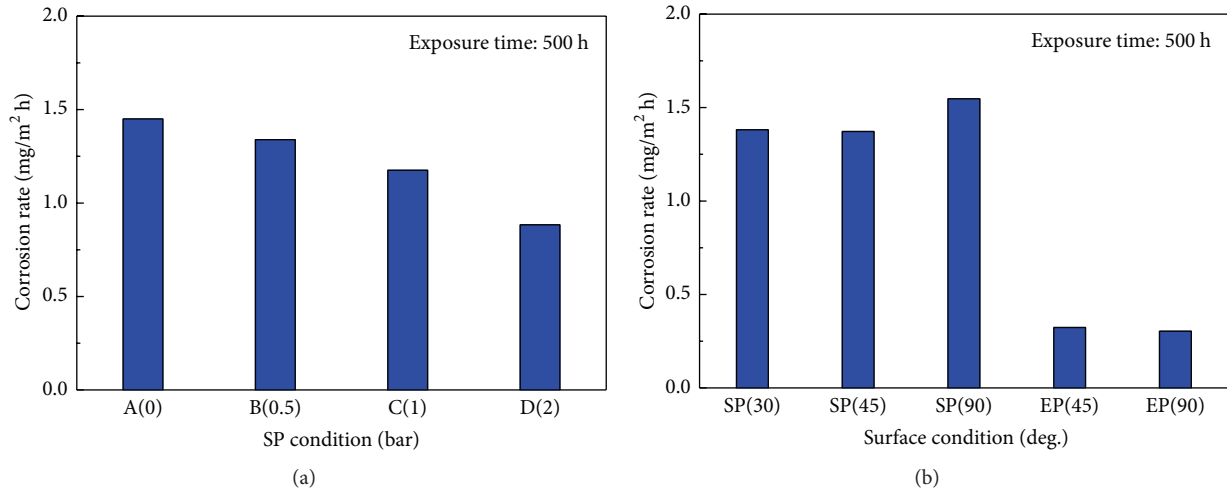


FIGURE 9: Corrosion rates of Alloy 690 processed with different surface treatments: variation of the shot peening air pressure (a) and incidence angle (b).

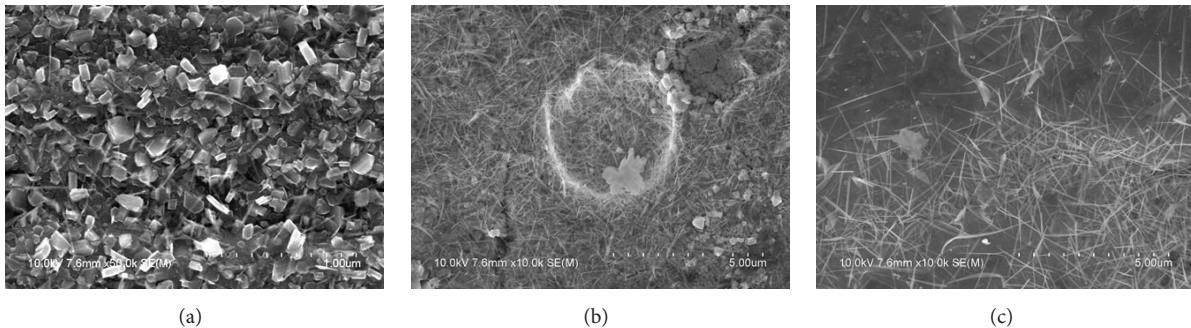


FIGURE 10: SEM photographs after corrosion test of 500 h for specimens of different surface treatments: (a) reference specimen, (b) specimen SP45, shot peening only, and (c) specimen EP45, electropolishing after shot peening.

shown to have the values of 1.34, 1.18, and 0.88 mg/m² h for specimens B, C, and D, respectively. Specimen D treated at high shot peening intensity shows a decrease of about 40% in the corrosion rate in comparison to as-received specimen A. Figure 9(b) shows the corrosion test results for the samples processed at different shot peening angles and distances, with or without electropolishing. The results indicate that weak shot peening was not effective for the reduction of the dissolution rate of metal ions (SP30, SP45, and SP90 specimens), whereas electropolishing after the shot peening (EP45, EP90 specimens) decreased the corrosion rate to less than 1/4 of that of reference specimen A.

The observations of the oxidic surface are shown in Figure 10. The oxide layer formed on reference specimen A shows a polyhedral crystal structure (Figure 10(a)), but the oxide layer on the shot-peened surface shows an almost needlelike morphology with small additional platelike particles (Figure 10(b)). In the case of electropolished surfaces, the needlelike oxides were concentrated in the dimples induced by shot peening whereas the outer surface showed little coverage of deposited oxides (Figure 10(c)). Investigation of

Seo et al. about the corrosion behavior of Alloy 690 at high-temperature condition shows that the change of the oxide morphology from polyhedral to wirelike shape was induced by a roughness change of the surface [21].

The increase in roughness by shot peening might be assumed to have a negative effect on the corrosion behavior; however, the results of the corrosion tests in primary environment indicate that the corrosion rate was reduced on increasing shot peening intensity. The depth of the oxide film might grow by the chemical reaction and deposition of metal ions in solution or by a metallic transfer from the metal-oxide interface. Because the corrosion environment was not changed, the different test results show that the corrosion rate relies on the metal-ion dissolution rate at the metal-oxide interface, and the metal-ion transfer depends on the residual stress in the metallic surface layer. The compressive residual stress formed in the sublayer beneath the outer metal surface of the specimen is considered to constrain the metal-ion release into the oxide film or solution [9]. The corrosion rate is proportional to the concentration gradient of the metallic species near the metal-oxide interface and to the

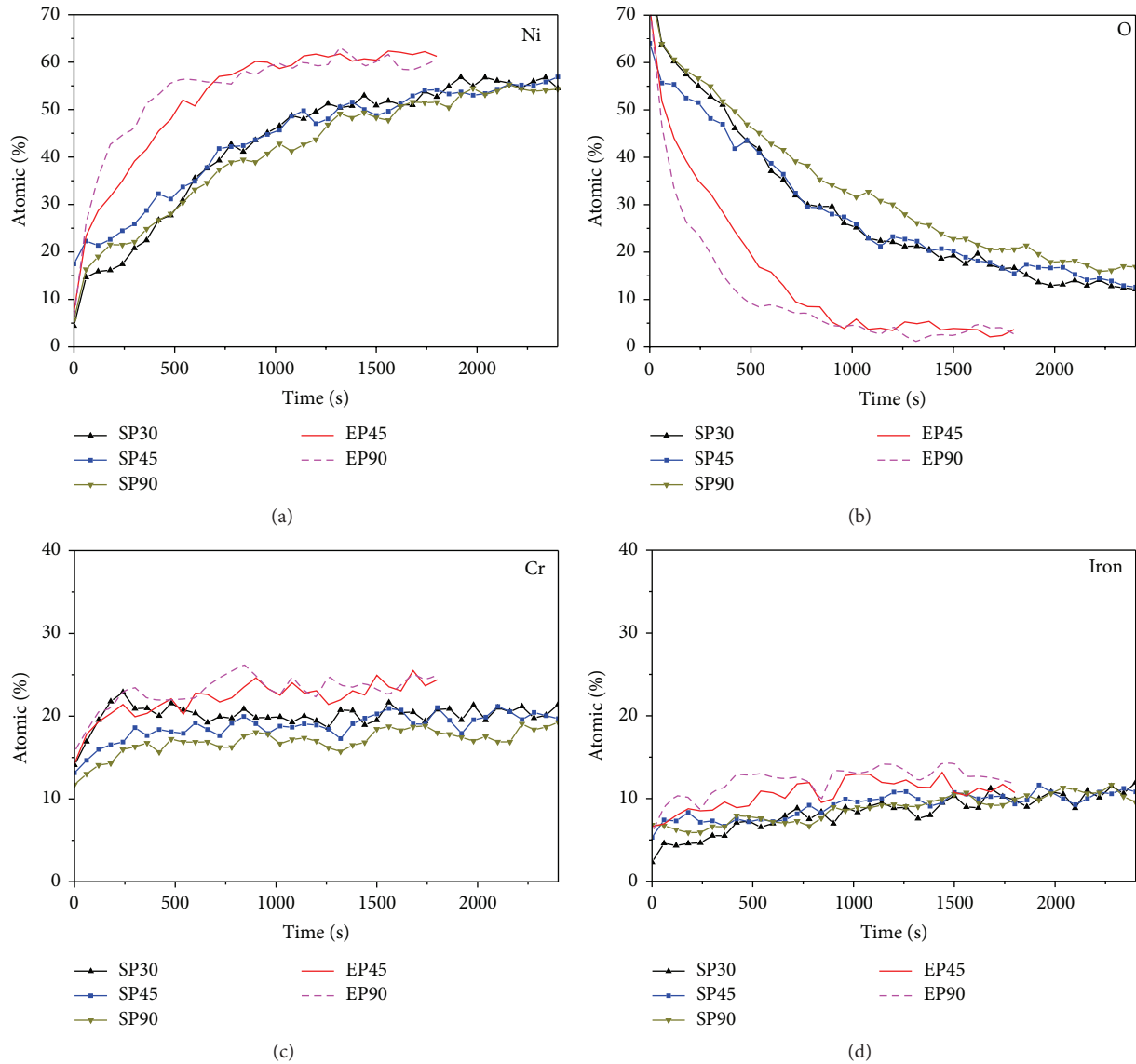


FIGURE 11: XPS depth profiles of the oxide layer for the elements (a) nickel, (b) oxygen, (c) chromium, and (d) iron.

mass-transfer property in the liquid phase that is governed by the solubility.

The corrosion-release rate can be controlled by the surface modification using electropolishing, as shown in Figure 9(b). The electropolishing treatment modifies the surface roughness and structure of the oxide layer. It is assumed that electropolishing reduces the density of dislocations which provide short-circuit paths for the diffusion of metal ions in the matrix [22] and promote the formation of a passive film in the primary coolant environment at high temperature. Figure 11 shows the XPS depth profiles for the individual elements Ni, O, Cr, and Fe in the oxide layer of Alloy 690. The content of nickel in the oxide layer of the specimens treated only by shot peening was more strongly reduced than in case of the electropolished specimens. The depletion of nickel in the oxide film is balanced by oxygen because the amount of chromium and iron did not change considerably, as shown in

Figures 11(c) and 11(d). The oxygen distribution in the oxide layer (Figure 11(b)) shows that the electropolishing treatment reduced the thickness of the oxide film and maintained a higher nickel content in comparison to the specimens treated only by shot peening. This result indicates that the additional electropolishing after shot peening could effectively mitigate the dissolution of nickel ions from SG tube materials.

4. Conclusions

The control of the nickel ion release rate is very important for reducing the radioactive dose rate and the deterioration of fuel performance in nuclear power plants. In this study, the surface residual stress of Alloy 690 was measured and its effect on the corrosion behavior was investigated. The modification of the SG tube surface induced by shot peening and electropolishing could affect the corrosion rate under primary

water conditions. Compressive residual stress is induced by the shot peening treatment, and its value depends on the shot peening intensity at the surface of Alloy 690. Higher shot peening intensity causes reduction in the corrosion rate. It is considered that the compressive residual stress beneath the surface layer suppresses the metal-ion transfer in the alloy matrix. At low shot peening intensity, the corrosion rate is not remarkably changed but the oxide morphology of the corrosion products was changed from polyhedral shape to a needlelike type. When the surface was further modified by electropolishing after shot peening, the corrosion rate was reduced to almost a quarter of that obtained by shot peening only. The dissolution of nickel ions from SG tube materials was mitigated by the additional electropolishing treatment after the shot peening process.

Conflict of Interests

The authors declare that there is no conflict of interests regarding the publication of this paper.

Acknowledgment

This work was supported by the National Research Foundation of Korea (NRF) grant funded by the Korea government (MSIP).

References

- [1] N. Engler, C. Brun, and M. Gullodo, *Optimization of SG Tubes Prefilming Process to Reduce Nickel Release*, NPC, Berlin, Germany, 2008.
- [2] F. Carette, "Impact of the surface state of steam generator tubes on the release of corrosion products in pressurized water reactors," in *Proceedings of the International Conference on Water Chemistry of Nuclear Reactor Systems*, Jeju, Republic of Korea, 2006.
- [3] Y. J. Kim, "Reactor core risk assessment on Zn injection in PWR," in *Proceedings of the UNIST MNE Seminar*, October 2014.
- [4] K. Fruzzetti, "Pressurized water reactor primary water chemistry guidelines, Rev. 6," EPRI Report, 2007.
- [5] C. J. Wood, "Water chemistry control in lwrs," *Comprehensive Nuclear Materials*, vol. 5, pp. 17–47, 2012.
- [6] F. Giraudeau, D. H. Lister, D. R. Morris, U. Setthanan, F. R. Steward, and L. T. Yang, "Henry's law constant for hydrogen in high temperature water with dissolved lithium and boron," *Canadian Journal of Chemical Engineering*, vol. 86, no. 6, pp. 1032–1038, 2008.
- [7] D. H. Lee, M. S. Choi, and U. C. Kim, *The Effect of the Hydrogen and Li/B Concentration on the Stress Corrosion Cracking of Alloy 600 in Simulated PWR Primary Water at 330°C*, NPC, Jeju, Republic of Korea, 2006.
- [8] D. S. Morton, S. A. Attanasio, and G. A. Young, *Primary Water SCC Understanding and Characterization Through Fundamental Testing in the Vicinity of the Nickel/Nickel Oxide Phase Transition*, NPC, Jeju, Republic of Korea, 2006.
- [9] Z. Zhang, J. Wang, E.-H. Han, and W. Ke, "Effects of surface state and applied stress on stress corrosion cracking of Alloy 690TT in lead-containing caustic solution," *Journal of Materials Science and Technology*, vol. 28, no. 9, pp. 785–792, 2012.
- [10] M. Clauzel, M. Guillodo, and M. Foucault, *Correlation between Ni Base Alloys Surface Conditioning and Cation Release Mitigation in Primary Coolant*, NPC, Québec, Canada, 2010.
- [11] L. Guinard, O. Kerrec, D. Noel, S. Gardey, and F. Coulet, "Influence of the initial surface condition on the release of nickel alloys in the primary circuit of PWRs," *Nuclear Energy*, vol. 36, no. 1, pp. 19–27, 1997.
- [12] F. Huang, J. Q. Wang, E. H. Han, and W. Ke, "Short-time oxidation of alloy 690 in high-temperature and high-pressure steam and water," *Journal of Materials Science and Technology*, vol. 28, no. 6, pp. 562–568, 2012.
- [13] S. E. Ziemniak, M. Hanson, and P. C. Sander, "Electropolishing effects on corrosion behavior of 304 stainless steel in high temperature, hydrogenated water," *Corrosion Science*, vol. 50, no. 9, pp. 2465–2477, 2008.
- [14] J. J. Kai, C. H. Tsai, and G. P. Yu, "The IGSCC, sensitization, and microstructure study of Alloys 600 and 690," *Nuclear Engineering and Design*, vol. 144, no. 3, pp. 449–457, 1993.
- [15] P. Hernalsteen, "PWSCC in the tube expansion zone— an overview," *Nuclear Engineering and Design*, vol. 143, no. 2-3, pp. 131–142, 1993.
- [16] V. N. Shah, D. B. Lowenstein, A. P. L. Turner et al., "Assessment of primary water stress corrosion cracking of PWR steam generator tubes," *Nuclear Engineering and Design*, vol. 134, no. 2-3, pp. 199–215, 1992.
- [17] S. E. Ziemniak and M. Hanson, "Corrosion behavior of NiCrFe Alloy 600 in high temperature, hydrogenated water," *Corrosion Science*, vol. 48, no. 2, pp. 498–521, 2006.
- [18] J. F. Ziegler and J. P. Biersack, *SRIM-2000, 40: The Stopping and Range of Ions in Matter*, IBM-Research, Yorktown, NY, USA, 2000.
- [19] M. R. Fard, T. E. Blue, and D. W. Miller, "SiC semiconductor detector power monitors for space nuclear reactors," in *Proceedings of the Space Technology and Applications International Forum (STAIF '04)*, Albuquerque, NM, USA, February 2004.
- [20] A. Gill, A. Telang, S. R. Mannava et al., "Comparison of mechanisms of advanced mechanical surface treatments in nickel-based superalloy," *Materials Science and Engineering A*, vol. 576, pp. 346–355, 2013.
- [21] M. J. Seo, H.-S. Shim, K. M. Kim, S.-I. Hong, and D. H. Hur, "Influence of surface roughness on the corrosion behavior of Alloy 690TT in PWR primary water," *Nuclear Engineering and Design*, vol. 280, pp. 62–68, 2014.
- [22] N. Shaigan, W. Qu, D. G. Ivey, and W. Chen, "A review of recent progress in coatings, surface modifications and alloy developments for solid oxide fuel cell ferritic stainless steel interconnects," *Journal of Power Sources*, vol. 195, no. 6, pp. 1529–1542, 2010.

Research Article

Preparation of U–Zr–Mn, a Surrogate Alloy for Recycling Fast Reactor Fuel

Jong-Hwan Kim, Ki-Hwan Kim, and Chan-Bock Lee

Next Generation Fuel Division, Korea Atomic Energy Research Institute, Daejeon 305-353, Republic of Korea

Correspondence should be addressed to Jong-Hwan Kim; jhk9@kaeri.re.kr

Received 27 May 2015; Revised 26 August 2015; Accepted 8 September 2015

Academic Editor: Randhir Singh

Copyright © 2015 Jong-Hwan Kim et al. This is an open access article distributed under the Creative Commons Attribution License, which permits unrestricted use, distribution, and reproduction in any medium, provided the original work is properly cited.

Metallic fuel slugs of U–10Zr–5Mn (wt%), a surrogate alloy for the U–TRU–Zr (TRU: a transuranic element) alloys proposed for sodium-cooled fast reactors, were prepared by injection casting in a laboratory-scale furnace, and their characteristics were evaluated. As-cast U–Zr–Mn fuel rods were generally sound, without cracks or thin sections. Approximately 68% of the original Mn content was lost under dynamic vacuum and the resulting slug was denser than those prepared under Ar pressure. The concentration of volatile Mn was as per the target composition along the entire length of the rods prepared under 400 and 600 Torr. Impurities, namely, oxygen, carbon, silicon, and nitrogen, totaled less than 2,000 ppm, satisfying fuel criteria.

1. Introduction

A metallic fuel is a promising candidate to power sodium-cooled fast reactors (SFRs). Compared with other fuel forms, the higher densities of fissile and fertile materials in metallic fuels offer superior reactor core performance, hence affording increased breeding ratio and reducing the fissile inventory [1–5].

However, the low melting temperature of metallic fuels such as pure U, Pu, and U–Pu alloys makes them unsuitable for high-temperature applications because of the dangers associated with molten elements penetrating the cladding. The addition of certain high melting temperature elements such as Cr, Mo, Ti, and Zr has therefore been investigated to boost the liquidus temperature and enhance the thermal and mechanical stability of the alloy system.

The excellent corrosion resistance and mechanical stability during the cycling of U–Zr-based alloys make them promising nuclear fuels. Moreover, Zr metal has a low thermal-neutron cross section and is unique in suppressing interdiffusion between the nuclear fuel and stainless-steel cladding. These favorable properties have led to the development of U–Zr fuel systems for SFRs.

Over several decades, various methods have been developed to fabricate metallic fuel, such as rolling, swaging,

wire drawing, and coextrusion; however, these processes are limited by the additional steps that are required and by complex setups, making them unsuitable for remote use [2, 6, 7]. For SFR applications, metallic fuel needs to be mass-produced remotely and inexpensively, while minimizing the amount of radioactive wastes. Casting is one of the oldest manufacturing processes and is used to produce shapes that are not readily machined. By carefully choosing the mold and the filling method, injection casting can be used advantageously to prepare small-diameter castings with a high length/diameter ratio and a randomly oriented grain structure.

In injection casting, the pressure difference between the interior of the mold and the furnace is exploited to drive the molten metal up into a quartz tube, either under a dynamic vacuum or a low-pressure atmosphere. A large number of input parameters have to be defined for this process, relating to the casting machine, injection, mold, and cast metal. Among these, the melt temperature, injection pressure, mold temperature, and pressure holding time are crucial, because small deviations from the optimal values can substantially degrade the quality of the product.

In the present work, a laboratory-scale induction furnace was designed and constructed to study injection casting variables and handling techniques. Firstly, a surrogate copper



FIGURE 1: Induction copper coil used for heating the raw materials.

slug, whose melting temperature is similar to that of uranium, was prepared to evaluate the effect of injection casting variables on the fuel slug. Then, U-10Zr-5Mn slugs (wt%), surrogates for the U-TRU-Zr slugs (TRU: a transuranic element) advanced for SFRs, were produced and their characteristics were evaluated.

2. Experimental

Figure 1 shows the induction copper coil used in this study. In keeping with the scale of the equipment, casting was conducted in a small furnace with a capacity of ~0.5 kg U-Zr alloy per batch operation. The main components are a melting furnace, a vacuum pumping system, and a pressuring system. The intention here is to prove the practicality of injection casting as a means of producing fuel slugs and to furnish the necessary design information for hot-cell applications. Components such as the crucible, crucible cover, graphite insulation, and water-cooled copper induction coil are contained within the furnace.

The chamber has a double-shell structure for water cooling and the chamber cover is designed to rotate to facilitate the separation of the mold assembly before and after casting. The quartz mold is preheated using a cartridge heater and insulated with ceramic wool. Pressurized inert gas was used to force molten metal, stored in the accumulator tank adjacent to the casting furnace, into quartz molds. For this study, the feedstock materials were weighed in proportion to the alloy composition and charged into a melting crucible. The crucible was heated at 100°C/min and elevated to the target temperature by induction copper coil.

Before injecting the melt, the heating power was reduced from 100% to 0% to maximize the electromagnetic force and homogenize the alloy via electromagnetic stirring. Once the quartz mold and alloy melt had reached the target temperature, the former was immersed in the latter and the chamber was filled with pressurized gas to inject the molten alloy into the mold. After injection casting, the fuel slug was extracted from the mold in a glove box.

Fuel slugs were cut into slices of suitable thickness using a slow-speed SiC abrasive cut-off wheel and the density at each location was measured using Archimedes' principle. The microstructures and compositions were analyzed using

scanning electron microscope (SEM) with energy-dispersive X-ray spectroscopy (EDS). Casting yields and fuel losses were evaluated by measuring the material balance before and after casting. The chemical composition of the fuel slugs and the presence of impurities were also assessed by inductively coupled plasma atomic emission spectrometry (ICP-AES).

3. Results and Discussion

Assuming a homogeneous liquid at constant temperature, the height of the liquid in the mold can be expressed in terms of the applied pressure as follows:

$$h = \frac{1}{\rho} \times \frac{p}{g}, \quad (1)$$

where h is height of the liquid, p is the fluid pressure, g is the gravitational constant, and ρ is the density of the liquid. However, for dynamic systems such as metallic fuel melts, many factors neglected in this equation hinder the rise of the melt, namely, the wettability, the cooling rate, temperature and density variations, and other hydraulic effects. These hindering effects can be circumvented by superheating the melt, preheating the mold, and increasing the pressure difference between the mold's interior and the furnace. However, because these factors affect one another, they should be optimized carefully.

Before using radioactive uranium, a copper slug was cast to study the interplay of these variables and optimize the handling of the apparatus. Copper has a melting temperature similar to that of uranium but does not carry a radiation risk. Table 1 lists the furnace pressures and other experimental parameters used to cast the copper slug (tests *a-d*). The holding time is the delay between the submersion of the mold tip and the pressurization of the furnace. The immersion time is the delay between the submersion and retraction of the mold tip.

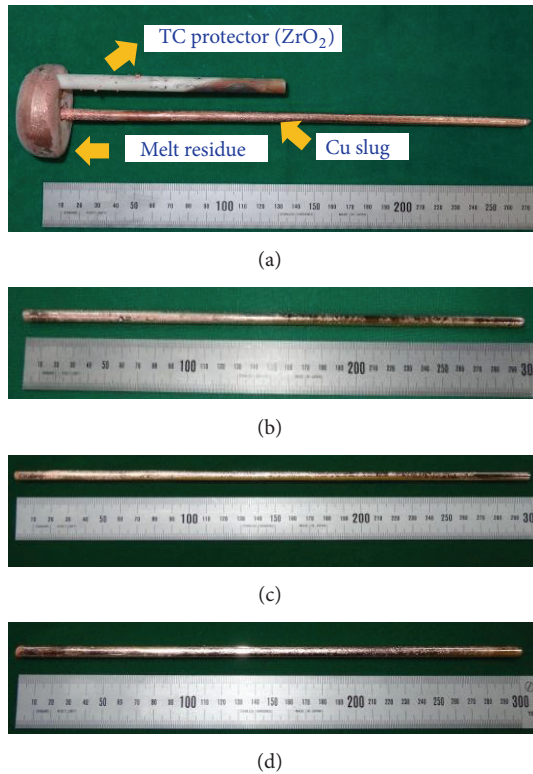
Test *a* was performed under dynamic vacuum conditions, at an injection pressure of ~0.8 kgf/cm², and with no electromagnetic induction while the mold was immersed. As shown in Figure 2(a), the Cu slug obtained was attached to the heel at the bottom of the mold as a result of the low casting temperature or relatively long immersion time. Nonetheless, the slug filled and was cast to the full length of the mold, with no thin sections observed.

In order to prevent the slug from solidifying too rapidly and becoming attached to the heel, in test *b*, induction was maintained until the mold was removed from the melt—the conditions being otherwise the same as those used for test *a*. Figure 2(b) shows that the resulting Cu slug was cast to the full length of the mold but not attached to the heel. The surface is however coarser in the lower region (left side of the photograph), where the temperature was highest during casting, than in the middle and upper regions of the slug.

Temperature is known to be the most important casting variable because it governs both the fluidity of the melt during mold filling and the surface state of the slug via its interactions with the hot mold. Shrinkage defects appear more readily in high-temperature melts; the melt temperature

TABLE 1: Experimental parameters for injection casting of Cu and U-10Zr-5Mn fuel slugs.

	Test <i>a</i>	Test <i>b</i>	Test <i>c</i>	Test <i>d</i>	Test <i>e</i>	Test <i>f</i>	Test <i>g</i>
Charge alloy composition (wt%)	Cu	Cu	Cu	Cu	U-10Zr-5Mn	U-10Zr-5Mn	U-10Zr-5Mn
Casting temperature (°C)	1160	1160	1120	1120	1530	1450	1450
Injection pressure (kgf/cm ²)	0.8	0.8	0.8	0.8	2.5	3.4	3.4
Chamber atmosphere before injection	Dynamic vacuum condition	Ar (400 Torr)	Ar (600 Torr)				
Holding time (sec.)	2	2	2	2	4	2	2
Emerging time (sec.)	18	18	18	10	5	5	5

FIGURE 2: Photographs of surrogate copper slugs prepared in (a) test *a*, (b) test *b*, (c) test *c*, and (d) test *d*.

should therefore be kept as low as possible to improve the quality of the casts, while ensuring nonetheless that the melt fills the mold adequately. For test *c*, the casting temperature was lowered from 1160 to 1120°C and indeed Figure 2(c) shows that the surface state of the Cu slug is better than that of the slugs obtained in test *a* or *b*.

Figure 2(d) shows the Cu slug fabricated under the same conditions as those used for test *c*, but with the delay between the submersion of the mold tip in the melt and its retraction reduced from 18 to 10 s (test *d*). The objective was to reduce the heating time in the melt and thereby reduce the thermal stress on the lower part of the slug. The fuel slug did not

drip back into the melt and its surface condition is visibly improved (Figure 2(d)).

Based on these preliminary tests with copper, U-Zr-Mn, a surrogate alloy for U-TRU-Zr, was injection cast. U-TRU ingots, the raw nuclear fuel for SFRs, are converted through pyroprocessing from spent fuel generated in nuclear power plants and contain volatile minor actinide such as Am. Volatile elements are difficult to melt and cast because they tend to vaporize and are often poorly incorporated in the product. A simple solution to this problem is to enrich the casting charge and accept the loss, as in conventional casting; however, this approach is not suitable for radioactive materials, in particular, those containing minor actinides which may transmute into short-lived or nonactive elements in the nuclear reactor.

The equilibrium vapor pressure of Am at 1465°C is about 3.3 Torr, and over the range of melting temperatures, the vapor pressure of Am is nearly three orders of magnitude higher than that of Pu. The vapor pressures of U and Zr are known to be 3 and 4.5 orders of magnitude less than that of Pu, respectively [8–13]. This implies that Am is the element most likely to be lost as vapor during the casting process. According to [13–15], Mn has a vapor pressure similar to that of Am in the temperature range of 1200–1600°C (Figure 3). In addition, the U-rich end of the U-Mn phase diagram exhibits no liquid miscibility [16]. Thus, Fielding investigated the use of a U-Mn-Zr alloy system to simulate the loss of Am during the melting process [17].

The furnace temperatures and other experimental parameters used to cast the U-Zr-Mn slugs are listed in Table 1 (tests *e–g*). The volatility of Mn was estimated under dynamic vacuum conditions in test *e* and under pressures of 400 and 600 Torr in tests *f* and *g*, respectively. The casting temperature is an important variable in the casting of fuel slug, and it is affected by many factors such as casting shape (length, diameter, volume, and area), batch size, mold filling time, cooling conditions, and casting method. In this study, casting temperature is referred to [18], where U-Zr-Mn alloy slug was fabricated soundly.

Figure 4(a) shows an as-cast U-Zr-Mn slug prepared under dynamic vacuum conditions at an injection pressure of 2.5 kgf/cm² (test *e*). The slug fills the full length of the

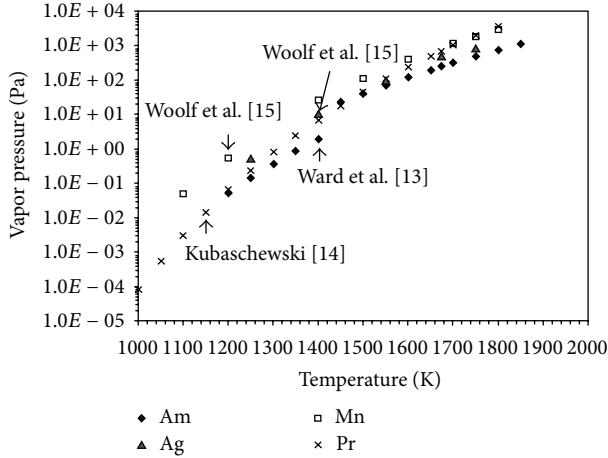


FIGURE 3: Vapor pressure of americium, manganese, silver, and praseodymium as a function of temperature [7, 13–15].

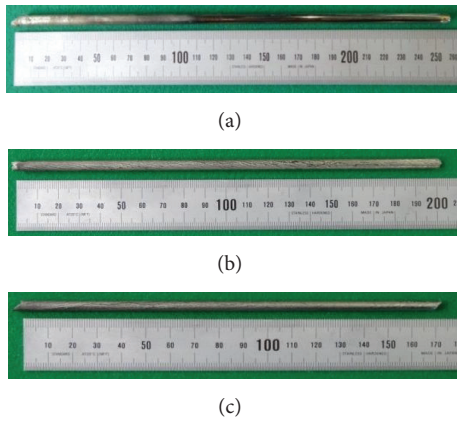


FIGURE 4: Photographs of U-10Zr-5Mn slugs prepared in (a) test *e*, (b) test *f*, and (c) test *g*.

mold and is generally sound with no cracks or thin sections visible. As for the Cu slug, the bottom surface is rougher, where the quartz mold was immersed in the melt (left side of the photograph), and some reaction layers are observed.

For tests *f* and *g*, the casting temperature was lowered from 1530 to 1450°C, to reduce the risk of Mn vaporization and improve the surface state of the resulting slug. As shown in Figures 4(b) and 4(c), the slug shortens as the atmosphere pressure is increased, reflecting the corresponding increase in the repulsive pressure during mold filling.

Figure 5 shows the density of the U-10Zr-Mn slugs as measured from samples taken from the lower, middle, and upper portions of each slug. The average densities are 15.7, 15.3, and 14.8 g/cm³ for the fuel slugs prepared in tests *e*, *f*, and *g*, respectively. The low standard deviations associated with each value (± 0.2 g/cm³) show that the inductive forces during melting and alloying were sufficient to mix the melt homogeneously. Figure 5 shows furthermore that the U-Zr-Mn slug prepared under dynamic vacuum (test *e*) is denser than the one prepared under pressure. This is the result of Mn

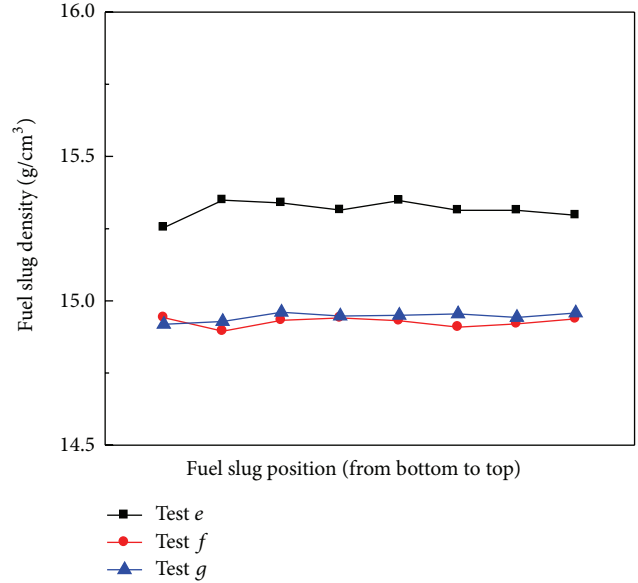


FIGURE 5: Distributions of fuel slug density according to the position of fuel slug.

vaporization. Indeed, as Mn is vaporized more readily than the other elements, the concentrations of U and Zr and the density of the alloy increase notably because the atomic mass of U is more than twice that of Mn. However, vaporization is inhibited under Ar pressure (tests *f* and *g*), resulting in slugs with a higher Mn content and lower density. The fact that the density of the slugs prepared under Ar is homogeneous along their length implies that pressures up to 400 Torr do not have a significant effect on the vaporization of Mn. This effect is quantified below in terms of the chemical composition of the casts.

The chemical compositions of the surrogate fuel slugs were obtained by ICP-AES. Table 2 shows the Mn and Si concentrations measured in the lower, middle, and upper portions of each slug. Under dynamic vacuum conditions (test *c*), approximately 68% of the original Mn content is lost by vaporization, indicating that dynamic vacuums are unsuitable for the fabrication of fuel slugs containing volatile radioactive constituents such as Am. Under 400 and 600 Torr Ar, however, the Mn content is as per the target composition along the entire length of the slugs, indicating that the volatile element was retained throughout the melting and alloying processes. The average Mn content of these slugs is ~5.1 wt%.

The impurity (i.e., oxygen, carbon, silicon, and nitrogen) content of the slugs is less than 2,000 ppm and thereby satisfies the tentative criteria defined for Experimental Breeder Reactor II fuel. Silicon is found in a higher concentration toward the bottom of the slug, the region in contact with melt, because of reactions with the melt during injection.

Figure 6 shows the U, Zr, and Mn concentrations measured in the lower, middle, and upper portions of the slugs. The fuel slugs prepared at 400 and 600 Torr have Zn contents in the target (11.0–9.0 wt% Zn) range; however, the fuel slug prepared under dynamic vacuum is richer in U and Zr, as

TABLE 2: Concentrations of Mn and Si according to position of U-10Zr-5Mn fuel slugs prepared by injection casting.

Fuel slug location	Test <i>e</i>		Test <i>f</i>		Test <i>g</i>	
	Mn (wt%)	Si (wt%)	Mn (wt%)	Si (wt%)	Mn (wt%)	Si (wt%)
Lower						
1	1.51	0.09	5.19	0.03	5.01	0.06
2	1.52	0.04	5.03	0.02	5.26	0.02
Middle						
1	1.49	0.02	5.11	0.02	5.28	0.02
2	1.48	0.03	5.06	0.02	5.36	0.01
Upper						
1	1.56	0.02	5.18	0.01	4.92	0.01
2	1.80	0.01	5.18	0.01	4.91	0.01

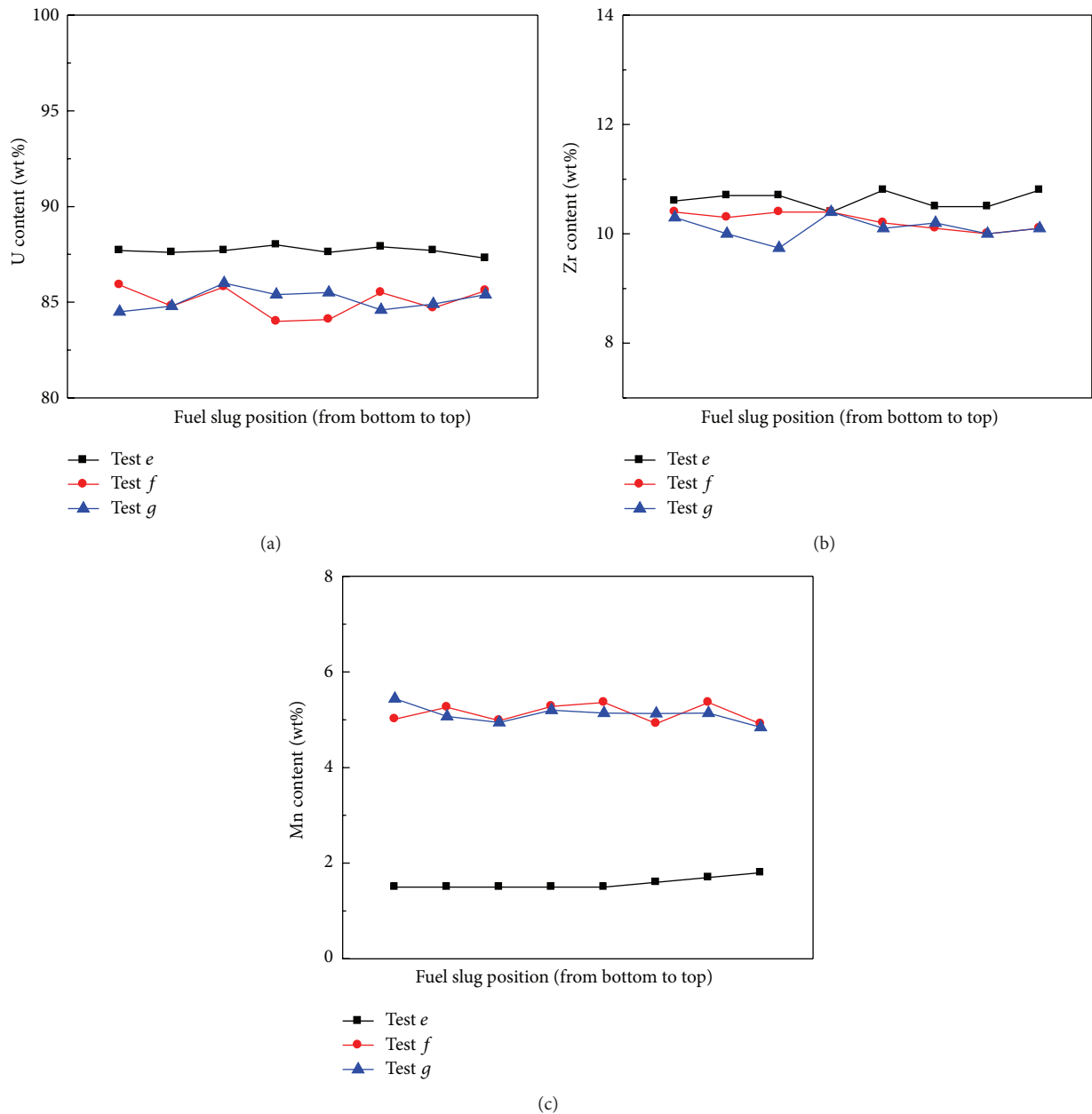


FIGURE 6: Variations of chemical composition according to the position of a U-Zr-Mn fuel slug fabricated under different injection casting conditions: (a) U, (b) Zr, and (c) Mn.

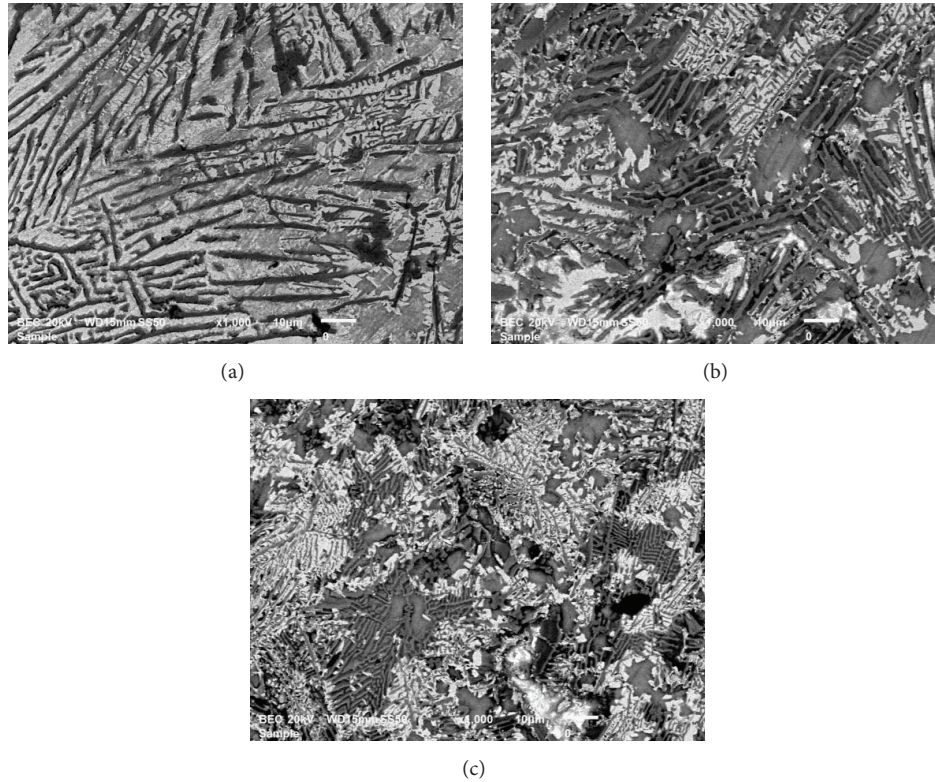


FIGURE 7: Scanning electron micrographs according to position of as-cast U–Zr–Mn fuel slug prepared in test *e*: (a) lower region, (b) middle region, and (c) upper region.

suggested already by its increased density. As mentioned above, this is the result of Mn vaporization (Figure 6(c)).

The microstructures at different positions of the as-cast fuel slug were examined to determine the effect of cooling rate. Figure 7 shows scanning electron micrographs of the lower, middle, and upper portions of the U–10Zr–5Mn fuel slug prepared in test *e*. It can be observed that the interlamellar spacing is large at the lower portion and becomes smaller at the upper portion. The reduction in interlamellar spacing at the upper portion can be explained by the cooling conditions. Because the lower portion is continuously heated by the high-temperature melt during the casting process, it has a lower cooling rate compared to the middle and upper portions. Hence, the thermal undercooling is relatively high at the upper portion, which leads to a high rate of nucleation and a smaller interlamellar spacing. The chemical composition of the lamellar structure was elucidated using an electron microscope fitted with an energy-dispersive X-ray analyzer, as shown in Figure 8. Figure 8(a) is a magnified image of the micrograph shown in Figure 7(a). The plate-like phase marked by “A” shows a higher content of Zr and Mg and lower content of U (Figure 8(b)), and the block phase marked by “B” shows a higher U content and lower Zr content (Figure 8(c)).

Quantifying and reducing the amount of fuel lost during its preparation are crucial because large recycling and waste streams lower the productivity and economic efficiency of the production process. The material balances in the crucible and

in the mold were quantified after casting the U–Zr–Mn slugs, as shown in Table 3. While a large amount of fuel is lost by casting under dynamic vacuum conditions, the fuel loss is within 0.1 wt% when casting under 400 or 600 Torr Ar. The fuel losses relative to the initial contents are 3.1%, 0.06%, and 0.04% in tests *e*, *f*, and *g*, respectively. This result indicates that fuel loss decreases as the atmosphere pressure increases, becoming very small for pressures greater than 400 Torr.

4. Conclusions

As surrogates for the U–TRU–Zr slugs proposed to fuel SFRs, U–10Zr–5Mn slugs were injection cast under different conditions in a laboratory-scale furnace and their characteristics were evaluated. The effects of injection temperature, electromagnetic stirring, and immersion time were evaluated in preliminary tests conducted using Cu slugs. As-cast U–Zr–Mn slugs were generally sound, without cracks or thin sections. The shorter the as-cast U–Zr–Mn slugs, the higher the atmosphere pressure. Under dynamic vacuum conditions, approximately 68% of the original Mn content was lost by vaporization, and the resulting U–Zr–Mn fuel slug was denser than that prepared under Ar atmosphere. This result indicates that fuel slugs containing volatile minor actinides should not be injection cast under dynamic vacuum conditions. Increasing the atmosphere pressure is also shown here to reduce fuel loss. All the U–Zr–Mn slugs prepared in this study contained less than 2,000 ppm impurities (namely,

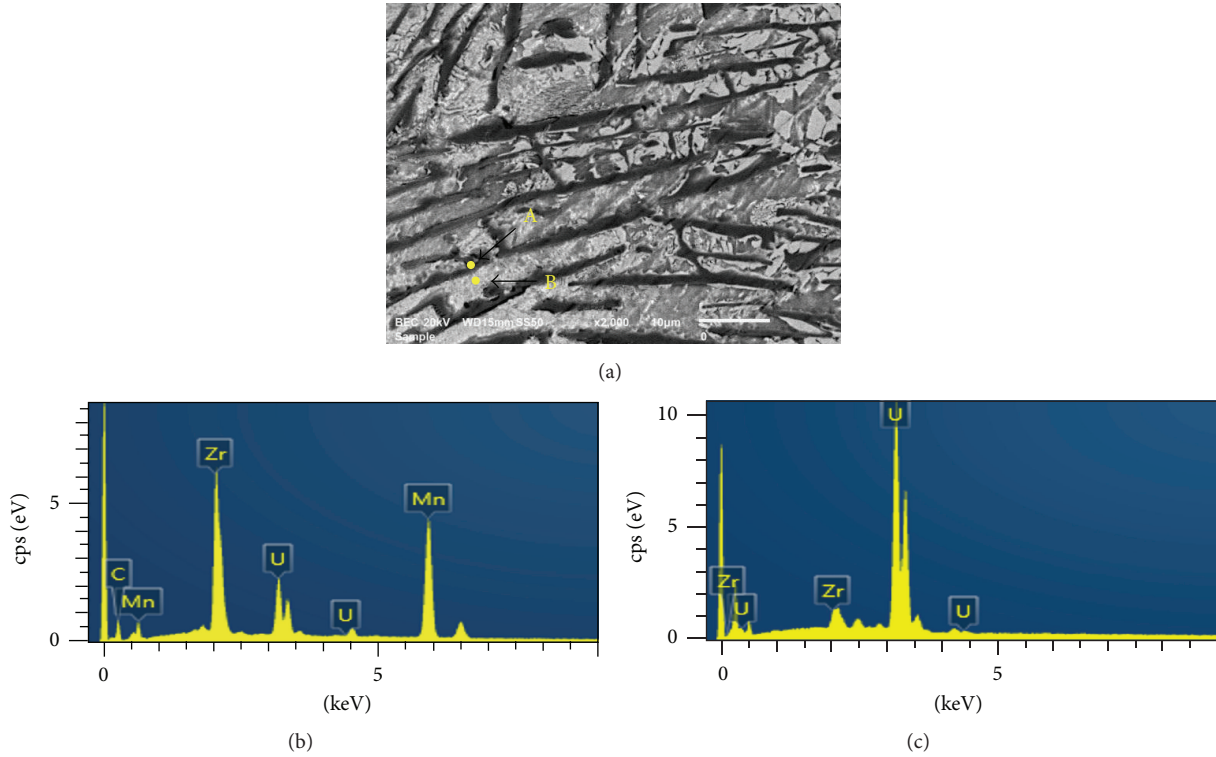


FIGURE 8: (a) Magnified image of the micrograph shown in Figure 7(a), and EDX spectra at (b) spot “A” and (c) spot “B” marked in (a).

TABLE 3: Material balance after injection casting of U-10 wt% Zr-5 wt% RE fuel slugs.

	Casting part	Test e		Test f		Test g	
		Mass (g)	Fraction (%)	Mass (g)	Fraction (%)	Mass (g)	Fraction (%)
Before casting	Crucible assembly	607.2	100	428.1	100	420.19	100
After casting	Crucible assembly	497.1	81.86	362.3	84.62	365.0	86.90
	Mold assembly	91.3	15.04	65.5	15.30	55.0	13.10
Fuel loss	—	18.8	3.10	0.30	0.06	0.19	0.04

oxygen, carbon, silicon, and nitrogen), satisfying the criteria defined for SFR fuels.

Conflict of Interests

The authors declare that there is no conflict of interests regarding the publication of this paper.

Acknowledgment

This study was supported by Nuclear Research & Development Program of the National Research Foundation Grant funded by the Ministry of Education, Science and Technology in Korea (Grant no. 2013M2A8A2000676).

References

- [1] C. E. Stevenson, *The EBR-II Fuel Cycle Story*, American Nuclear Society, La Grange Park, Ill, USA, 1987.
- [2] L. C. Walters, B. R. Seidel, and J. H. Kittel, “Performance of metallic fuels and blankets in liquid-metal fast breeder reactors,” *Nuclear Technology*, vol. 65, no. 2, pp. 179–231, 1984.
- [3] L. C. Walters and G. L. Hofman, “Metallic fast reactor fuels: a comprehensive treatment,” *Materials Science and Technology A*, vol. 10, pp. 1–43, 1994.
- [4] G. L. Hofman, L. C. Walters, and T. H. Bauer, “Metallic fast reactor fuels,” *Progress in Nuclear Energy*, vol. 31, no. 1-2, pp. 83–110, 1997.
- [5] D. C. Crawford, D. L. Porter, and S. L. Hayes, “Fuels for sodium-cooled fast reactors: US perspective,” *Journal of Nuclear Materials*, vol. 371, no. 1–3, pp. 202–231, 2007.
- [6] D. E. Burkes, R. S. Fielding, D. L. Porter, D. C. Crawford, and M. K. Meyer, “A US perspective on fast reactor fuel fabrication technology and experience part I: metal fuels and assembly design,” *Journal of Nuclear Materials*, vol. 389, no. 3, pp. 458–469, 2009.
- [7] D. E. Burkes, R. S. Fielding, and D. L. Porter, “Metallic fast reactor fuel fabrication for the global nuclear energy partnership,” *Journal of Nuclear Materials*, vol. 392, no. 2, pp. 158–163, 2009.

- [8] H. A. Kick and R. N. R. Mulford, "Vapor pressure of neptunium," *The Journal of Chemical Physics*, vol. 41, no. 5, pp. 1475–1478, 1964.
- [9] S. C. Carniglia and B. B. Cunningham, "The vapor pressure of americium metal," *Journal of the American Chemical Society*, vol. 77, no. 6, p. 1502, 1955.
- [10] R. J. Ackermann and E. G. Rauh, "The thermodynamics of vaporization of neptunium and plutonium," *The Journal of Chemical Thermodynamics*, vol. 7, no. 3, pp. 211–218, 1975.
- [11] R. N. R. Mulford, "Thermodynamics," in *Proceedings of the Symposium on Thermodynamics*, vol. 1, p. 231, IAEA, Vienna, Austria, July 1965.
- [12] A. Pattoret, J. Drowart, and S. Smoes, "Thermodynamics of nuclear materials," in *Proceedings of a Symposium in Vienna, 1967*, p. 613, IAEA, Vienna, Austria, 1968.
- [13] J. W. Ward, W. Muller, and G. F. Kramer, "Transplutonium elements," in *Proceedings of Fifth International Conference in Baden-Baden, 1975*, European Institute for Transuranium Elements, Karlsruhe, Germany, 1975.
- [14] O. Kubaschewski, *Materials Thermochemistry*, Pergamon Press, New York, NY, USA, 6th edition, 1993.
- [15] P. L. Woolf, G. R. Zellars, E. Foerster, and J. P. Morris, *Vapor Pressures of Liquid Manganese and Liquid Silver*, US Department of the Interior, Bureau of Mines, 1960.
- [16] T. B. Massalski, P. R. Subramanian, H. Okamoto, and L. Kacprzak, *Binary Alloy Phase Diagrams*, ASM International, 1990.
- [17] R. S. Fielding and D. L. Porter, "Volatile species retention during metallic fuel casting," *Journal of Nuclear Materials*, vol. 441, no. 1–3, pp. 530–534, 2013.
- [18] J. H. Kim, H. Song, H. T. Kim, K. H. Kim, C. B. Lee, and R. S. Fielding, "Development of a new casting method to fabricate U-Zr alloy containing minor actinides," *Journal of Radioanalytical and Nuclear Chemistry*, vol. 299, no. 1, pp. 103–109, 2014.